

# An Accelerator-Based Neutron Imaging System and Its Application to Detection of Corrosion in Aircraft

by  
Shuanghe Shi

B.S., Beijing Normal University (1982)  
M.S., Beijing Normal University (1985)  
M.S., Massachusetts Institute of Technology (1991)

Submitted to the Department of Nuclear Engineering  
in Partial Fulfillment of the Requirements for the Degree of  
Doctor of Philosophy in Nuclear Engineering  
at  
Massachusetts Institute of Technology

May 1995

© Massachusetts Institute of Technology

Signature of Author \_\_\_\_\_  
Department of Nuclear Engineering  
May, 1995

Certified by \_\_\_\_\_  
Richard C. Danza  
Principle Research Scientist, Department of Nuclear Engineering

Read by \_\_\_\_\_  
Ronald G. Ballinger  
Associate Professor, Department of Nuclear Engineering  
Thesis Reader

Accepted by \_\_\_\_\_  
Allan F. Henry  
Chairman, Departmental Committee on Graduate Students

Science  
MASSACHUSETTS INSTITUTE  
OF TECHNOLOGY

JUN 07 1995

LIBRARIES

# **An Accelerator-Based Neutron Imaging System and Its Application to Detection of Corrosion in Aircraft**

by

Shuanghe Shi

Submitted to the Department of Nuclear Engineering  
on April 28, 1995, in Partial Fulfillment of the requirements for the degree of  
Doctor of Philosophy in Nuclear Engineering

## **Abstract**

An accelerator based neutron imaging system has been designed and tested for detection of corrosion by thermal neutron imaging. The system combines a compact radio frequency quadrupole (RFQ) accelerator with an electro-optical imaging system based on a neutron sensitive scintillator which is lens coupled to a cooled, charged coupled device (CCD) imagers. The goal of the system was to produce an imaging system capable of producing both tomographic and planar radiographic neutron images with low neutron fluence such as is obtained from transportable accelerators. The major new elements incorporated into the system are: design and fabrication of a moderator/collimator system for use with neutrons from the reaction  $\text{Be}(d,n)\text{B}$  produced using a 0.9 MeV RFQ; design and characterization of an electro-optical digital neutron imaging system with a dynamic range of  $> 2 \times 10^4$  and with the capability of detecting single neutrons; development of all required software for control of mechanical motion and for tomographic imaging using both back-projection and multi-scale wavelet methods. The measured moderated flux of the accelerator was a few times  $10^4$  n/cm<sup>2</sup>/s, depending on the collimation used. The CCD camera noise was below one neutron/pixel and the system noise was limited by the statistical variance in the neutron flux. The camera resolution was 1152 x 1242 pixels. With the lens used, the resolution of each pixel was 0.15 mm, however most data were taken with pixels grouped to a resolution of 0.63 mm.

Results of measurements on actual aircraft lap joints have shown that the system is capable of detecting corrosion (aluminum hydrates) of 90  $\mu\text{m}$  or less in actual components and that this corrosion can be detected through multiple layers of aluminum such as typical for a lap joint. The operation of the tomographic system was confirmed using a 40 keV x-ray source.

Thesis Supervisor: Richard C. Lanza

Title: Principle Research Scientist, Department of Nuclear Engineering

Thesis Reader: Ronald G. Ballinger

Title: Associate Professor, Department of Nuclear Engineering

# Acknowledgments

I would like to thank my thesis advisor, Dr. Richard C. Lanza, for his guidance and assistance during the entire course of this research work. His intelligence, energy, dedication, patience, good humor and understanding are greatly appreciated. I am especially grateful to his encouragement, financial support and help in my work on the system design. This thesis would not have been possible without the help I received from him. Working with him has been an enjoyable experience in my life.

I thank my thesis reader, Professor Ronald G. Ballinger, for his critical reading and suggestion of the thesis. Thanks also go to Professor Regis Pelloux for his great help in my thesis work and for so many years help and support to my family.

I would like to thank Professor Xiao-lin Zhou and Professor Kevin W. Wenzel for serving as my thesis committee members.

I would like to thank Erik B. Iverson, David W. Fink, Sam Yong, Hongli Dai for many useful discussions and their technical support.

Finally, many thanks to my husband, Jin Liang, for his love, support, understanding, patience and encouragement. I would like to thank my mother-in law, Shujun Ma, without her sacrifice, it would be hard for me to finish my Ph.D. work. I would like to acknowledge the support of my father and my sisters in China who could not be with me in body but were always here in spirit.

# Contents

<b>Abstract</b> .....	2
<b>Acknowledgments</b> .....	3
<b>Contents</b> .....	4
<b>List of Figures</b> .....	7
<b>List of Tables</b> .....	11
<b>Chapter 1 Introduction</b> .....	12
1.1 Main contributions of the thesis .....	13
1.2 Thesis outline .....	15
<b>Chapter 2 Corrosion problems and the solutions</b> .....	17
2.1 Corrosion problems .....	17
2.2 Solutions .....	20
2.3 Historical review .....	25
2.3.1 The historical development of the neutron sources .....	26
2.3.2 The historical development of the neutron tomography .....	31
<b>Chapter 3 Imaging system</b> .....	38
3.1 Background theory .....	38
3.2 Neutron detection system .....	43
3.3 Object handling system: Turn table and translator .....	45
3.4 Optical system .....	48

3.5 CCD camera system .....	52
3.6 Summary .....	55
<b>Chapter 4 Accelerator neutron sources .....</b>	<b>57</b>
4.1 Particle accelerator system .....	57
4.2 Electrostatic accelerator .....	59
4.3 Linear radiofrequency accelerators .....	61
4.4 Circular radiofrequency accelerators .....	62
4.5 Cyclotron accelerators .....	63
4.6 Linear radiofrequency quadrupole accelerators .....	65
4.6.1 Technical description for AccSys technology DL-1 RFQ accelerator .....	69
4.6.2 Control system.....	74
4.6.3 Parameters monitored and controlled .....	74
4.6.4 Operation procedures for the AccSys Technology DL-1 RFQ accelerator.....	76
<b>Chapter 5 Software development for three-dimensional reconstruction for neutron tomography .....</b>	<b>79</b>
5.1 Radiography and tomography .....	79
5.2 Two dimensional reconstruction .....	82
5.2.1 Two dimensional reconstruction algorithms .....	83
5.2.2 Numerical solution for reconstruction.....	85
5.2.2.1 Filtered back projection .....	87
5.2.2.2 Wavelet method .....	91
5.3 Three important reconstruction issues in our experiments.....	92
5.3.1 Reconstruction result changes with $N_{\theta}$ .....	92
5.3.2 Cut-off frequency .....	96
5.3.3 Noise .....	97
5.4 Three dimensional reconstruction method .....	103
<b>Chapter 6 Detector performance and experimental results .....</b>	<b>106</b>
6.1 Noise performance .....	106
6.2 Dynamic range.....	114

6.3 Spatial Resolution .....	114
6.4 Evaluation and demonstration of detection of corrosion.....	121
6.5 Verification of tomographic hardware and reconstruction software performance	127
<b>Chapter 7 Discussion and conclusions .....</b>	<b>130</b>
7.1 Discussion .....	130
7.1.1 Neutron sources .....	130
7.1.2 A comparison of NTI with other corrosion detection methods .....	132
7.2 Conclusions .....	136
7.3 Suggestion for future work.....	138
<b>Appendix A Basic CCD theory.....</b>	<b>139</b>
A.1 A CCD image sensor operates in four successive steps .....	139
A.2 Electrooptical performance.....	143
A.2.1 Spectral response .....	144
A.2.2 Noise .....	145
<b>Appendix B 3-D Reconstruction programs.....</b>	<b>147</b>
<b>References.....</b>	<b>159</b>

# List of Figures

Figure 2.1: An aircraft damaged due to corrosion .....18

Figure 2.2: Military aircraft age tally (up to Sept. 92). .....19

Figure 2.3: Mass absorption coefficients( $\text{cm}^2/\text{g}$ ) as a function of atomic number for thermal neutrons and 20 keV X-ray.....23

Figure 2.4: Evolution of the effective thermal neutron flux from available neutron sources. ....27

Figure 2.5: Diagram of a proposed portable neutron source of the Sb-Be type. After Warman (1962). .....28

Figure 2.6: Polyethylene moderator and cadmium collimator used with an Sb-Be neutron source for radiographic studies by Warman (1962). The diameter of the neutron port is 2 inches, the depth of the port is 3 in. A source configuration such as this, with a  $10^{10}$  n/sec Sb-Be source, yielded a collimated thermal neutron beam intensity in excess of  $10^6$  n/cm<sup>2</sup>-sec. ....29

Figure 3.1: Principle of transmission tomography.....40

Figure 3.2: The relationship of particle fluence  $\Phi$  to differential attenuation for different attenuation coefficients  $\mu$  for a give object dimension of  $D = 10$  cm and a feature size  $\Delta x = 500$   $\mu\text{m}$ . ....41

Figure 3.3: Relationship of particle fluence  $\Phi$  to attenuation coefficients  $\mu$  for different object dimension  $D$  and attenuation differences  $d\mu/\mu$ . ....42

Figure 3.4: The mechanical composition of scintillation screen.....44

Figure 3.5: Turn table and translator. ....46

Figure 3.6: The computer control system. ....	47
Figure 3.7: The Labview software for motion control. Top: the front control panel; Bottom: the diagram panel for the motion control. ....	49
Figure 3.8: The light loss due to the finite lens. ....	51
Figure 3.9: Schematic view of camera system. ....	56
Figure 4.1: Schematic of Cockcroft and Walton's experiment with the first particle accelerator . ....	59
Figure 4.2: Schematic of a linear DC accelerator . ....	60
Figure 4.3: Schematic of a linear RF accelerator. ....	62
Figure 4.4: Schematic of a cyclotron accelerator. ....	64
Figure 4.5: Schemes of static, RF, and RFQ quadrupoles (from top to the bottom). ....	67
Figure 4.6: Modulated RFQ electrodes. ....	67
Figure 4.7: AccSys Technology DL-1 RFQ accelerator. The RFQ is in center with RF amplifier cabinet on left rear and ion source power supply and controls on right. ....	71
Figure 4.8: Detailed cross-section view of the AccSys Technology DL-1 RFQ accelerator. ....	73
Figure 4.9: Total neutron yields versus bombarding energy for several accelerator produced neutron reactions. The yields are given per microampere of bombarding particle current . ....	78
Figure 5.1: The difference between radiography and tomography. ....	81
Figure 5.2: The relationship between 2-D projection data and 3-D object. ....	82
Figure 5.3: Projection of a two dimensional object function. ....	84
Figure 5.4: Projection measurements for an 2-D object at three different angular positions with 6 strip integrals. ....	86
Figure 5.5: A comparison of BP and FBP. ....	88
Figure 5.6 Example of filtered back projection numerical reconstruction calculation result. ....	91

Figure 5.7: Examples of reconstruction using wavelet technique. Using the same data set, the image may be reconstructed on various scales depending on the desired resolution and reconstruction time. ....	93
Figure 5.8: Reconstruction results at different $N_{\theta}$ and $N_s = 128$ . (a) $N_{\theta} = 128$ , (b) $N_{\theta} = 64$ , (c) $N_{\theta} = 20$ .....	95
Figure 5.9: The intensity map of the 128X128 phantom shown in Figure 5.8. The numbers shown are intensities of respective regions. The projection data are gathered using a parallel beam geometry with $N_s = 128$ .....	96
Figure 5.10: Reconstruction results at different cut off frequency. (a) $f_c = 0.85$ , (b) $f_c = 0.75$ , (c) $f_c = 0.5$ . ....	98
Figure 5.11 The intensity map of the 128X128 phantom shown in Figure 5.10. The numbers shown are intensities of respective regions. The projection data are gathered using a parallel beam geometry with $N_s = 128$ and $N_{\theta} = 128$ . ....	99
Figure 5.12: Reconstruction results for different signal to noise ratio with $N_s=128$ and $N_{\theta}=128$ . (a) SNR=infinite, (b) SNR=10, (c) SNR=30, (d) SNR=100 .....	101
Figure 5.13: The intensity map of the 128X128 phantom shown in Figure 5.12. The numbers shown are intensities of respective regions. The projection data are gathered using a parallel beam geometry with $N_s = 128$ .....	102
Figure 5.14: The relationship between slice and three dimensional reconstruction result.	103
Figure 5.15: Flow chart for the three dimensional reconstruction procedures.....	104
Figure 6.1: Determination of the readout noise and gain of the CCD camera system using measurement of the variance in the dark current. ....	109
Figure 6.2: The mean as a function of exposure time at $-34^{\circ}\text{C}$ . ....	112
Figure 6.3: The variance in the image as a function of the exposure time. Results are shown for the temperatures of $-34^{\circ}\text{C}$ , $-40^{\circ}\text{C}$ , $-44^{\circ}\text{C}$ , $-48^{\circ}\text{C}$ , to $-50^{\circ}\text{C}$ .....	113
Figure 6.4: Schematic representation of (a) a general system; (b) a linear system; (c) a linear and stationary system. ....	115
Figure 6.5: Derivation of the MTF from the edge response curve .....	119
Figure 6.6: Two kinds of collimators. (a) Cadmium cylinder. (b) B4C painted aluminum.	120

Figure 6.7: Modulation transfer function of the detector with B <sub>4</sub> C painted aluminum collimator and without collimator. ....	121
Figure 6.8: Neutron radiographic image for two pieces of Cadmium with 3 minute exposure time. ....	122
Figure 6.9: Polyethylene samples with the same size but different thickness. ....	122
Figure 6.10: Neutron radiographic image for polyethylene with thickness of .125 mm, .5 mm, .75 mm, 1.5 mm and 2.125 mm. ....	123
Figure 6.11: Neutron radiographic image of a piece of aluminum lap joint from a KC-135. ....	126
Figure 6.12: Same as Figure 6.11, except with photo negative, the bright area in Figure 6.11 becomes the dark region in this picture. ....	126
Figure 6.13: This is the picture of the same lap joint without filtering or equalization, but with rotation of 45 degree. A region of interest was chosen to cover the two dark strips and the average pixel value for each column of the rectangle was calculated. ....	127
Figure 6.14: Tomographic reconstruction results for the metalwrench socket and the chicken bone. The hight is equivalent to the 140th cross sections by pixel counts. ....	128
Figure 6.15: The radiographic image for the metal wrench socket and the chicken bone at 0° ....	129
Figure 6.16: The radiographic image for the metal wrench socket and the chicken bone at 160° ....	129
Figure 7.1: Basic coil component for surface scanning eddy current testing. ....	133
Figure 7.2: Thermal wave image system. ....	135
Figure A.1: Photodetection using silicon. ....	140
Figure A.2: Two phase transfer operation. ....	142
Figure A.3: The four steps for CCD image sensor operation. ....	143
Figure A.4: Typical spectral responses for a) a photodiode, b) a photoMOS, c) the human eye for reference. ....	144

# List of Tables

Table 2.1: Linear attenuation coefficients ( $\text{cm}^{-1}$ ).....	24
Table 2.2: Radioactive ( $\alpha$ , n) source. ....	30
Table 4.1: Model DL-1 system specifications .....	70
Table 6.1: The raw data of mean, RMS and standard deviation for different exposure time at $-34^{\circ}\text{C}$ . ....	111
Table 6.2: The raw data for new mean, RMS and variance for different exposure time at $-34^{\circ}\text{C}$ .....	111
Table 7.1: Comparison of the best performance of three type neutron sources with our AccSys Technology model DL-1 RFQ.....	131

# Chapter 1

## Introduction

Neutron radiography and tomography allow scientists and engineers to inspect and evaluate industrial materials in a nondestructive way. This technology provides a new field for nondestructive testing and evaluation. Neutron radiographic and tomographic images have been used for many applications, such as, the detection of corrosion in aircraft components, plant research, the inspection of electrical components, and the visualization of fluid flow. In Japan, scientists even used a neutron radiographic imaging system to monitor the "cold fusion" processes. However, due to the limitations of the neutron source, most of the research up to this point has been done in the laboratory rather than in the field. It is important to develop portable neutron sources for practical radiographic and tomographic imaging systems. If we want to do a corrosion inspection on aircraft, it is almost impossible to fly a plane to a nuclear reactor to do the test; at the same time, the radiation issue makes it impossible to build a reactor in the airport to inspect the aircraft.

In this research work, a portable neutron radiographic and tomographic image system was designed and built. An AccSys Technology model DL-1 radiofrequency quadrupole (RFQ) accelerator neutron source was used. An  $^6\text{LiF-ZnS}$  scintillator screen was mounted to transfer the neutron information into photon information. Two optical

systems were selected to focus the image onto an electro-optical cooled charged coupled device (CCD) chip.

## **1.1 Main contributions of the thesis**

The highlights of the significant contributions made by this thesis work are summarized as follows:

The first contribution of this thesis is the design and the installation of a portable accelerator based digital neutron nondestructive test image system. Neutrons have proved to be a powerful tool for nondestructive testing and evaluation both for science and engineering. In order to get high quality images, reactor neutron sources have been used in the past. Radiographic and tomographic imaging systems using reactor neutron sources have already made great contributions to scientific research work in this field. For practical applications, we need a nondestructive test system that is moveable, instead of one that remains in the laboratory. It is clear that if we want to detect the presence of corrosion on any part of an aircraft, our testing equipment must be portable. A portable neutron imaging system lets a nondestructive test step out from the laboratory and move into the real world. This step has significant meaning not only for science but also for engineering. The benefits apply to the aircraft industry, but they are also important to human beings as a whole, since aircraft safety is an important issue to everyone.

The second contribution of this thesis is the development of an electronic digital imaging system for neutron radiography and tomography. Traditionally, people store their images on films, which are very expensive and difficult to do any imaging processing. Our digital imaging system has great advantages over the traditional film image system; in our system, a computer controls the camera and saves the images digitally. In this way, not only is film eliminated, but also image processing on the stored digital images becomes reality.

The third contribution of this thesis is the development of a method to characterize the image quality for the whole imaging system. In order to determine the resolution of the imaging system the modulation transfer function (MTF) was measured. The dark noise for the CCD camera was measured and the read out noise for the charged coupled device (CCD) camera was also calculated from experimental data. The gain and dynamic range of the CCD system were measured.

The fourth contribution is the development of the software for three dimensional reconstruction for our neutron imaging system. The three dimensional reconstruction software was developed and tested on our Silicon Graphics 4D/240GTX workstation. A new reconstruction technique, multiple scale simulation reconstruction, developed by M. Bhatia [47] was also put into our reconstruction software; therefore, we can get multiple scales simultaneously. The advantage of this technique lies in the ability to trade off reconstruction time and resolution during initial fast scanning to discover possible problems in the object under investigation by a fine scale reconstruction which could be used to extract edges and features. In conventional tomography, a complete high resolution reconstruction is made, followed by post processing of the image to extract features. With multiscale reconstruction an initial quick reconstruction could be made to determine areas of corrosion, followed by a subsequent interactive zooming in on the region of interest at high resolution if corrosion is detected. The performance of the reconstruction software was tested by x-ray.

The fifth contribution of this research work is the design of the collimators for this portable neutron imaging system. Collimation is an important procedure for an imaging system which uses an accelerator based neutron source, since the neutrons which come out from the accelerator are not parallel; thus in order to get reasonable resolution for the image we have to use collimator. The collimator can evaluate and eliminate neutron scattered components from the digital image.

The final contribution of this research work is a preliminary attempt to apply this imaging system to non-destructive tests for corrosion detection of aircraft aluminum lap joint parts from an aging KC-135 aircraft.

## **1.2 Thesis outline**

The thesis is organized as follows. In Chapter 2, the current status of corrosion problems in industries, particularly, in the aerospace industry, and possible detection methods are presented. A historical overview of the development of the neutron radiography and tomography is given also in Chapter 2. In Chapter 3, the imaging system design for our experiments is described. This chapter also includes the design of neutron detection system, optical system design and the CCD camera. Other equipment, turn table and translator, for doing tomographic imaging are also described. In Chapter 4, a general review of the development of the accelerator neutron sources is discussed. The AccSys Technology model DL-1 RFQ accelerator, the key equipment for our portable neutron imaging system is also presented in this chapter. In Chapter 5, 3-D reconstruction methods for our tomography system are discussed. We first present the difference between radiography and tomography and then point out that tomographic reconstruction is a bridge between two dimensional projection data and three dimensional object distribution function. Two reconstruction methods are discussed specifically. Also we discuss 3-D reconstruction software development for our neutron tomography image system on our Silicon Graphics 4D/240GTX workstation. In Chapter 6, the detector's performance was measured in terms of dark noise, readout noise, gain of the CCD camera, dynamic range and the spatial resolution for this imaging system. The design of the moderator and collimator is discussed. The moderators were designed and installed. The major difference in a reactor source and an accelerator source is that the flux of neutrons from reactors are higher even with large L/D ratios (L/D, the length to diameter

ratio of collimators is a traditional measure of parallelism for neutron work). Even though the number of neutrons coming out from our accelerator is in the order of  $10^{10}$ n/sec, they are essentially isotropic, only those parallel thermal neutrons can make useful contributions to our images. Collimators were designed and tested in our experiments and the results are presented in this chapter also. In Chapter 7, the discussion of this thesis work is given and the future work for this project is also pointed out. A final note for comparison of our portable neutron imaging system with other corrosion detection image technique is given to show a clear advantage of our system over others in aircraft corrosion detection application.

# **Chapter 2**

## **Corrosion problems and the solutions**

In this chapter, the current status of corrosion problems in industries, particularly, in the aerospace industry, and the possible detection methods are presented. First, the possible and common damages due to corrosion are reviewed. Secondly, the solutions to avoid these accidents and how to reduce these damages, and the early detection of corrosion and cracking in a metallic material are discussed. Third, the reasons for using neutrons to do early corrosion detection instead of using X-rays are explained. Finally, a general historical development of neutron radiography and tomography is briefly reviewed.

### **2.1 Corrosion problems**

The degradation of industrial materials by environmental influences is a problem of the great concern among designers, engineers and users because of its potential impact on human safety and on extremely expensive equipment. Corrosion can be defined as the degradation of a metallic material by an electrochemical reaction with the environment [1].

Corrosion can directly lead an engineering component to failure, it also can cause serious degradation in mechanical properties by indirect actions through the corrosion

reaction products. The presence of hydrogen in metals and alloys can result from a corrosion reaction, which cause significant changes in mechanical properties, such as hydrogen-induced embrittlement. Generally speaking, there are three kinds of phenomenological mechanisms that can be attributed to the degradation of a material in which hydrogen plays an important role:

- 1). Surface corrosion with formation of hydrogen-compounds (e.g. Aluminum) ;
- 2). Stress corrosion cracking, where an anodic dissolution with formation of hydrogen occurs along the crack ( $\text{Metal}^+ + \text{H}_2\text{O} \rightarrow \text{Metal-OH} + \text{H}^+$ ) ;
- 3). Hydrogen embrittlement with the reduction of the ductility of a metal by hydrogen atoms or molecules in the granular structure of the material [2, 3].

Figure 1 shows an aircraft damaged due to corrosion and corrosion fatigue [4]. Commercial and military airplanes are exposed to highly corrosive environments all over the world. Usually, corrosion is the result of hydrate formation on the surfaces between two bonded or riveted aluminum plates. The stability of the connection is decreased and the structure is weakened by corrosion. This early detection of corrosion products in order to avoid failures is a major problem to be solved.



Figure 2.1: An aircraft damaged due to corrosion [4].

In the military, some aircraft are very expensive, such as the B-1B strategic bomber, which costs over \$800 million each. Military aircraft are flown throughout the world and are therefore exposed to the most severe corrosive environments on earth. On modern combat aircraft, composite materials and mixed structures (plates and honeycomb) are in widespread use, bonding these materials together is becoming more and more frequent, and also more and more challenging. Ingress of moisture or condensation causes corrosion and separation of bonding layers, leading to a weakening of the structure. Early detection of degradation is crucial to enable effective repairs and to avoid more expensive damage. There are significant numbers of military and commercial airplanes which have been in operation for more than 25 years (see Figure 2.2); the economical incentive to repair these planes rather than replace them makes detection of corrosion and repair an increasing objective [5, 6]. As the average age of many of the world's airline fleets has increased, evaluation of the "safeness" of these aging aircraft by maintenance personnel has become increasingly urgent.

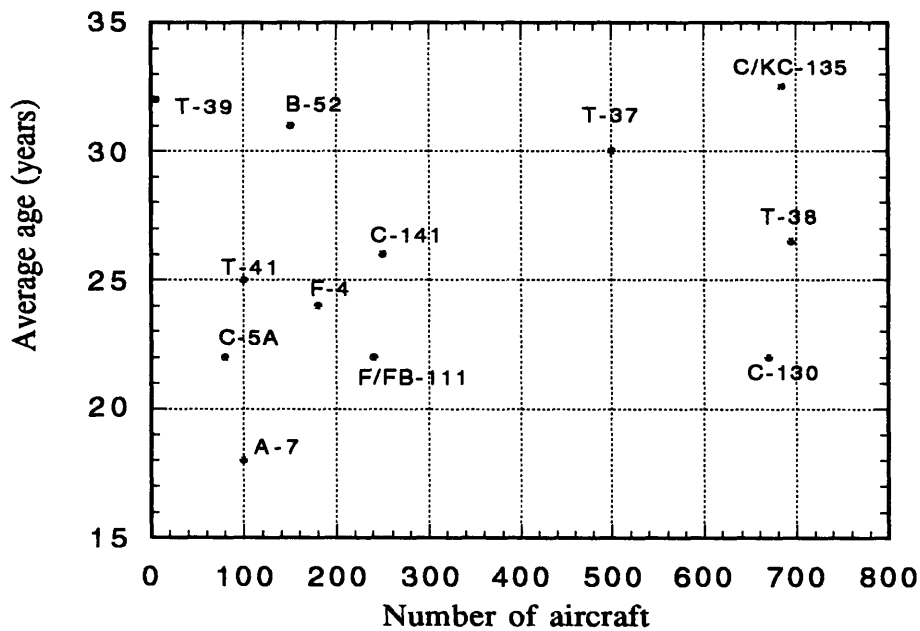


Figure 2.2: Military aircraft age tally (up to Sept. 92).

In nuclear power plants, a multitude of pipes are used to transport fluids at various temperatures and pressures, such as superheated steam and hot water. These environments can easily introduce corrosion to the pipes. Additionally, these pipes are one of the barriers between fission products in the primary coolant system and the outside environment. Due to the internal and external forces acting on these pipes, hydrogen embrittlement can easily happen. Detecting the degradation of the pipe before damage occurs is not only an operational consideration, but also an important issue for nuclear safety.

For ocean transportation of crude oil and other goods, the most obvious form of environmental attack on the supertanker and the ship is corrosion-related. Stress corrosion cracking occurs in the heat affected zone around welds, but hydrogen embrittlement can occur anywhere because of ocean environment. Loss of ductility due to embrittlement seriously impairs the capability of the ship to absorb the loads of a rough sea or large swell, therefore parts can be broken easily.

In the petrochemical industry, large refineries use hundreds of miles of pipes and a multitude of reaction vessels to contain hydrocarbon-compounds at high temperature and pressure. This makes the materials used for the construction degrade very easily by hydrogen. An embrittled region in the pipe is a potential breaking point. Pipe breaks can lead to loss of products, pollute the environment and cause a serious risk to human life.

## **2.2 Solutions**

By reviewing all the problems mentioned above, one can see that it is very important to detect and quantitatively characterize the corrosion in metals. How can we do this? One answer is to use the neutron tomographic image technique.

Neutrons have unique interaction properties that make them ideal for imaging many important engineering materials. When neutrons interact with a nucleus, a common

process by which neutrons are removed from a beam is through elastic scattering or by absorption where the incident neutron is the nucleus, forming a transient compound nucleus. The nucleus thus gets energized to an unstable excited state. When the excited nucleus gives up its excess energy, there are several things that can happen, each with a given probability dependent on the type of nucleus and the kinetic energy of the incident neutron. The compound nucleus may 1) re-emit the incident neutron with its energy unchanged but heading off in a different direction, 2) emit a neutron with more or less energy than the incident neutron (inelastic scattering), 3) emit a proton, alpha particle, more than one neutron, or a photon (charged-particle emission), 4) the compound nucleus de-excites itself by emitting a  $\gamma$  ray (neutron capture) or 5) fission into two or more lighter nuclides.

The probability of each of these reactions from a neutron interaction is quantitatively described by a value known as the nuclear cross-section, with units of  $\text{cm}^2$ . The cross section  $\sigma$  is a function of the type of reaction, neutron energy, and target nuclide [7]. Microscopic cross-section with units of  $\text{cm}^2$  is an effective area used to characterize a single nucleus. It is a probability per unit nuclide density and per unit thickness of material through which the neutrons travel. There is also the linear attenuation coefficient,  $\Sigma$ , with units of  $\text{cm}^{-1}$ . It is simply the product of the microscopic cross-section and the atomic number density of a material. The macroscopic cross-section is the probability per unit distance that neutron will interact with a material; therefore, it also is a function of reaction type, neutron energy, and target nuclide [8].

Planar radiography using neutrons was developed to take advantage of their scattering and absorption properties to study structure and flaw development as a means of non-destructive testing of materials [9, 10, 11]. In traditional medical X-ray imaging, the main matrix materials consist of light elements such as hydrogen, and the components which need to be imaged are high density materials, such as bone. X-rays and other electromagnetic radiation, however, are strongly absorbed by metals and other

engineering materials. Large thickness of metals and other important industrial materials can be penetrated with neutrons and the spatial distribution of elements such as carbon and boron can be determined.

Due to the lack of electrical charges, neutrons are able to interact with nuclei in a large number of ways, and in ways quite different from charged particles and X-rays. Neutrons can easily penetrate the electron cloud of an atom and interact with the nucleus. Neutrons, even with very low energies, in the meV range, can interact with nuclei too. For charged particles, due to the electron cloud, a proton or alpha particle must have energy in the MeV range to interact with the nucleus of even light elements. As for the X-ray, it interacts primarily with the surrounding electron cloud, not the nucleus.

From a physical point of view, the basic interaction with target materials for X-ray and neutron are totally different. For neutron, it is a nuclear interaction; for X-ray it is electromagnetic interaction. Figure 2.3 is a plot of the mass absorption coefficients as a function of atomic number for thermal neutrons and 20 keV X-ray [12]. Here the mass absorption coefficient is equal to the linear absorption coefficient divided by the atomic density.

It is clear that there are large differences in the neutron mass attenuation coefficients for certain elements compared to X-ray. For X-ray, with increases of the atomic number the mass absorption coefficients increase slowly and continuously, while for neutrons, there are significant changes in the mass absorption coefficients with different elements. Depending on the material being imaged, neutron imaging can have great advantages over X-ray imaging, but the neutron imaging technique cannot replace the X-ray imaging technique in some applications. The neutron imaging technique will make its own special contribution to some special applications. Samarium and neodymium, for example, are common components of modern permanent magnets, which are finding wide applications within systems such as automobile starting motors

and high-speed train running assemblies. Such materials are ideally imaged within heavy metal structures because of their high neutron absorption cross section. The ability to study the internal structure of these and other systems non-destructively is uniquely provided by neutron imaging.

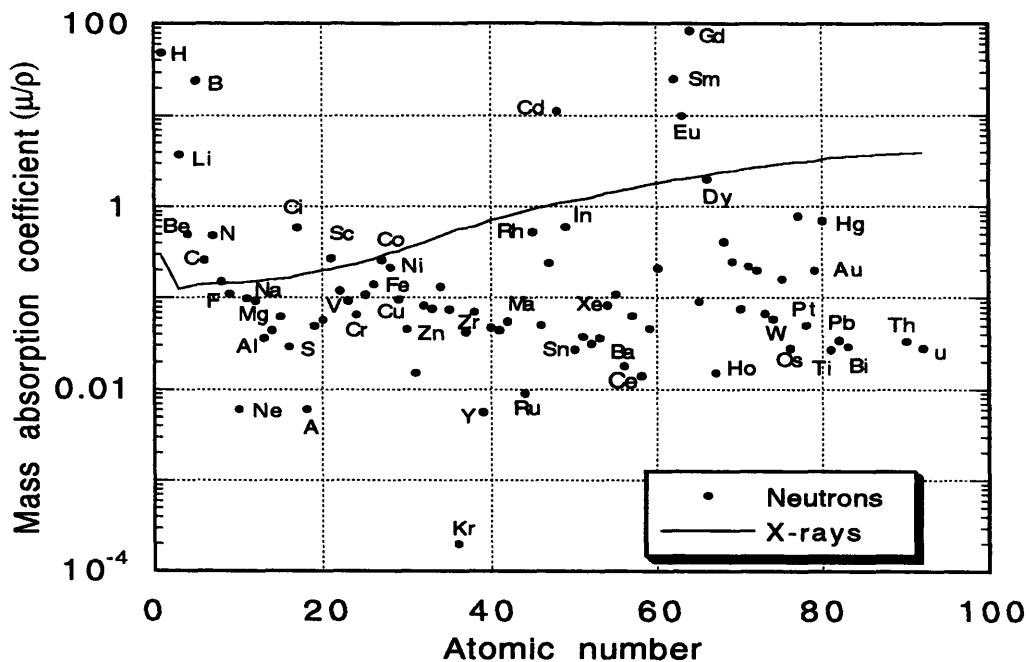


Figure 2.3: Mass absorption coefficients( $\text{cm}^2/\text{g}$ ) as a function of atomic number for thermal neutrons and 20 keV X-ray [12, 13, 14].

Neutrons are an ideal probe for detecting corrosion in aluminum. The reason is that the sensitivity of any radiographic system depends on both the quantity of corrosion and the attenuation characteristics of the corrosion products to the probing radiation. Table 2.1 [15] shows some of the linear attenuation values for X-rays and neutrons at different energy levels. Note that for low energy X-rays, the attenuation coefficients for both aluminum and its corrosion products are somewhat different, whereas a dramatic difference is seen in the neutron absorption coefficient, especially if subthermal neutrons

are used. Unfortunately, the large absorption coefficient for aluminum at 30 keV precludes the use of low-energy X-ray for examining thick structures. At the higher energies required for penetration, the X-ray absorption coefficients are closer, and contrast is essentially determined by density variation. In the case of X-rays, the ratio of absorption coefficients for corrosion products ( $\Delta\mu/\mu$ ,  $\mu$  of aluminum is normalized to one) is between 0.5 and 0.72, whereas for thermal neutrons the corresponding ratios are 27.8 and 17.4 and for subthermal neutrons, 48.7 and 52.3. The large interaction cross-sections for thermal neutrons mean there is a large differential attenuation of a neutron beam, and therefore, greater contrast in the radiograph. As a result, even very thin layers of corrosion may be imaged and so the detection of corrosion products in aluminum is particularly well suited to the use of neutron radiography and neutron tomography.

Table 2.1: Linear attenuation coefficients ( $\text{cm}^{-1}$ ).

Materials	Density $\text{g/cm}^3$	X-ray (30 keV)	Thermal Neutrons( $\text{cm}^{-1}$ )	Subthermal Neutrons( $\text{cm}^{-1}$ )
Aluminum	2.7	3.0	0.861	0.086
$\text{Al(OH)}_3$	2.53	1.501	2.40	4.190
$\text{AlO(OH)}$	3.014	2.16	1.50	4.5
Water( $\text{H}_2\text{O}$ )	1.00	0.368	2.706	4.55
$\text{Al(OH)/Al}$		0.38	27.87	48.72
$\text{AlO(OH)/Al}$		0.72	17.42	52.33

Other specific applications ideally suited to imaging with neutrons are in materials with constituents or components made of light nuclei such as hydrogen, carbon, magnesium, boron, or lithium within a matrix or structure consisting of heavy elements such as uranium, zirconium, gold, silver, cadmium, tungsten or lead. Neutron radiography has been successfully utilized to study the distribution of boron in

zirconium-based nuclear reactor control rods. An ideal application of neutron tomography is in boric materials (boron nitride reinforced aluminum), which are used widely in the aerospace industry. Additionally, high contrast imaging is possible in hydrogen containing compounds such as plastics, rubber, and wood.

## **2.3 Historical review**

The concept of radiography using neutrons was first introduced by Kallman and Kuhn in Berlin [11] a few years after Chadwick's 1932 discovery of the neutron. In the years 1935 to 1938, they used a small accelerator approximately equivalent to a 2 to 3 gram Ra-Be source for the pioneering studies, and over the next ten years a number of patents were filed, recording the basic principles of neutron radiography [16]. The first neutron radiographs published in 1946 came about as a result of the German efforts to create nuclear energy after the discovery of nuclear fission by Hahn and Strabman [17].

After World War II the advent of nuclear reactors brought about the next development in neutron radiography. The first reactor source neutron radiographs were produced in 1956 by Thewlis and Derbyshire [11] at Harwell. The intense neutron beam of the BEPO reactor allowed them to produce radiographs of high quality in short periods of time. These studies also demonstrated the applications of neutron radiography to specific problems of flaw detection in uranium cylinders and boron-aluminum composites. The technique has continued to evolve and develop slowly for an increasing number of applications due to the outstanding work of Berger and Barton [11].

### 2.3.1 The historical development of the neutron sources

It seems appropriate to begin our historical review by discussing neutron sources, for at least two reasons. First, the neutron source is an obvious first consideration for anyone interested in actually performing neutron radiography and tomography. The image quality is often limited by the neutron source. The other reason is that the type of the neutron source which people use in their imaging system determine the practical applicability of the imaging system, e.g. if an imaging system was designed by using reactor neutron source, then the imaging system can not be used as a portable system.

Chadwick [ 18] first produced neutrons in 1932 by interactions in beryllium of alpha particles from decay of natural polonium. Nuclear fission reactions [19] were the next generation of sources (beginning with CP-1 in 1942). So far the thermal neutron fluxes produced by research reactors are generally in the order of  $10^{15}$ n/cm<sup>2</sup>-sec, operating at powers on the order of 100 MW. The most advanced reactors now being contemplated for fluxes close to  $10^{16}$ n/cm<sup>2</sup>-sec. Figure 2.4 [20] shows the evolution of the effective thermal neutron flux from available neutron sources. The peak flux is used to approximately characterize the pulsed sources.

Let us consider radioactive source first. The neutrons available from radioactive sources are primarily high energy neutrons, and problems involving moderation and collimation in order to obtain thermal neutron beams for radiography are encountered. Hennelly [21] (1961) has described an Sb-Be neutron source capable of a total yield of  $10^{10}$  n/sec. A neutron yield of this magnitude, appreciably higher than that which can practically be achieved from other available radioactive neutron sources, has attracted interest from groups concerned with several application areas, including neutron radiography.

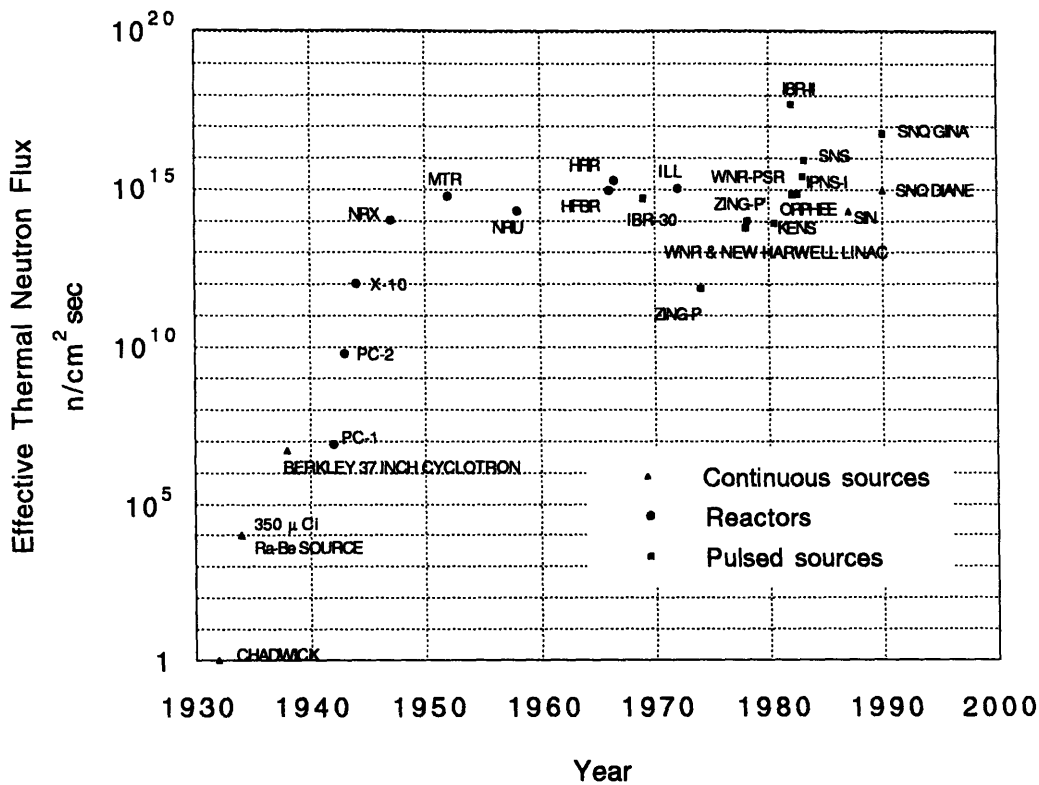


Figure 2.4: Evolution of the effective thermal neutron flux from available neutron sources.

Warman's work [22] (1962) with a  $10^{10}$  n/sec Sb-Be source indicated that such a source might not only be useful for neutron radiography, but it also offered an advantage as a portable type source. Since the source does not emit neutrons until the antimony and beryllium are brought together, Warman was able to design a simple gamma radiation shield for the radioactive antimony. Additional neutron shielding would not be necessary until the source was actually being used because it was only then that the antimony and beryllium were brought together. The basic features of this design are illustrated in Figure 2.5.

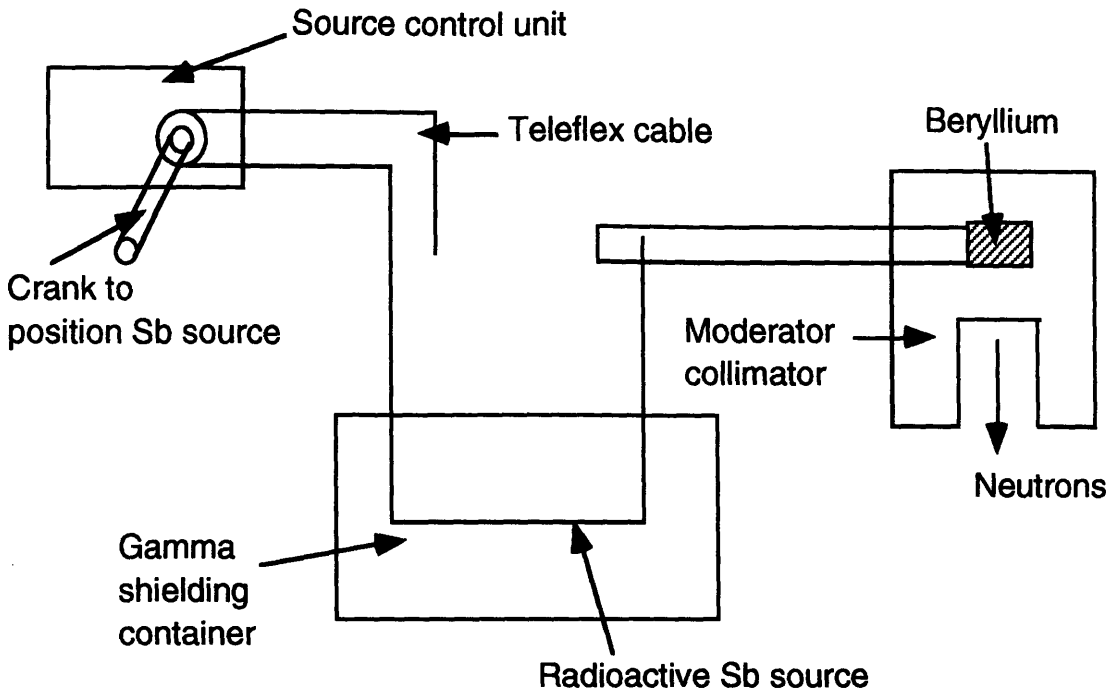


Figure 2.5: Diagram of a proposed portable neutron source of the Sb-Be type.

After Warman (1962) [22].

Warman's neutron radiography investigation using an Sb-Be source was encouraging for two reasons. One is that it did offer the hope that a portable source could be made available at a reasonable cost. Hennelly (1961) had previously estimated the cost of the basic source at an initial value of \$3500 (1961 \$), with an additional amount of \$5000 per year being necessary to maintain the source at a high output level. This latter amount would cover the cost of additional neutron irradiation of the decayed  $^{124}\text{Sb}$ . This would be necessary in the case of  $^{124}\text{Sb}$ , because the two month half-life would produce a 64-fold decrease in source output during the course of a year, unless the antimony was reactivated by neutron irradiation.

The other encouraging fact brought out by Warman's study was that the low energy neutrons yielded by this source could be easily moderated and would therefore yield a fairly high intensity thermal neutron beam. Using the moderation and collimation

configuration shown in Figure 2.6, Warman was able to obtain a fairly well collimated thermal neutron beam having an intensity of about  $10^6$  n/cm<sup>2</sup>-sec from a  $10^{10}$ n/sec total neutron yield source. Admittedly, a good radiographic source would require better collimation in order to produce radiographs of reasonable quality. However, one would hope that this improved collimation could be accomplished in a manner such that the additional neutron beam intensity loss could be held to about a factor of 10. A portable neutron source which would produce a thermal neutron beam intensity of  $10^5$  n/cm<sup>2</sup>-sec would be extremely useful.

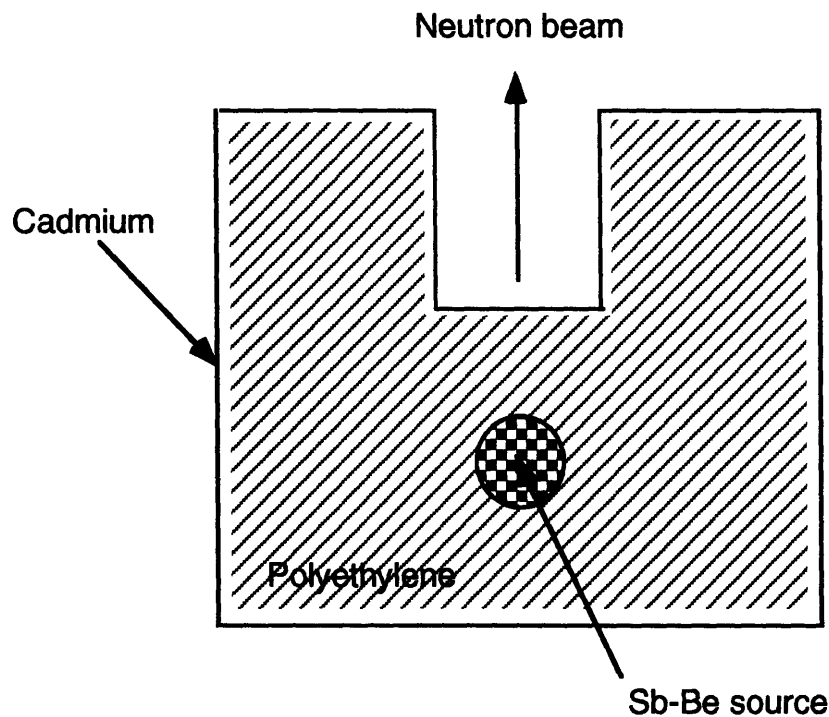


Figure 2.6: Polyethylene moderator and cadmium collimator used with an Sb-Be neutron source for radiographic studies by Warman (1962). The diameter of the neutron port is 2 inches, the depth of the port is 3 in. A source configuration such as this, with a  $10^{10}$  n/sec Sb-Be source, yielded a collimated thermal neutron beam intensity in excess of  $10^6$  n/cm<sup>2</sup>-sec.

One disadvantage of this source, namely the short half-life, has already been pointed out. Another disadvantage is that the gamma radiation background from this source, and from other ( $\gamma, n$ ) sources would naturally be expected to be very high. This would probably limit the use of such sources to detection systems which did not respond to gamma radiation.

This problem is actually present in the case of most radioactive sources, although the data shown in Table 2.2, a list of common ( $\alpha, n$ ) radioactive neutron sources, might mislead one into thinking otherwise. We must recall that the favorable  $\gamma/n$  ratios shown in Table 2.2 involve the fast neutron yield of the source. Moderation and collimation will reduce the neutron intensity and will probably increase the gamma intensity because of prompt ( $n, \gamma$ ) emission from materials in the neutron path. Therefore gamma to thermal neutron ratios available from radioactive sources will be relatively high, with the possible exception of the Polonium-210 and Americium-241 sources which, as indicated in the table, have an extremely low gamma background.

Table 2.2: Radioactive ( $\alpha, n$ ) source.

	Yield		$\gamma/n$ Ratio
Source	$10^6 n/\text{curie-sec}$	Half-Life[i]	$\text{mRhm}/10^6 n[\text{ii}]$
Ra- $\alpha$ -Be	17	1620 y	57
Rn- $\alpha$ -Be	15		65
Ra- $\alpha$ -B	6.8	1620 y	14
Po- $\alpha$ -Be	3	138.4 d	0.012
Am- $\alpha$ -Be	3	458 y	<0.1
Ac- $\alpha$ -Be	1.5	22 y	8
Th- $\alpha$ -Be	20	1.91 y	30

[i] Half-life units are days, d, and years, y.

[ii] The ratio of gamma intensity to neutron intensity is given in terms of milli-Roentgen per hour at a meter per  $10^6$  neutrons.

The yields from radioactive sources in general are approximately  $10^6$  to  $10^7$  neutrons /sec per curie of activity. Since it has been indicated that the use of such sources for thermal neutron radiography appears to require a total fast yield of at least  $10^{10}$  n/sec to obtain a reasonable intensity thermal neutron beam, we can readily see that radioactive source intensities in terms of kilocuries are necessary. This fact tends to eliminate from further consideration most of the materials mentioned, because of availability, half-life, or economic factors. The Sb-Be source appears to be the best radiographic radioactive neutron source presently available, in spite of the shortcomings of that source. As far as the future is concerned, one promising possibility is the californium 252 spontaneous fission source which has been reported to be capable of providing a  $10^{11}$  n/sec yield from a 30 mg source with a half-life of 2.2 years (Anon [23], 1956), but this source is too expensive.

At the present stage of neutron source development, it cannot be denied that the highest quality neutron images produced have been made using reactor neutron sources. The high thermal neutron beam intensities available from such source already reached as high as  $10^{16}$  n/cm<sup>2</sup>-sec (see Figure 2.4).

We will give a detailed description of the development of our accelerator source in Chapter 4.

### **2.3.2 The historical development of the neutron tomography**

With the development and application of the computer, people realized that planar radiographic techniques are limited due to the nature of the image procedures. Density variations in the radiograph (two dimensions), which constitute the image, represent the

integrated interaction cross-section over the entire path of radiation through the object. Details of internal structure and volumetric information are easily hidden in this effective averaging.

Tomography using the method of image reconstruction from projections allows two- and three-dimensional details to be retained and the object to be visualized in cross-section, retaining the spatial distribution of radiation attenuation and thus the details of the object's internal structure [24]. Attenuation differences as little as 0.02% have been measured with computer-aided X-ray tomography. This precision is essential in medical imaging, which relies on very small differential X-ray absorption between normal and diseased tissue. Neutron-computed tomography (NCT) imaging will be considerably less restricted because differences in neutron cross-section will often vary by orders of magnitude, thus NCT offers the potential of tremendous increases in the sensitivity of non-destructive testing.

The advantages of neutron tomography over radiography were realized in the early 1980's and prototype systems assembled and tested. Barton [11] *et al.* first used neutron tomographic reconstruction from radiographs obtained at several angles to examine nuclear reactor fuel bundles having 217 pins in a hexagonal array. The experimental beam penetrated the equivalent of approximately 9 fuel pins having a total attenuation length of 47 cm. The system resolution was on the order of a few millimeters. Later, the results of experiments performed in Japan at Nagoya University by Matsumoto and Krata [25] were presented in the Proceedings of the First World Conference on Neutron Radiography, which was held in 1983. Two types of neutron sources were used for the tomographic imaging experiments. The first experiments used a 2 MeV Van de Graft accelerator as a thermal neutron source. The detector was a combination of gadolinium converter foils (25  $\mu\text{m}$  thickness) and emulsion film (Kodak Type AA). One film was used for each projection angle. The source fluence was  $1 \times 10^8 \text{ n/cm}^2$ , over

typical sample exposure times of approximately 20 to 30 minutes per angle. The samples studied were made of 10 mm thick aluminum plate with various holes having diameters of either 30 mm or 40 mm. Data for each projection was obtained by scanning the exposed film with a microdensitometer at 0.2 mm or 0.4 mm intervals, and converting the density to neutron fluence using a relation obtained experimentally. Only 18 projection angles (at 10 degree intervals) were used due to the long exposure times and the time required to scan each radiograph with the microdensitometer.

Data were processed using a FACOM 200 type computer using the Simultaneous Iterative Reconstruction Technique (SIRT) or the Convolution Integral Method with appropriate filter functions. Resolution in the final tomograms was limited to 1.2 mm.

In their second series of experiments, the Japan Research Reactor No. 4 was used as the neutron source. This 2.5 MW swimming pool-type reactor delivered a thermal neutron flux of approximately  $2 \times 10^7$  n/cm<sup>2</sup>-sec. Again, the detector was a gadolinium-foil converter and emulsion film (Fuji Mini Copy film). Exposure time was reduced to 8 minutes; however, all other procedures remained the same as in the previous experiments. The image resolution was improved to 0.8 mm, primarily because of improved source collimation.

In later work presented in 1986 at the Second World Conference on Neutron Radiography in Paris, Matsumoto *et al.* [26] were able to improve upon their original technique by replacing the single films with a roll system in an automatic camera and by using the KUR E-2 reactor Facility (thermal neutron flux of  $1.2 \times 10^6$ n/cm<sup>2</sup>-sec). The camera had a gadolinium-foil converter which was in direct contact with the film. Sequential radiographs were taken on a single roll of film. The microdensitometer used in the previous experiments was replaced by a video camera to scan the optical density of the film. A convolution integral algorithm was used for reconstruction on a FACOM M-382 computer. In addition to the automatic camera, Matsumoto's group developed a

neutron television system, utilizing a gadolinium oxysulfide converter scanned by a video camera [26]. The images were recorded on conventional video tape and transmitted to a high-speed image processor (TOSPIX-2) for reconstruction. The resolution of an image reconstructed from 100 projection angles for the neutron television system was found to be about 0.4 mm.

Yoneda *et al.* at the Kyoto University Reactor (KUR) also developed a video camera-based tomography based on the same components as Matsumoto's group [26]. The KUR imaging system consisted of a neutron TV system, a video image processing system, a personal computer system (NEC PC-9801), and a stepper motor control and drive unit. The projection data were collected in transverse increments one pixel in size (about 0.75 mm to 0.80 mm). Twenty one projections covering 180 degrees were taken to reconstruct an axial image.

In resolution tests, the system was capable of detecting water in a 1.5 mm diameter water column hole embedded in a 9 cm aluminum cylinder. The contrast resolution was severely limited by the dynamic range of the system.

In France, Kusminarto and Spyrou at the Institute Laue-Langevin in Grenoble performed experiments with neutron tomography [27]. A thermal neutron reactor source with a flux of  $1.8 \times 10^{12}$  n/cm<sup>2</sup>-sec was used. Images of a test object were obtained using three experimental setups. The test object was a Teflon cylinder 10 mm in diameter. Two 5 mm diameter holes were drilled perpendicular to the axis of the cylinder. In one hole, brass and copper rods were inserted, separated by cadmium foil. Silver foil was fixed at one end of the hole, and indium foil was placed at the other end. The other hole was filled with copper and perspex rods.

In the first experiment, a well collimated He<sup>3</sup> proportional counter recorded the neutrons transmitted through the object over a period of 40 seconds. The counter was incremented along 19 positions to obtain complete projection information, made up of 19

ray sums, for each angle of rotation. Such data was obtained for 15 projection angles spaced at 12 degree intervals. The image was reconstructed using a filtered back-projection algorithm.

The second method used conventional direct radiography with a gadolinium-foil converter in contact with film. Thirty 10-second exposures evenly spaced over 180 degrees of rotation of the object were obtained. The radiographs from each projection were digitized using a computerized, video camera-based microdensitometer with a spatial resolution of 12 pixels per millimeter and a 256 gray-color scale. As a comparison, gamma-ray transmission tomography was also carried out on the same object using 60 keV gamma rays from a well-collimated Am-241 source. The transmitted photons were recorded using a NaI(Tl) detector collimated to 1 mm diameter. As in the case of the He<sup>3</sup> neutron detector, fifteen projections comprised of 19 ray sums were obtained over 180 degrees of the object. For the two neutron tomography experiments, indium, cadmium and silver were easily distinguished in the reconstructed image. However, the system was not sensitive enough to differentiate Teflon, brass, and copper. Furthermore, the solid angle subtended by the collimated He<sup>3</sup> detector was so large that a significant fraction of the scattered neutrons was also recorded, which degraded the image. The contribution of scattered neutrons can be suppressed and the statistical error controlled by adjusting counting time. Thus, a better image could be obtained by using the detector than by using film, which receives information from both transmitted neutrons and scattered neutrons incident upon the converter. The disadvantage of the He<sup>3</sup> detector was that only one slice of interest could be examined at a time. Comparatively, the gamma ray tomography of the object yielded little information.

In the United States, the majority of the neutron tomography research has been done at Argonne National Laboratories [28]. Initial studies were carried out in which the examination and testing of reactor fuel assemblies were developed. Their neutron source

was a 250 kW TRIGA reactor, which would deliver a beam having a high component of indium-resonance energy neutrons (1.4 eV) to the sample. Like the Japanese groups, the method was indirect and relied on the activation of indium foils shielded with cadmium thermal neutron filters. The foil was then used to expose emulsion film, which was then scanned and converted to digital data using a scanning microdensitometer. Typically 75 projection angles were used for their filtered back-projection reconstructions. Using this data, fuel assemblies of up to 255 fuel pins have been successfully reconstructed, with resolution of approximately 1 mm.

In 1986 at the University of Virginia [28], the capability to do neutron tomography was added to a real-time neutron radiography facility. Real-time neutron radiography was performed using a Precise Optics Neutron Image Intensifying System (neutron camera), which incorporated a Thompson CSF image intensifier. The neutron camera provided a standard video signal interfaced to a dedicated image processor (Science Applications Inc. Intellect 100). The experiments were performed using a parallel beam geometry by rotating the sample through 200 projection angles. Each projection radiograph was transferred to the image processor and stored. This system demonstrated a resolution of approximately 1.3 mm .

In 1991, a multi-dimensional neutron tomographic imaging device for non-destructive testing of materials and complex assemblies was built and operated at MIT by R.C. Lanza and E.W. McFarland [29, 30]. The experimental system was composed of a reactor neutron source, a turn table, a scintillator screen and a CCD camera. The system was tested under various conditions. The resolution for this system is 500  $\mu\text{m}$ . The significant achievement for this experiment is that they used a CCD camera detector system to replace the traditional film. A great advantage over film-based methods is an increase in the dynamic range by a factor of at least 100. This factor can be increased by further development of the system and by use of better CCD chips.

H.P. Leeftang and J.F.W. Markgraf did an experiment to detect the corrosion on aircraft components and hydrogen ingress on zircalloy fuel cladding tubes by neutron radiography in 1992 [15]. They used cold neutrons in order to enhance the differences in the attenuation coefficients between aluminum and hydrogen. They also tested the detection capabilities of a subthermal neutron system and looked at corroded aluminum aircraft components. The imaging system utilized a gadolinium screen with single coated X-ray film. They successfully detected surface, subsurface and pit corrosion in corroded aircraft components even with the limited dynamic range system.

# Chapter 3

## Imaging system

In this chapter, the imaging system for our experiments is described. A general background physical theory for a neutron tomographic image is given first. Then the minimum requirement for the neutron fluence to take an image is discussed. Neutron detection, object handling, and the optical system are also discussed. Another important piece of equipment, the CCD camera, is also described.

### 3.1 Background theory

For a nondestructive test it is important to know what you want to see and how to see it. What you want to see is a target and how you see it is a technique. In Chapter 2 we already discussed why we can use thermal or subthermal neutrons to detect corrosion. The physics involved in the process of visualizing corrosion in airplane materials is quite straightforward. When a neutron beam is directed onto the object, some of the neutrons are absorbed and some are scattered. The probability of absorption and scattering is expressed in terms of the concept of cross-section:

$$\sigma_{tot} = \sigma_a + \sigma_s \quad (3.1)$$

Where  $\sigma_{\text{tot}}$  is a function of the atomic number and the energy of the incident neutron. The neutrons which we used in our experiments are thermal and subthermal neutrons (i.e., the energies for these neutrons are smaller than 0.025 eV). The total cross-section for an element was determined empirically. Many of these cross-sections can be found in a series of handbooks called "Barn-books" (named after the unit of the cross-sections, 1 barn =  $10^{-28}$  m<sup>2</sup>).

It is very important to know the minimum fluence required to detect corrosion of a given area on a sample to be inspected, since in practice we can only produce a finite neutron fluence.

Consider a basic radiation transmission experiment: a fluence  $\Phi$  (particles/cm<sup>2</sup>) is an incident beam on an object of dimension  $D$ . The bulk object has an attenuation coefficient  $\mu$  (cm<sup>-1</sup>) and contains a feature of dimension  $\Delta x$  which has an attenuation coefficient  $\mu+d\mu$  (see Figure 3.1). We want to detect the difference  $d\mu$  in a volume element of dimension  $\Delta x$  based on our ability to distinguish between the number of particles  $N$  transmitted along adjacent particle trajectories. Figure 3.1 shows the basic principle for the transmission image. The difference in particles transmitted is

$$\Delta N = N d\mu \Delta x \quad (3.2)$$

where  $\mu$  is the attenuation coefficient of the bulk object with dimension cm<sup>-1</sup>. And

$$\mu = n \sigma \quad (3.3)$$

where  $n$  is the number of atomic density and has units cm<sup>-3</sup>.  $\Delta x$  is the dimension of the feature which we want to detect.

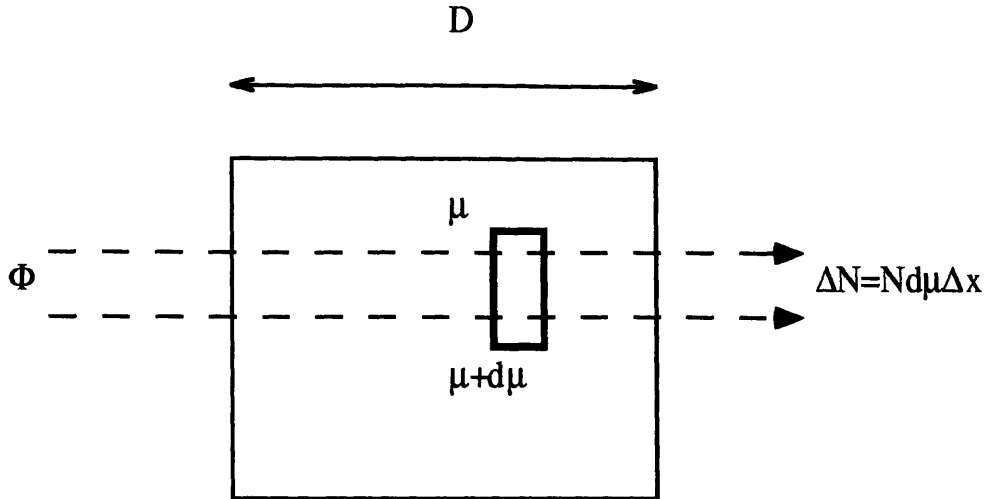


Figure 3.1: Principle of transmission tomography.

If we only consider the statistical error, i.e., the counts  $\sqrt{N}$ , then the signal which we can observe must be larger than the statistical error. (Later, we will prove that for our system the statistical error is the major contribution to the whole system error.) Clearly, if a system has too much noise, the detection results will be noise instead of the image which we want. So the following equation must be satisfied:

$$\sqrt{N} < N d\mu \Delta x \quad (3.4)$$

where  $N$  is the number of counts in a detect element with a size of  $\Delta x$ . If  $N = N_0 e^{-\mu D}$ , and  $N = N_0 \Phi(\Delta x)^2$ , the minimum detectable  $d\mu/\mu$  is:

$$\frac{d\mu}{\mu} > \sqrt{\frac{e^{\mu D}}{\Delta x^4 \mu^2 \Phi}} \quad (3.5)$$

equivalently the particle fluence,  $\Phi$  (particles/cm<sup>2</sup>), required to detect a difference  $d\mu/\mu$  is

$$\Phi > \frac{e\mu D}{\Delta x^4 \mu^2 \left(\frac{d\mu}{\mu}\right)^2} \quad (3.6)$$

Figures 3.2 and 3.3 show the required fluence  $\Phi$  as a function of  $d\mu/\mu$  and  $\mu$ .

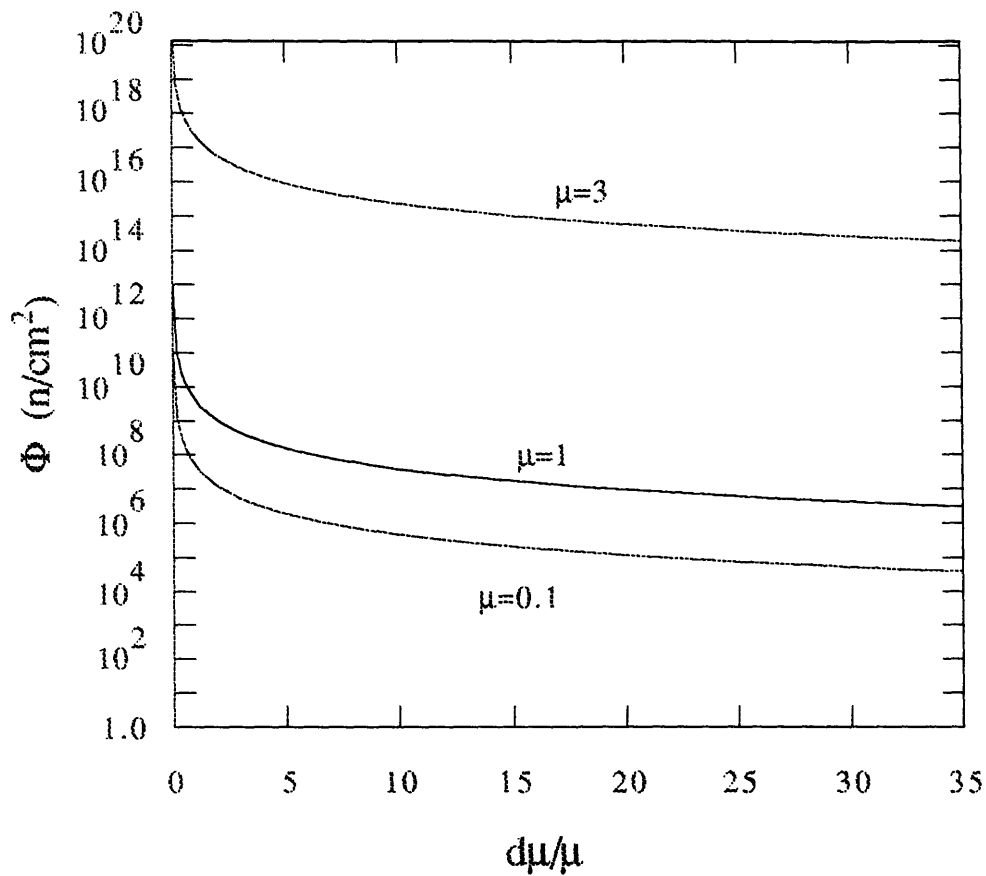


Figure 3.2: The relationship of particle fluence  $\Phi$  to differential attenuation for different attenuation coefficients  $\mu$  for a given object dimension of  $D = 10$  cm and a feature size  $\Delta x = 500$   $\mu\text{m}$ .

By using equation (3.6), we calculated the particle fluence  $\Phi$  as a function of differential attenuation for different attenuation coefficients  $\mu$  and a given object dimension  $D$ . Three cases are considered, i.e.,  $\mu$  equals 0.1, 1 and 3. We assume the object dimension is 10 cm and the corrosion size is 500  $\mu\text{m}$ . It is clear that a relative attenuation difference,  $d\mu/\mu$ , of at least 5, is desirable to minimize the number of particles needed to resolve the feature.

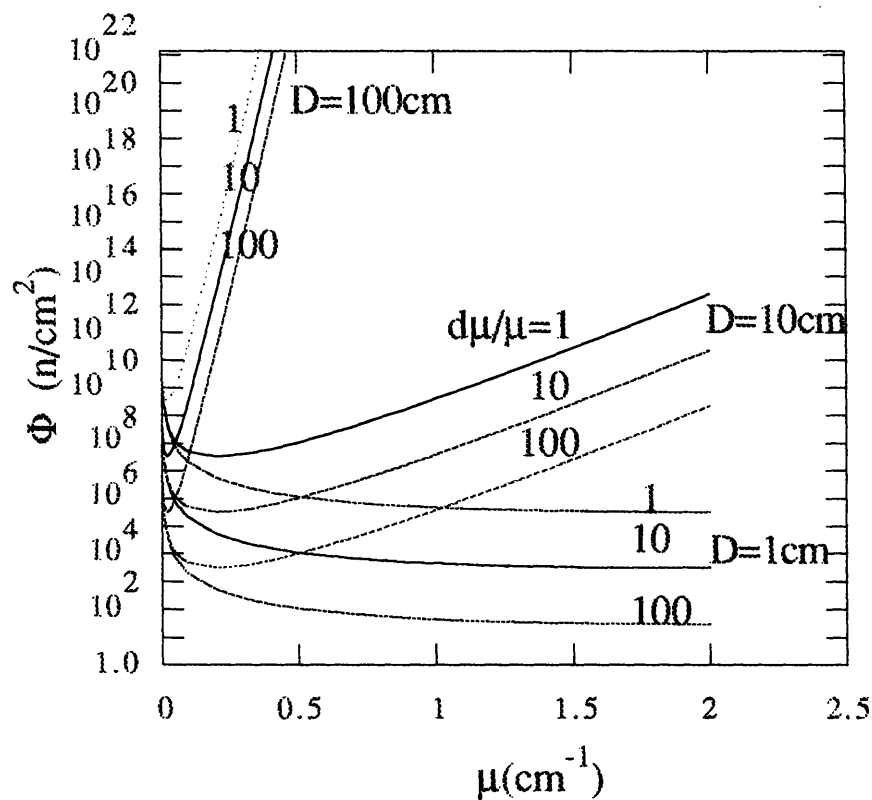


Figure 3.3: Relationship of particle fluence  $\Phi$  to attenuation coefficients  $\mu$  for different object dimension  $D$  and attenuation differences  $d\mu/\mu$ .

Figure 3.3 shows the necessary particle fluence  $\Phi$  as a function of attenuation coefficient  $\mu$  for different object dimensions  $D$  and different attenuation differences  $d\mu/\mu$ .  $D$  ranges from 1 to 100 cm and  $d\mu/\mu$  ranges from 1 to 100. The bigger the object is, the more fluence is needed to detect the corrosion. We can see that the matrix should be relatively transparent to the radiation with a value of  $\mu$  between 0.1 and 1.0  $\text{cm}^{-1}$  for minimum fluence. From Table 2.1, it is clear that for the detection of corrosion we have to use neutrons as the incident source instead of X-rays. We can also see that if we wish to image elements of corrosion in the order of 500  $\mu\text{m}$ , we should use a neutron fluence in the order of  $10^6$  to  $10^8$   $\text{n}/\text{cm}^2$ . From equation (3.6), we know that the fluence required to get the image is inverse to the fourth order of the corrosion size. For early detection of corrosion, it is important that we are able to achieve the resolution in the order of 500  $\mu\text{m}$  to 50  $\mu\text{m}$ , otherwise it would not be "early" detection of corrosion. If our imaging system could only detect a very large area of corrosion, it would be too late, since large corrosion parts produce cracks very quickly and the crack parts will cause mechanical failure. From an engineering point of view, we need a resolution for our imaging system in the order of 50  $\mu\text{m}$  to 500  $\mu\text{m}$ .

## 3.2 Neutron detection system

Direct spatially localized detection of neutrons is difficult. Therefore, a neutron imaging system uses a corporate neutron-photon converter, placed between the transmitted neutron beam and the detection system within the converter; neutrons interact with the nuclei of the converter material, releasing secondary radiation. It is the secondary radiation that is detected by the electronic sensor or film. A commonly used two-dimensional integrating detector for neutrons is based on an electron-optical configuration. In our experiments, an  $^6\text{LiF-ZnS}$  scintillator screen is used (Nuclear

Enterprises NE-426). The mechanical components are shown in Figure 3.4. Here the  ${}^6\text{LiF}$  stops neutrons and  $\text{ZnS}$  stops the  $\alpha$  particles.

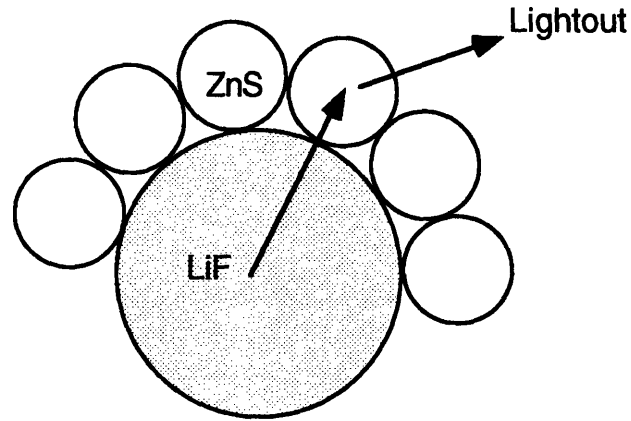


Figure 3.4: The mechanical composition of scintillation screen.

In our experiment the scintillation screen has an overall dimension of 180 X 240 (mm). This scintillation screen consists of one part of  ${}^6\text{LiF}$  and four parts of  $\text{ZnS}$  in weight with some kind of binding material. The thermal neutron is stopped by reaction



with 4.78 MeV energy released. In order to stop more thermal neutrons, it is needed to either increase the component of  ${}^6\text{LiF}$  or to thicken the scintillation screen; but the former does not increase the output light, and the later increases light output only mildly with sacrificing spatial resolution. By considering both light output (i.e. the efficiency) and resolution, we selected NE-426. The thickness of this scintillator screen is 0.25 mm. It has a detection efficiency of 15% for thermal neutrons incident perpendicular to the screen and a light output of  $1.7 \times 10^5$  photons per neutron [31]. The light emitted from  $\text{ZnS}$  is blue-green (around 400 nm). In our experiment, the  $\text{ZnS}$  scintillator has been

modified to our specifications using a Cu activator rather than the standard Ag activator [32]. This shifts the spectrum of the emitted light further toward the green region where the quantum efficiency of the CCD is higher. The inherent detection efficiency of the screen can be increased at the expense of reduced spatial resolution in one dimension by tilting the screen at an angle,  $\alpha$ , to the incident neutron flux. Alternatively, the amount of Li can be increased but will result in lower light output. (We could tilt it in the direction so as to degrade the spatial resolution in the slice thickness direction). The screen has a resolution of 100  $\mu\text{m}$  when used in its intended configuration, and this can be preserved through the lens-CCD system. A mirror reflects the visible light out of the direction of the neutron beam in order to prevent radiation damage to the optical components and to ease the shielding of the CCD camera. A CCD camera is used to record the focused output light image and transfer the data into a computer. We have to use a high resolution CCD chip in order to maintain high resolution in the whole system. The CCD camera we used in our experiment is a Princeton Instrument TE/CCD-1242E which uses an EEV 05-30 CCD array of 1152 x 1242 pixels (26x28 mm) with pixel dimensions of 22.5 x 22.5  $\mu\text{m}$ .

### **3.3 Object handling system: Turn table and translator**

In order to get the tomographic image, we have to use a turntable and a translator so that we can let the object be rotated and translated. In our experiment we used an RT-12-SM (New England Affiliated Technologies) rotary table. The motor driven rotary table provides a highly accurate angular position throughout a 360 degree range. The diameter of this turntable is 12 inches, its minimum accuracy is 3' (minutes). Horizontal and vertical load bearing capacities are 200 lbs and 45 lbs respectively. This table is supplied completely with locking connectors for motor and limit/encoder signals, a 50 oz-in stepping motor with a rear mounted knob for fine manual control. We also use an HM-

2400-SM translator so that we can move the object back and forth. It offers a higher load capacity and torsional stiffness. Its capacity is 2200 lbs and can travel 24 inches. The HM-2400-SM is supplied completely with built-in precision limit switches, integral, strain relieved motor and limit connectors; and a 100 oz-in stepping motor with manual adjustment knob. Figure 3.5 shows the turntable and translator. We have mounted the turntable on top of the translator. We can see that for this object handling system, we can turn an object of up to 200 lbs and translate an object of 2200 lbs. The total weight of this system is 108 lbs so it can be transported very easily.

The next step is to program the computer to control the turn table and translator assembly. Figure 3.6 shows how the computer controls the motion system.

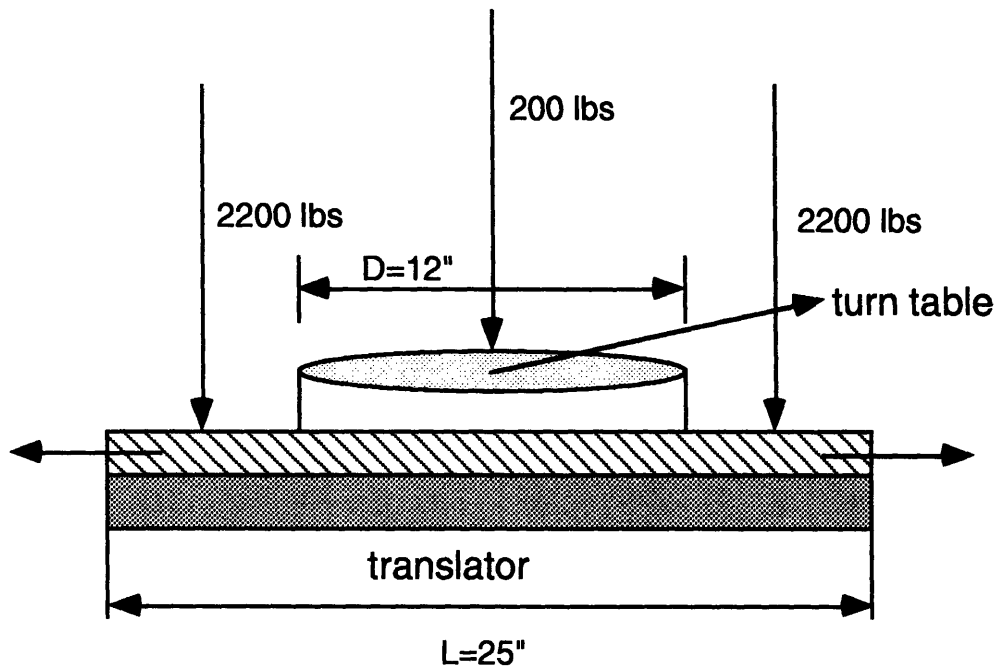


Figure 3.5: Turn table and translator.

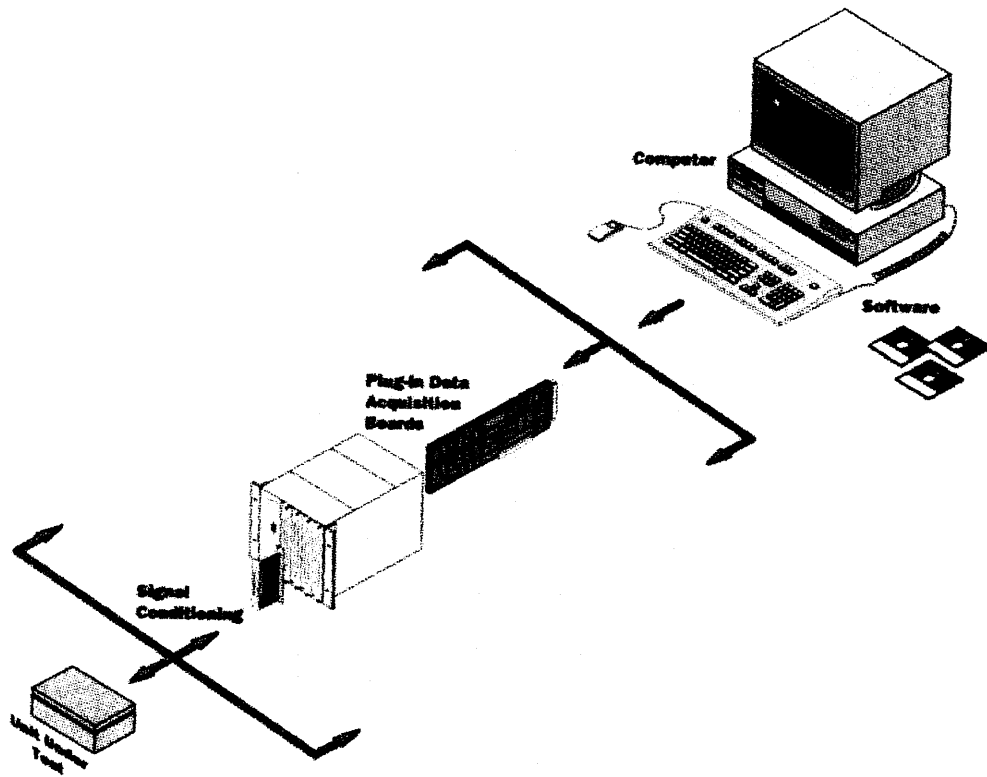


Figure 3.6: The computer control system.

The nuDrive 3-axis system is a complete power amplifier and system interface unit for use with one, two or three axes of simultaneous or independent servo or stepper motion control. In our system we use the stepper motor. It is ideally suited to our experimental system. The nuDrive provides everything needed to interface motors, encoder limit switches and other motion hardware to computer based motion control boards. nuDrive can drive a broad range of stepper motors. The necessary power suppliers are built in and use standard 115 VAC for operation. All electronics are fan

cooled and protected from overheating and over current to assure reliable operation. The nuDrive is connected to a motion control board, nuStep, via a 50 pin ribbon cable.

The nuStep is a 3 Axis Stepper Motor Control board providing high-performance motion control for NuBus based Macintosh computer systems. It provides programmable motion control for three axes of operation. The nuStep board also has functions including a programmable limit switch and home switch inputs as well as programmable I/O bits for additional system configuration and control.

Figure 3.7 shows a Labview motion control program which I have developed for our experiments. It is important to put the change direction control on the program because for the translator, the maximum travel distance is 24 inches. After it travels forward 24 inches, we have to change the direction to let it travel back.

### **3.4 Optical system**

We readout images from the CCD-chip by using a computer controlled interface. In order to get a good image we have to put a focused image onto the CCD chip. An optical lens is mounted to the front of the CCD-camera. The function of this lens is to gather the light emitted from the scintillator screen onto the front surface of the CCD-chip. The characteristics of the lens strongly influences the detection efficiency of the experimental system since a large amount of light is lost due to the minification of the large scintillator screen (object) onto the CCD-chip (image).

For a single lens there are two characteristic parameters for describing the optical property of the lens: focal length, and F number, the ratio of the focal length to the lens diameter. A lens with a large diameter has a better light-gathering ability and a smaller F-number. In our experiments, we have built up two optical systems. One lens is Nikon

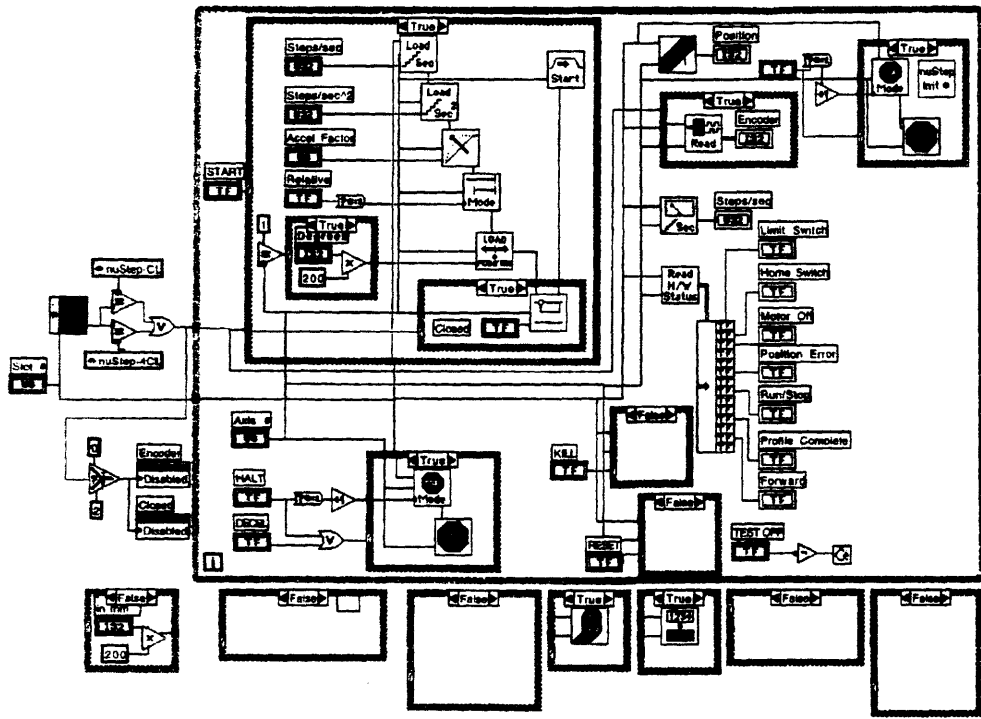
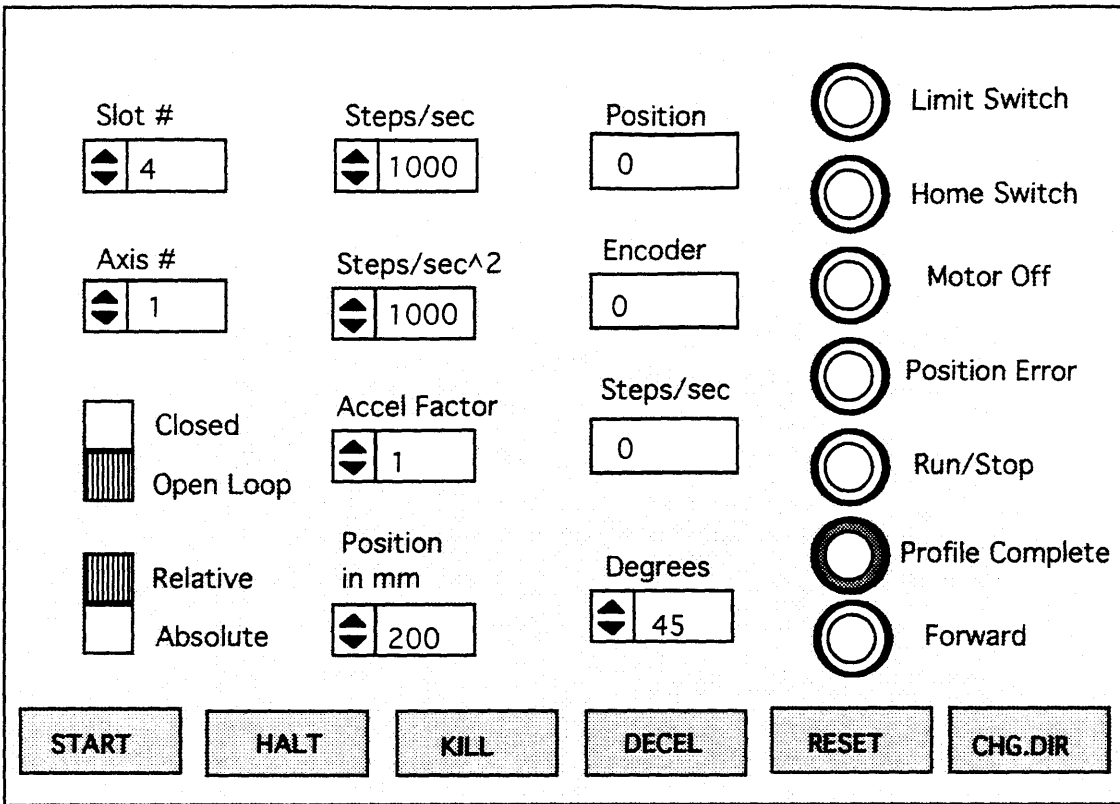


Figure 3.7: The Labview software for motion control. Top: the front control panel; Bottom: the diagram panel for the motion control.

with focal length 50 mm and F number 1.2. Another lens is Perkin-Elmer with a focal length of 100 mm and an F number of 0.95. For these two optical systems, the effective minification ratios are 18 and 7 respectively, with corresponding fields of view 390 x 420 mm and 182 x 196 mm.

For a single lens optical image system, we have the following equation

$$\frac{1}{S_0} + \frac{1}{S_i} = \frac{1}{f} \quad (3.7)$$

here  $S_0$  is the distance from object to lens,  $S_i$  is the distance from image to lens and  $f$  is the focal length of the lens.

The minification,  $m$ , is defined as the ratio of the object height to the image height:

$$m = \frac{H_0}{H_i} = \frac{S_0}{S_i} \quad (3.8)$$

here  $H_0$  is the height of the object,  $H_i$  is the height of the image. By putting equation (3.8) into equation (3.7) we can get

$$S_0 = (1 + m)f \quad (3.9)$$

In our experiment we have to consider the light loss in the optical system due to the dimension of the lens, because some of the light can not be captured by the lens. This is given by the factor  $L$ , which expresses the fraction of light captured from the screen to the lens. As shown in the Figure 3.8, the efficiency is determined by the fractional solid angle subtended by the lens:

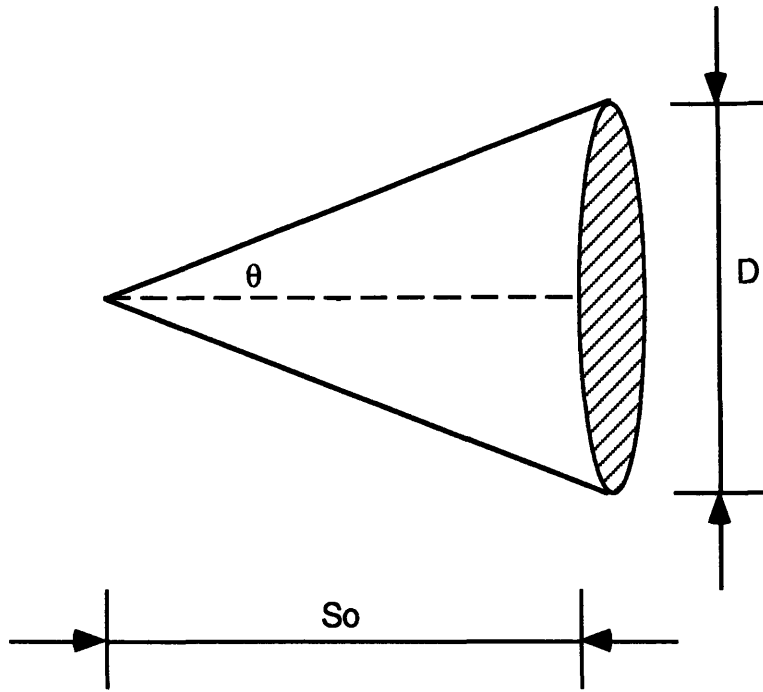


Figure 3.8: The light loss due to the finite lens.

$$\epsilon = \frac{d\Omega}{4\pi} = \frac{2\pi d(\cos\theta)}{4\pi} \quad (3.10)$$

If we further assume a Lambertian source of light where the apparent brightness :

$$B \propto \cos\theta \quad (3.11)$$

We can integrate over the subtended angle to obtain independent of lens diameter:

$$L = \frac{1}{[2F(1+m)]^2} \quad (3.12)$$

To reduce the amount of light loss we have to use a smaller F number lens and also decrease the minification number  $m$ , which favors a larger CCD-chip. In our experiment for the two optical systems, the L numbers are  $5.0 \times 10^{-4}$  for the Nikon lens and  $4.0 \times 10^{-3}$  for the Perkin-Elmer lens.

### **3.5 CCD camera system**

In its broadest definition, a charge-coupled device (CCD) image sensor is an analog integrated circuit that converts an optical image into an electronic output, i.e., it is the electro-optic interface in an electronic image pickup system. Therefore, CCD cameras are generally used to transfer an analog photon image into a digitized data file. A digitized image has many of advantages over an analog image, since we can do more image processing on the digitized image, such as add two images together, subtract them, or filter them. In recent years, CCD imaging systems have begun to find widespread applications in different fields [33, 34, 35].

The CCD camera used in our experiments is a Princeton Instrument TE/CCD-1242E which uses an EEV 05-30 CCD array of 1152 x 1242 pixels (26 x 28 mm) with pixel dimensions of 22.5 x 22.5  $\mu\text{m}$ . The camera is interfaced to a Princeton Instruments ST-138 controller which can be read out in either high speed mode (12 bits, 1 MHz) or low speed (15 bits, 430 kHz) mode. The ST-138 also controls the thermoelectric cooler on the CCD and has a lower limit of  $-60^\circ\text{C}$  with air cooling and, if further dark current reduction is required,  $-70^\circ\text{C}$  with supplemental water cooling.

Now we want to know the limits on neutron flux set by CCD dark current. This is a very important parameter to know for the whole experiment system. We have to let the

signal large than the noise so we can get the image which we want. Assuming the following:

$\Phi_n$	detected neutrons/cm <sup>2</sup> -sec at screen
$n_e$	photoelectrons/neutron produced in CCD
$\eta_{ccd}$	quantum efficiency of CCD
$\eta_o$	optical efficiency of lens (transmission)
$\eta_\gamma$	photons/neutron produced in screen
$F$	f/number of lens
$m$	minification ratio ( $A_{obj}/A_{ccd} = m^2$ )
$n_{dc}$	CCD dark current in electrons/cm <sup>2</sup> -sec

Using these definitions, we see the electron flux (e/cm<sup>2</sup>-sec) produced at the CCD is given by:

$$\phi = \Phi_n^2 n_e m^2 \quad (3.13)$$

The factor of  $m^2$  comes from the decrease in area due to minification. The factor of  $n_e$  computed for a Lambertian source is:

$$n_e = \frac{\eta_{CCD} \eta_o \eta_\gamma}{[2 F (m + 1)]^2} \quad (3.14)$$

and thus:

$$\phi = \frac{\Phi_n \eta_{CCD} \eta_o \eta_\gamma}{4 F^2} \frac{m^2}{(m + 1)^2} \quad (3.15)$$

which for large m gives:

$$\phi = \frac{\Phi_n \eta_{CCD} \eta_0 \eta_\gamma}{4 F^2} \quad (3.16)$$

which is independent of CCD size. This allows us to compare CCDs easily since the dark current in CCDs scales as the area, i.e., is just given in e/cm<sup>2</sup>-sec and thus can be compared to the neutron fluence.

If we set a lower limit of neutron fluence as that where the neutron signal is just equal to the dark current, then:

$$n_{dc} = \frac{\Phi_n \eta_{CCD} \eta_0 \eta_\gamma}{4 F^2} \quad (3.17)$$

and finally:

$$\Phi_n = \frac{4 F^2 n_{dc}}{\eta_{CCD} \eta_0 \eta_\gamma} \quad (3.18)$$

In our experimental we have:

$$\eta_{ccd} = 0.30$$

$$\eta_0 = 0.85$$

$$n_\gamma = 8 \times 10^4 \text{ photons/neutron}$$

$$F = 0.95$$

which gives:

$$\Phi_n = 18.2 \times 10^{-4} n_{dc} \quad (3.19)$$

For our CCD camera system, dark current is quoted at less than 1 e/pixel/sec for a 22.5  $\mu\text{m}$  x 22.5  $\mu\text{m}$  pixels in a 1252 x 1142 array, or approximately:

$$n_{dc} = 2 \times 10^5 \quad [e / \text{cm}^2\text{-sec}] \quad (3-20)$$

which gives a lower limit for  $\Phi_n$  of 30 n/cm<sup>2</sup>-sec and thus indicates that dark current is only a factor at extremely low fluences. The dark current will add a very small amount of noise in quadrature and can essentially be neglected for any realistic flux. That is why in section 3.1 we only considered the statistical error and neglected the dark noise.

## 3.6 Summary

The whole imaging system was described completely in this chapter. Figure 3.9 shows the imaging system we have constructed.

The size of the light tight chamber is 90 cm x 30 cm x 30 cm. It is made of aluminum, which, since it has lower neutron activation, is easy to move around without necessitating additional shielding or radiation protection. The scintillation screen is Nuclear Enterprises NE-426 with an overall dimension of 180 x 240 mm. The scintillator is viewed through a front surfaced mirror by the CCD camera with a choice of two lenses: the first is a Nikon 50 mm F/1.2 lens and the second a Perkin-Elmer 100 mm F/0.95 lens. The CCD camera is a Princeton Instrument TE/CCD-1242E which uses an EEV 05-30 CCD array of 1152 x 1242 pixels (26x28 mm) with pixel dimensions of 22.5 x 22.5  $\mu\text{m}$ . For a fixed lens - scintillator distance of approximately 80 cm in our current system, the effective minification ratios are 18 and 7 respectively, with corresponding fields of view of 390 x 420 mm and 182 x 196 mm.

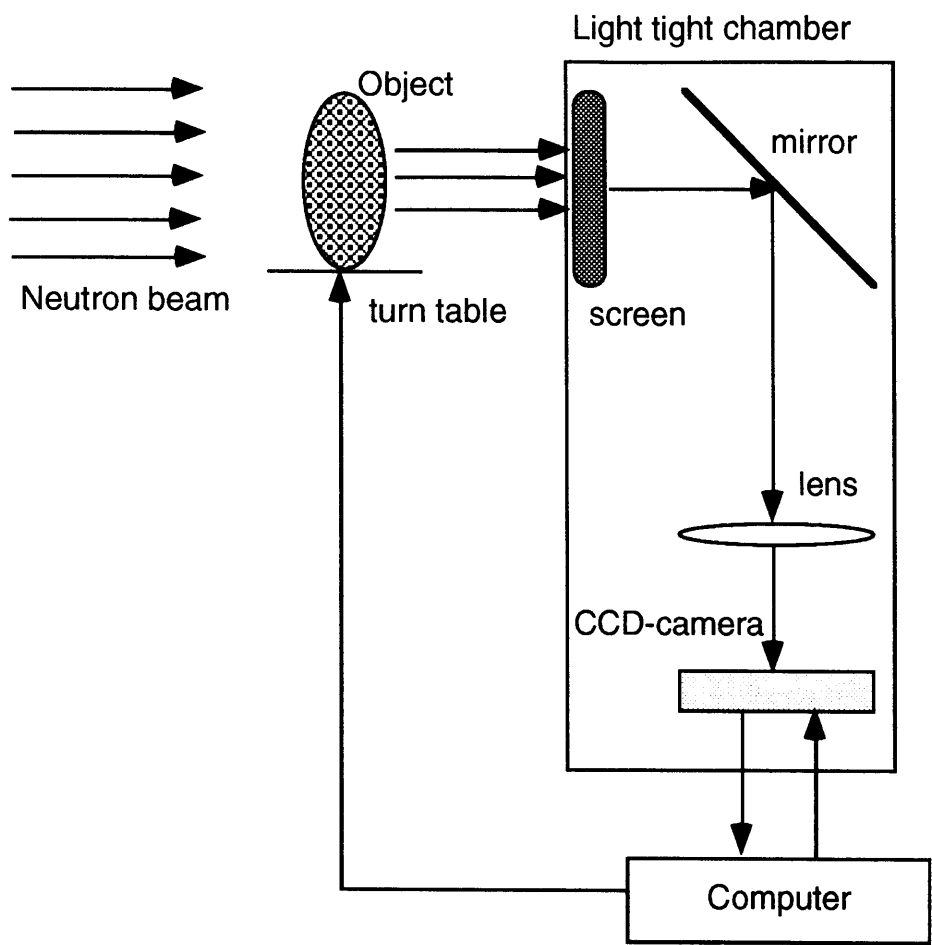


Figure 3.9: Schematic view of camera system.

# **Chapter 4**

## **Accelerator neutron sources**

In this chapter we will provide a general review of the development of accelerator neutron sources and discuss various means of particle acceleration. We will also talk about our AccSys Technology model DL-1 RFQ accelerator, the key piece of equipment for our portable neutron imaging system.

### **4.1 Particle accelerator system**

Neutrons have proved to be powerful tools for nondestructive testing and evaluation for science and engineering. In order to get a high quality image, it is important to have a very good neutron source; we require that the neutron source have high flux, high uniformity and be well collimated. As we mentioned earlier, in reality, it is impossible to use a reactor neutron source to do corrosion tests for aircraft fuselage and wings in the field. We have to develop a small accelerator based and portable neutron imaging system to do the field tests.

Here we will mainly discuss the accelerator source, since in our experiment we are going to use this type of neutron source. In order to get an accelerator based neutron source, first we have to have charged particles. Second we need to accelerate these

particles. In the last step we use those high energy charged particles to bombard a target element which produces neutrons through a nuclear reaction. While the principles may seem simple, actually, we have to face many technical problems, such as how to get charged particles, how to accelerate them, what is the maximum energy we can achieve and what kind of target materials should we use. First we will discuss the various means of particle acceleration.

Particle accelerators are among the most useful tools for research in nuclear physics and high-energy particle physics. In 1927, physicist E. Rutherford first proposed that new nuclear transformations could be accomplished by bombarding the nuclei of various substances with hydrogen ions (protons) accelerated to high velocities using a direct-current generator [36]. In 1928, Wideroe used a linear accelerator to accelerate potassium and sodium ions. In 1932, the first charged particle accelerator, developed by Cockcroft and Walton, was used to investigate Rutherford's hypothesis. Figure 4.1 shows the equipment referred to as the "proton gun", which they used for the experiment. Hydrogen atoms were ionized by electrons moving through hydrogen gas and accelerated to an energy of 150 keV by a constant applied potential; a lithium target was placed in the path of the output proton beam. They observed the emitted particles and hypothesized the nuclear reaction as:



This was the first experiment producing a nuclear transformation using charged particles instead of a radioisotope source.

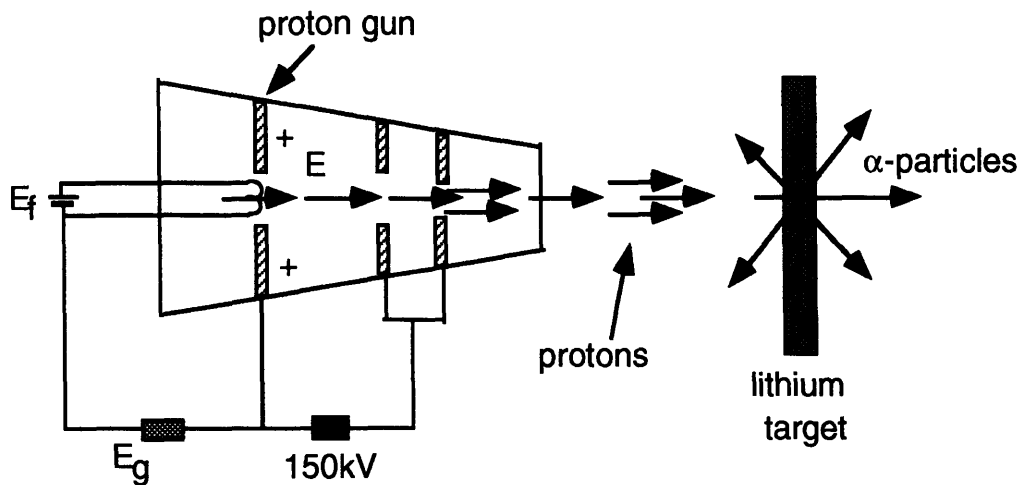


Figure 4.1: Schematic of Cockcroft and Walton's experiment with the first particle accelerator [36].

With the development of new techniques, several different types of accelerators now exist, each differing in the way used to accelerate the charged particles and the maximum energy the charged particles can reach. Some accelerators accelerate charged particles by applying a static voltage potential, some based on dynamic electromagnetic (EM) fields.

## 4.2 Electrostatic accelerator

The simplest accelerator is the electrostatic accelerator [37]. In the electrostatic accelerator, also known as a direct-current (DC) accelerator, a potential difference between two electrodes is used to accelerate charged particles. The general design for the electrostatic accelerator has both sides of an evacuated linear accelerating chamber connected to a high-voltage generator. A large voltage potential difference between the charged particle source and the opposite end of the chamber accelerates the ions, as

shown in Figure 4.2. The maximum energy the charged particles can reach is determined by the potential difference of the chamber. More complex designs contain many electrodes throughout the acceleration chamber, making the voltage gradient more uniform. The basic difference among these DC accelerators is their method of generating a high voltage potential.

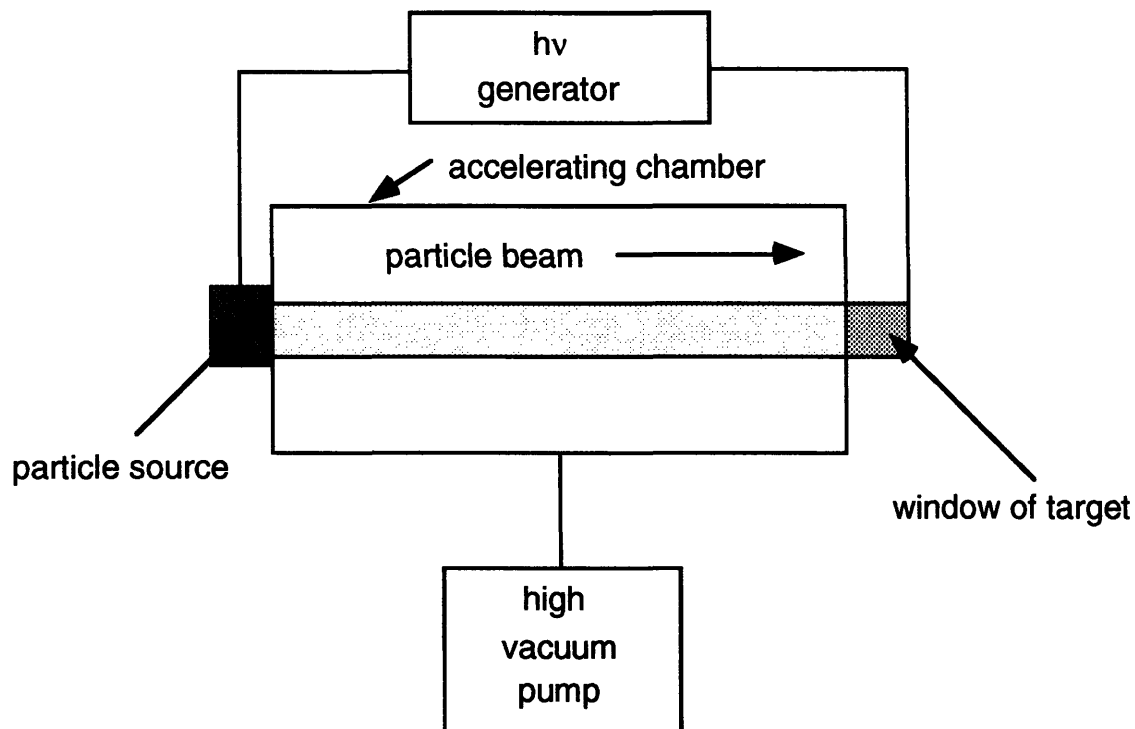


Figure 4.2: Schematic of a linear DC accelerator [36].

The disadvantage of DC accelerators is that the accelerating chamber holds the entire accelerating voltage. Thus, the insulating requirements for these chambers are the major limitation on the maximum voltage which can be applied, although they can still achieve potential as high as 30 MV. This limits particles with a unit charge energies of 30 MeV. This limitation can be overcome by accelerators using radiofrequency

electromagnetic fields or cyclic accelerator. We will discuss two accelerators which have been used for production of neutrons, the linear accelerator and the cyclotron.

### **4.3 Linear radiofrequency accelerators**

Linear radiofrequency accelerators accelerate charged particles in a straight line through a chamber containing a number of electromagnetic field segments (see Figure 4.3). These field segments are produced by electrodes and are separated by field gaps.  $L_n$  is the distance the particle travels at constant velocity before being accelerated again. Within the field segments a radiofrequency voltage is applied such that the particle is accelerated; the particle then drifts through a field gap  $L_n$  (at constant velocity) to the next field segment where it is again accelerated. Specific conditions are required to ensure that the particles are exposed to only accelerating rf fields. During the half period when the fields reverse sign, the particles must be shielded from the fields so that they will not be decelerated again. The length of the field gaps correspond to the oscillating electromagnetic field such that the particle only feels the accelerating electrical force of the bipolar electromagnetic field, i.e., the field gap length  $L_n$  increases with each acceleration to match the increased velocity of the particle, resulting in the particle reaching the next EM field just as the polarity of the field changes to create an accelerating force on the particle [38].

The disadvantage of linear RF accelerators is the need for long acceleration chambers to reach high energies and the need for additional magnetic fields to focus the beam. The electron linear RF accelerator built at Stanford uses a chamber of 3200 m to reach energies of 22 GeV.

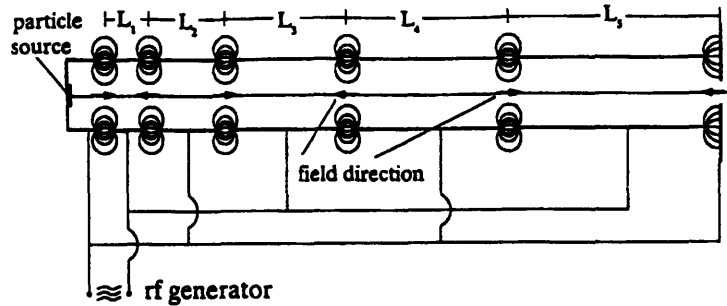


Figure 4.3: Schematic of a linear RF accelerator.

## 4.4 Circular radiofrequency accelerators

In order to decrease the length of the accelerator chamber, scientists developed the circular radiofrequency accelerator. Circular accelerators use magnetic fields to guide charged particles around a closed orbital trajectory. The acceleration is generally conducted in a circular cavity in which particles move in circular or gradually expanding orbits. Particles orbiting within the cavity periodically gain energy from an RF EM field. This configuration simplifies the RF system compared to linear RF accelerators, allowing protons and heavier ions to be accelerated to extremely high energy; the Fermi National Accelerator Lab (FNAL) accelerates protons up to 1000 GeV[39]. The function of the magnetic field is only to guide the particles around a circular orbit. The RF field oscillations must be synchronized with the particle motion to achieve acceleration: the time for a particle to travel around one orbit must be an integer multiple of the RF field oscillation period. This synchronization depends on the particle velocity, path length, magnetic field strength and frequency of EM field.

Circular RF accelerators, especially cyclotrons have the potential to provide practical application with intense non-reactor neutron sources.

## 4.5 Cyclotron accelerators

Cyclotrons use a uniform magnetic field and RF cavity extending over the entire aperture of the magnet, see Figure 4.4. The accelerating cavity is cut in two halves with the accelerating fields generated between the sections and the poles of the magnet. Thus, most of the particle's orbital path is without a tangential accelerating force. Cyclotrons accelerate particles in a nearly circular path that spirals outward. The ion path is curved using magnetic fields perpendicular to the particle's trajectory. As the particles gain energy, their radius of curvature increases, since the magnetic field is constant, and they spiral outward. The beam is extracted using magnetic fields to divert the particles from their near orbital path into a beam tube.

The particles pass through the acceleration force twice per revolution. The revolution time,  $\tau$ , in a cyclotron is given by:

$$\tau = \frac{2 \pi r}{V} = \frac{2 \pi m c}{e} \frac{\gamma}{Z B} \quad (4.1)$$

where  $\gamma$  can be set to one for non relativistic particles,  $Z$  is the charge of the particle,  $e$  is the electron charge,  $B$  is the magnetic field,  $r$  is the radius of orbit,  $m$  is particle mass, and  $V$  is the velocity of the particle. If the magnetic field is constant the particles have constant revolution frequency, which then defines the appropriate EM frequency:

$$f_{rev} = f_{RF} = \frac{Z e B}{2 \pi m c} = const \quad (4.2)$$

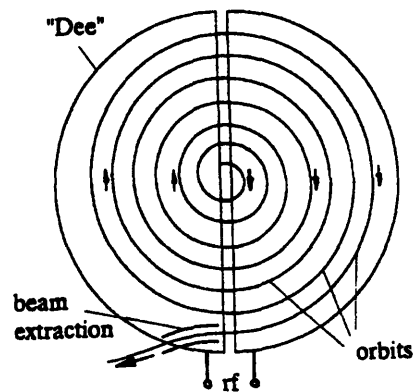
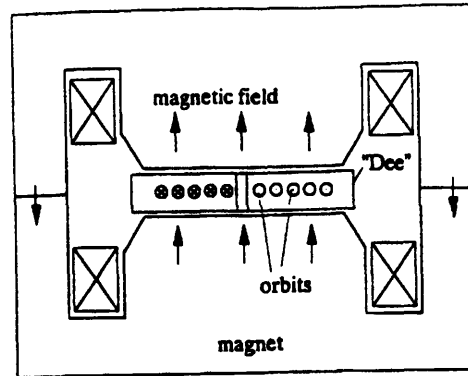


Figure 4.4: Schematic of a cyclotron accelerator.

The above equation shows the EM frequency is dependent on charge  $Z$ , and magnetic field strength,  $B$ , resulting in the following relations for protons, deuterons, and  $\alpha$ -particles:

$$f_{\text{RF}}(\text{MHz}) = 1.53 B (\text{kG}) \quad (\text{protons})$$

$$f_{\text{RF}}(\text{MHz}) = 0.76 B (\text{kG}) \quad (\text{deuterons})$$

$$f_{\text{RF}}(\text{MHz}) = 0.76 B (\text{kG}) \quad (\alpha\text{-particles})$$

The maximum energy a particle can acquire in a cyclotron is a function of the particle mass, charge, magnetic field, and maximum orbital radius,  $R$ :

$$E_{max} = \frac{1}{2} m v^2 = \frac{(c p)^2}{2 m c^2} = \frac{(Z e B R)^2}{2 m c^2} \quad (4.3)$$

where  $p$  is momentum. Thus, for protons, deuterons, and  $\alpha$ -particles we have the following relations for  $E_{max}$ :

$$E_{max}({}^1H) = 0.48 B^2 (k G^2) R^2 (m^2)$$

$$E_{max}({}^2H) = 0.24 B^2 (k G^2) R^2 (m^2)$$

$$E_{max}(\alpha) = 0.48 B^2 (k G^2) R^2 (m^2)$$

Although cyclotrons are relatively compact, the need for strong magnetic fields excludes their use for applications needing a maneuverable neutron source. However, as stationary neutron sources, cyclotrons may be the best alternative to nuclear reactors.

## 4.6 Linear radiofrequency quadrupole accelerators

Finally we will discuss Linear Radiofrequency Quadrupole Accelerators in more detail, because this is the type of accelerator used to do our experiments.

RFQ accelerators were first proposed by Kapchinskii and Teplyakov in 1970 [40]. The RFQ is a linear accelerator structure for low velocity ions which focus and accelerate with the help of electrical radiofrequency (RF) quadrupole fields. The major advantage for this kind of accelerator is that it uses radiofrequency electromagnetic fields to simultaneously focus, bunch, and accelerate the ion beam, therefore, it has strong ability to focus and bunch an ion beam at low energies. These accelerators can capture

almost all ions extracted from the ion source at low voltage and accelerate them to an energy of 1-2 MeV in very short distance, generally a few meters or less than a meter.

The basic structure of an RFQ consists of four electrodes arranged symmetrically around the beam axis and excited such that adjacent electrodes have the same voltage amplitude but with  $180^\circ$  phase shift. This corresponds to an array of quadrupole singlets and is a pure focusing channel as first proposed by Paul [41] without accelerating field components.

RFQ accelerators focus the ion beam by using electromagnetic quadrupole fields uniformly distributed along the length of the beam channel. Figure 4.5 shows the schemes of static, rf, and RFQ quadrupoles. First let us consider how the system focuses an ion beam. Particles with off axis trajectories will experience a focusing force in one plane and defocusing force in the other on alternate RF half cycles, switching the focusing-defocusing planes with each half cycle. This results in a strong focusing system that will transport an ion beam without acceleration.

Now we need to consider how the system accelerates the ion beam. The ion beam is accelerated by the mechanical perturbation of the four line electromagnetic focuser. If the separation of electrodes of similar polarity varies periodically along the beam channel (see Figure 4.5), a longitudinal accelerating field,  $E_z$ , results. The mechanical modulation of the electrodes as indicated in Figure 4.5 and 4.6 now introduces an axial accelerating field  $E_z$ . The charged particles can be accelerated by this longitudinal accelerating field,  $E_z$ . For a given electrode voltage  $U$ , the amplitude  $A$  of the accelerating field will be proportional to the modulation  $m$  of the electrodes while the focusing strength, which is proportional to the radial field  $E_r$ , will decrease with increasing modulation.

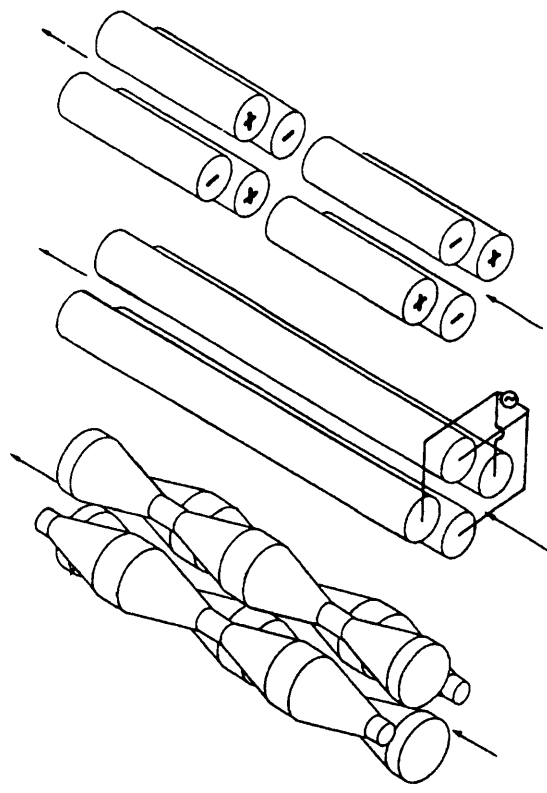


Figure 4.5: Schemes of static, RF, and RFQ quadrupoles (from top to the bottom).

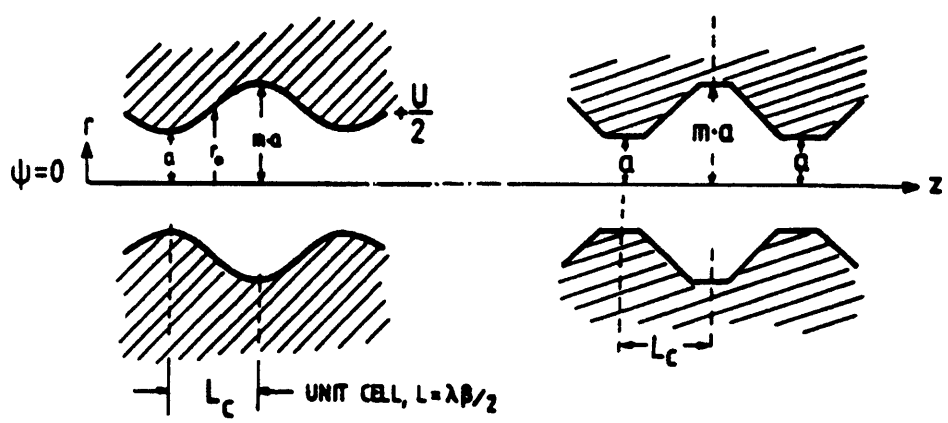


Figure 4.6: Modulated RFQ electrodes.

Assuming  $E_z = 0$ , if we only consider pure rf-quadrupole focusing channel fields, we have:

$$E_r = E_\psi = \frac{U}{a^2} r \cos(2\psi) e^{i\omega t} \quad (4.4)$$

Adding a lowest order accelerating field with  $E_z$  not equal to zero, we have:

$$E_z = A I_0(kr) \sin(kz) e^{i\omega t} \quad (4.5)$$

where  $A = k BU/2$ ,  $k = \omega/v = \beta 2\pi/\lambda_0$ . Also we have:

$$E_r = \left\{ X \frac{U}{a^2} r \cos(2\psi) - I_1(kr) \cos(kz) \right\} e^{i\omega t} \quad (4.6)$$

with the abbreviation

$$B = \frac{m^2 - 1}{m I_0(ka) + I_0(ka)} \quad (4.7)$$

where  $X = 1 - B I_0(ka)$ ,  $v$  is the particle velocity,  $\beta = v/c$ , RF frequency  $\omega$ , and aperture is  $a$ .

The RFQ resonator for our AccSys Technology model DL-1 was designed in this way so that at any given time the voltage on adjacent pole tips is the same in magnitude but opposite in sign; after each half cycle these voltages reverse sign, thus producing a net quadrupole focusing force in the plane transverse to particle acceleration. The focusing force is spatially contiguous along the direction of acceleration. If the pole tips have a constant radius, only a radial focusing force will be present and no acceleration

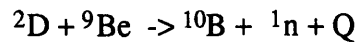
will take place; however, if the pole-tip distance is modulated periodically, a longitudinal accelerating field is produced in addition to the transverse focusing field.

The focusing accelerating quadrupole fields allow RFQ to capture and bunch a high percentage of the ions from the pre-accelerator ion source, resulting in small ion losses and high transmission efficiencies. The ions can be accelerated to high energies over short distance, and the RF amplitude of an RFQ accelerator is the only physical parameter to adjust during operation; thus, RFQs are smaller and relatively simple to operate compared to conventional linear accelerators, although conventional linacs may be used to go to higher energies.

#### **4.6.1 Technical description for AccSys technology DL-1 RFQ accelerator**

The unconventional aspect of the work on neutron radiography and tomography done for this thesis is the use of an accelerator neutron source instead of a reactor source. As we mentioned in Chapter 2, when Kallman and Kuhn took the first radiograph in Berlin they used a small accelerator approximately equivalent to a 2 to 3 gram Ra-Be source. After the nuclear reactor was well developed, which provided a high neutron flux, scientists started to use nuclear reactors as a neutron source. As we know that in the real world, it is important to develop a portable neutron tomographic imaging system, since we can not carry a reactor from place to place and at the same time, it is hard to fly an airplane to a reactor to do the corrosion test. We have to achieve two goals in this thesis: one is to develop a portable system; the other is to make the accelerator produce a certain amount of neutron flux so that we can have enough neutrons to detect corrosion. An AccSys Technology model DL-1 RFQ accelerator has been obtained for use in our experiment. The machine is a compact radiofrequency quadrupole (RFQ) linear accelerator (linac) that accelerates deuterium ions to an energy of 900 keV and bombards a beryllium target

to produce neutrons. Neutrons with typical energies of 5 MeV are produced through the reaction:



The pertinent operating parameters for the Model DL-1 are listed in Table 4.1.

Table 4.1: Model DL-1 system specifications

Accelerated particle	d+
Input Beam energy (nominal, MeV)	0.2
Output Beam energy (nominal, MeV)	0.9
Neutron yield (n/sec/mA)	$7.8 \times 10^7$
Beam current/pulse (mA)	10
Beam pulse width (msec)	30-120
Pulse repetition rate (Hz)	1-640
Maximum target current (mA)	140
Maximum target yield (n/sec/4p)	$1 \times 10^{10}$
Thermal flux (n/cm <sup>2</sup> -sec)	$5.0 \times 10^7$
Collimated flux at L/D=24 (n/cm <sup>2</sup> -sec)	$5.4 \times 10^3$
Accelerator length (ft)	4
Accelerator weight (lbs)	400
Electrical requirement (kVA)	12
Pulsed RF power (kW)	40
RF duty factor (maximum)	2.25%

The machine consists of three major components: the RFQ accelerator with ion source, the RF power amplifiers, and the ion source power supply and control system.

The accelerator is connected to the amplifiers and control systems through flexible RF and high voltage cables. Figure 4.7 shows the AccSys Technology DL-1 RFQ accelerator.

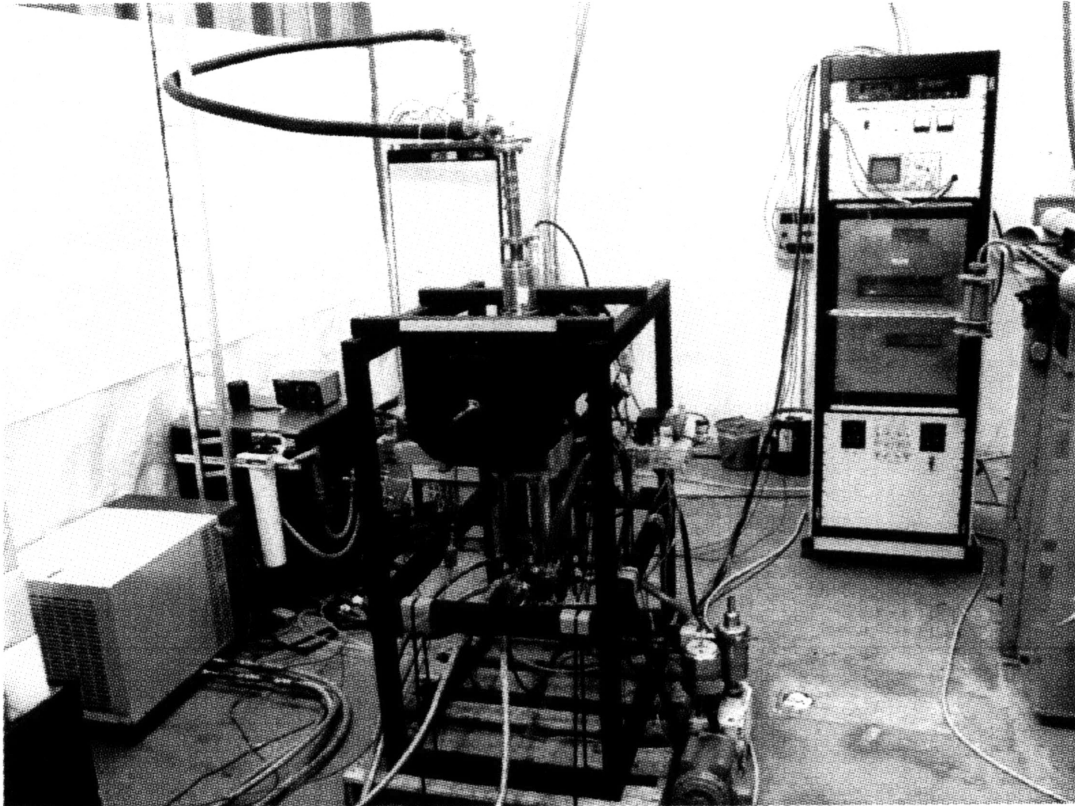


Figure 4.7: AccSys Technology DL-1 RFQ accelerator. The RFQ is in center with RF amplifier cabinet on left rear and ion source power supply and controls on right.

The Model DL-1 Linac Neutron Generator produces a positive ion beam by the ionization of deuterium gas in a duoplasmatron ion source. The ion source and the power supplies required to operate it are isolated at a voltage of 25 kV. This voltage results in an ion beam being extracted from the plasma in the ion source anode and accelerated across

the high voltage gap through the grounded extraction electrode. The extracted deuterium ion beam (80 to 90%  $d^+$ , 10-20%  $d_2^+$  ions) exits from the accelerating gap through an aperture in the extraction electrode and is measured in a beam current toroid before being focused into the RFQ linac by an electrostatic einzel lens.

The RFQ linac used in the Model DL-1 Neutron Generator is a compact four-vane resonant cavity accelerator operating at 425 MHz that accelerates the  $d^+$  ions from 25 keV to 900 keV with an acceptance of the dc beam current injected into it of about 90%. This structure has been designed and built to be rugged, yet precisely aligned in order to achieve and maintain good performance. The RFQ resonator structure insures that no adjustment of the internal vane positions will be required during the lifetime of the linac and the mounting mechanism of the RFQ inside its vacuum enclosure maintains the concentricity of the beam axis to the vacuum chamber. This alignment stability insures that the accelerated deuterium beam always hits the beryllium target. The characteristics of the RFQ linac, an RF driven accelerating device, are such that only  $d^+$  ions are accelerated and the beam energy remains constant if the RF power is above a threshold value.

A cross-sectional view of the Model DL-1 RFQ linac is shown in Figure 4.8, with the active components labeled. This drawing indicates that the ion injector is placed in a separate vacuum chamber from the RFQ and is pumped by a separate vacuum pump. The alignment of the ion source and einzel lens within the ion injector are maintained by the assembly of its precision parts, while two alignment pins are used to maintain the alignment of the injector with respect to the RFQ. The RFQ linac is housed in a vacuum chamber that has two parts. One end of the vacuum chamber has the RFQ mounted onto it, along with the cooling lines and electrical input and signal feedthroughs. This feedthrough collar then bolts to the main part of the vacuum chamber, which has the vacuum pump mounted to it. The RF drive loop is mounted into the RFQ resonator with

the vacuum chamber in place, and then sealed to the vacuum chamber using a flexible bellows assembly to allow for motion between the RFQ and its vacuum chamber during vacuum pump-down and also during operation of the RFQ.

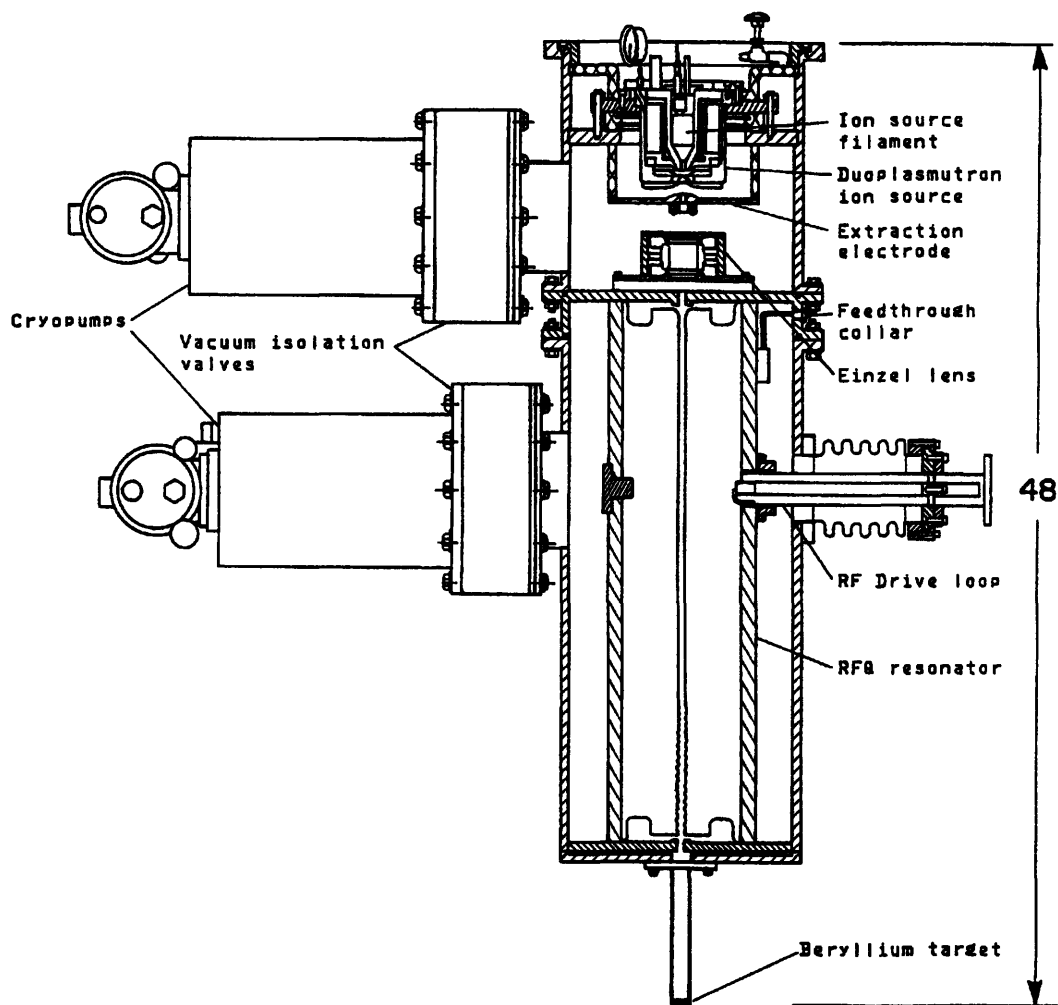


Figure 4.8: Detailed cross-section view of the AccSys Technology DL-1 RFQ accelerator.

The RFQ linac is driven from a stand-alone RF power system. The vacuum is maintained by commercial cryopumps attached to the linac and the ion injector. The cryopumps are kept at a constant operating temperature, we set to 12 °K in our

experiments, during operation using a closed-cycle water cooling system that also cools the ion injector and RF power amplifier. In this prototype unit, the PC-based control system operates the ion injector system and the vacuum pumping system, and provides the timing pulse for the RF power system. However, the RF power amplifier and water cooling system are each operated from separate manual controls.

#### **4.6.2 Control system**

An interlock system was installed in the lab area; the switch was connected to the RF power supply directly. For safety reasons, if someone accidentally opens the door of the lab during operation, the RF power supply will stop automatically. The AccSys Technology DL-1 RFQ linac control system consists of a 486 PC controlling two interface chassis located in the injector electronics cabinet over a MIL-STD-1553B data bus. It was designed to be low cost, reliable and easy to use. All interlocks are hardwired with no software dependence, making the system safe and dependable. The software is written in the popular TURBO PASCAL language and reads a data base of I/O channels that can be tailored by the user without modifying the underlying source code.

#### **4.6.3 Parameters monitored and controlled**

The control system monitors and controls several I/O channels in the injector electronics cabinet and the vacuum control panel.

Injector operation I/O channels:

<u>Channel Name</u>	<u>Type</u>
Gas Pressure	A to D
Arc Voltage	A to D

Arc Current	A to D
Filament Current	A to D
Magnet Current	A to D
Pierce Anode Voltage	A to D
Extraction Voltage	A to D
Average Beam Current	A to D
Ion Gauge Pressure	A to D
Pulsed Beam Current	A to D
Gas Flow Voltage	D to A
Arc Power Supply Voltage	Digital Output
Filament Current	Digital Output
Magnet Voltage	Digital Output
Pierce Anode Voltage	Digital Output
40 kV Power Supply Voltage	Digital Output
30 kV Power Supply Voltage	Digital Output
Ion Gauge Start/Stop	Digital Output
Ion Gauge Select	Digital Output

Timing and setup I/O channels:

Arc Capacitor Voltage	A to D
+15 Volts	A to D
-15 Volts	A to D
+ 5 Volts	A to D
Sample & Hold Delay	D to A
Rate Control Voltage	D to A
Beam Gate Delay	D to A
RF Gate Delay	D to A

Beam Pulse Width	D to A
RF Pulse Width	D to A
HV Power Supplies On/Off	Digital Output
Pulse Repetition Rate	Digital Output

Vacuum control I/O channels:

Valves 1-9 Status	Digital Input
Valves 1-9 Open/Close	Digital Output
Compressor Run	Digital I/O
Compressor Overtemp	Digital Input
Valve Busy	Digital Input

For digital to analog channels, we have to set parameters during the experiments. We only need to monitor the parameters of the analog to digital channels during the experiments.

#### **4.6.4 Operation procedures for the AccSys Technology DL-1 RFQ accelerator**

The AccSys Technology DL-1 RFQ accelerator is quite easy to operate. The detailed start up procedures are given as followings:

- 1). Turn on the vacuum system. The vacuum system can also be operated remotely from the computer screen (screen number 3).
- 2). Turn on the RF high voltage power supply. The switch is in the RF cabinet.

3). Do the system operation. The system operation display screen controls and monitors the operation of the ion source power supplies, gas flow, injector and ion source arc chamber pressure and the high voltage for the extraction gap and einzel lens.

During the operation process we need to set the filament current first. Generally we set it to 10 amps, then we need to wait and let the chamber pressure fall below 300 millitorr. For 15 amps and above, the pressure should not exceed 120 millitorr. Observing the above constraints, proceed with filament current increases of approximately 1 amp, waiting for several minutes between increments for the filament to reach thermal equilibrium. Filament current setting is complete when the operating current is achieved and the chamber pressure is less than 20 millitorr. Set the Arc power supply voltage around 280 V, set the magnet current from 0.5 to 1.7 A, set the pierce anode voltage to 36 V, HVPS #1 to 25 V and HVPS #2 to 23 V. Then we can increase the gas flow voltage to the operating level while maintaining the chamber pressure below 250 millitorr.

4). Set the arc enable "on" to enable the arc pulse. Initially, the arc power supply voltage may need to be set higher than the operating voltage to strike the arc. Once an arc has been struck, gradually return the arc voltage to its previous setting. The operating arc current should be approximately 10 Amps.

5). Set HVPS on. The injector beam pulse should 10 to 15 mA. We can adjust the ion source parameters and high voltage power supplies for highest beam current and best pulse shape.

If the beam current is 10 mA and the repetition rate is 160 Hz so we can get the total neutron yield should be  $10^{10}$  n, see Figure 4.9.

We can also change the repetition rate of the pulse in order to get more neutrons.

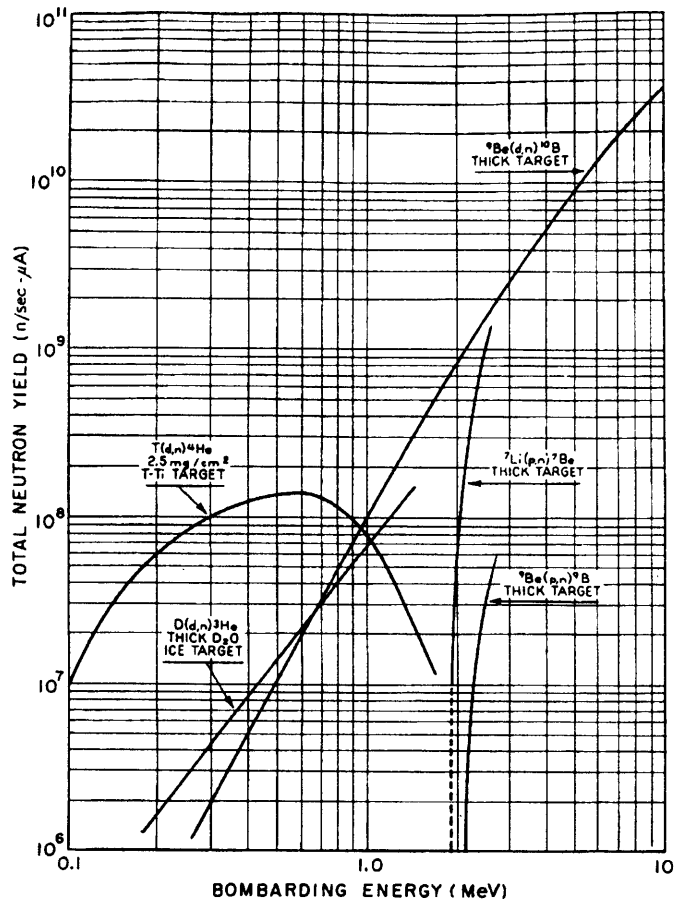


Figure 4.9: Total neutron yields versus bombarding energy for several accelerator produced neutron reactions. The yields are given per microampere of bombarding particle current [7].

# Chapter 5

## Software development for three-dimensional reconstruction for neutron tomography

In this chapter, the 3-D reconstruction methods for our tomography system are discussed. We first indicate the difference between radiography and tomography and point out that tomographic reconstruction is a bridge between two dimensional projection data and the three dimensional object distribution function. Two reconstruction methods are discussed specifically. Finally, we talk about 3-D reconstruction software development for our neutron tomography image system on our Silicon Graphics 4D/240GTX workstation.

### 5.1 Radiography and tomography

In radiography, whether photon, electron, or neutron, we get a two dimensional projection image from three dimensional object by integrating along the path of the radiation. Contrast in radiography is due to spatial differences in the attenuation of the radiation within the object, which depends on the interaction of radiation with matter. With radiography, we can only relate differences in contrast to properties averaged over the path of radiation; we cannot determine properties of a point occurs within the three

dimensional object. Plainly, for medical or industrial diagnostic applications, radiography alone is not enough since we want to know the exact spatial distribution function of an object property. Tomography is a powerful nondestructive evaluation technique (NDE) for detecting the internal structure of objects. The theoretical development of computed tomography has its roots in 1917 by Radon [42], but due to the limitations of computation ability and the lack of availability of radiation technique, there was no great progress in the tomography imaging field in the early years. With the development of powerful computer technology and the development of radiation techniques, vast progress on tomographic imaging techniques was made. A significant break-through occurred when Cormak (1969) and Hounsfield (1973) developed the first medical imaging system, for which they shared the 1979 Nobel prize in medicine [43]. A few years later, the X-ray tomographic imaging system was commercially available. Although computed tomography has found its biggest field of application in medicine, it has also been applied to nondestructive testing of materials and industrial objects. The basic idea for tomographic imaging is to illuminate the object with a radiation source, such as X-rays, or a neutron beam. We take a series of planar radiographs and then turn the object a certain angular interval or turn the source. Then we take another radiographic image, until turns over an angle of  $180^\circ$  are completed. From all of the collected radiographic image data, we can reconstruct the three dimensional object. Figure 5.1 shows the difference between radiography and tomography.

Clearly tomography has many of advantages over radiography:

- 1). Tomography provides a three dimensional distribution of density of the object. This is very important for medical surgery, since the doctor has to know the exact position of the tumor before operating. For industrial nondestructive testing, it is also important to find the right position and repair it in order to save a lot of human power and money.

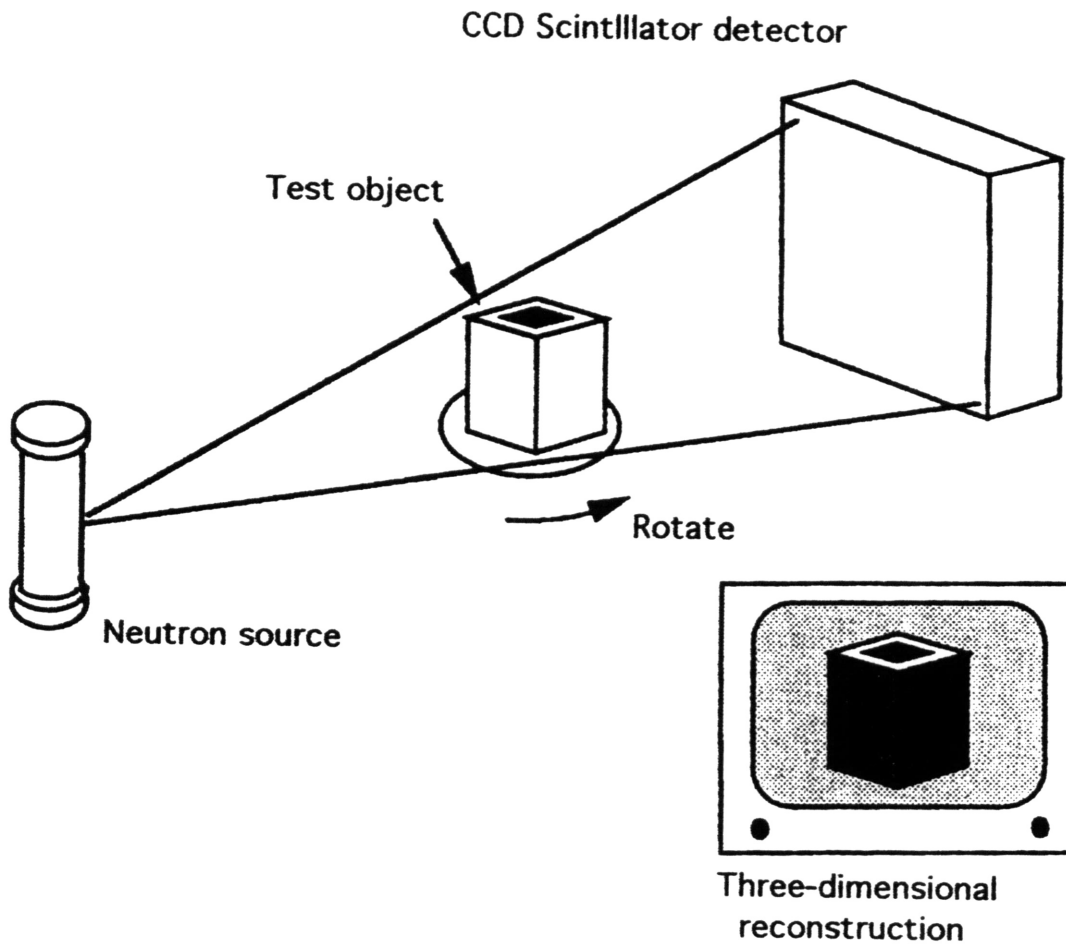
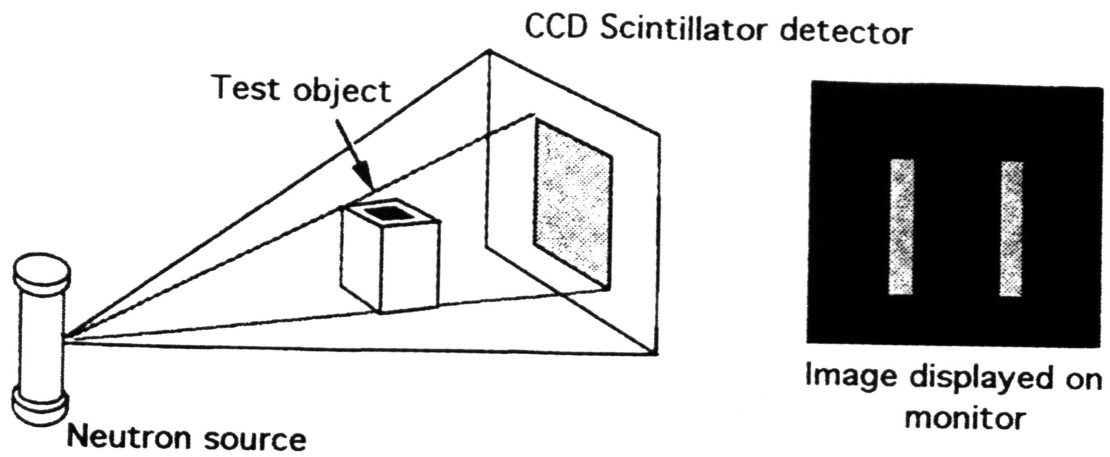


Figure 5.1: The difference between radiography and tomography.

2). Tomography has the contrast and resolution comparable to radiography .

3). After we get the reconstructed three dimensional object distribution function, we can change the viewing angle. This is impossible for radiography.

## 5.2 Two dimensional reconstruction

Tomographic reconstruction is a bridge between two dimensional projection data and the three dimensional object distribution function, as shown in Figure 5.2.

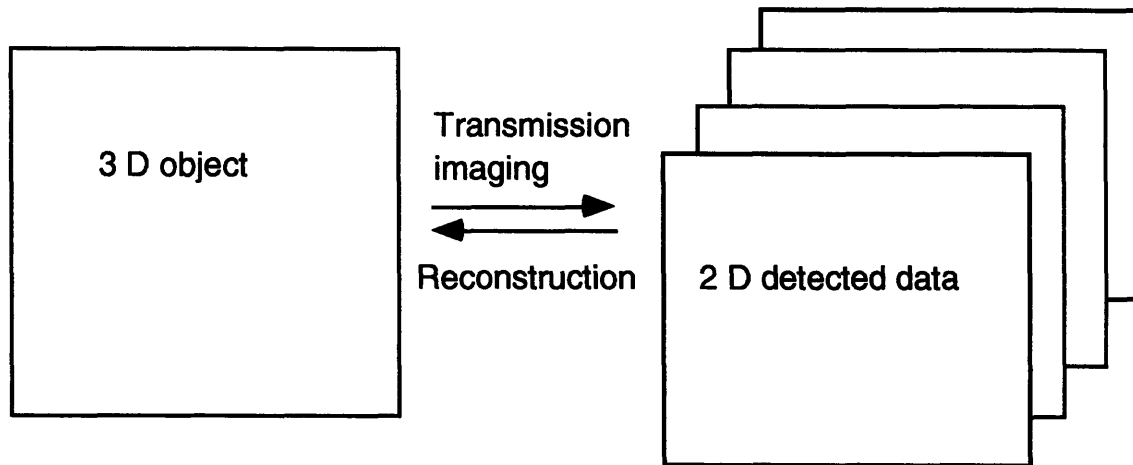


Figure 5.2: The relationship between 2-D projection data and 3-D object.

Reconstruction is a key step for tomographic imaging technique. We have developed a reconstruction software on our Silicon Graphics 4D/240GTX workstation which allows us reconstruct a three dimensional object from two dimensional projection data quite easily.

## 5.2.1 Two dimensional reconstruction algorithms

To illustrate the question simply, we will consider two dimensional tomography; later we will discuss the three dimensional case. As we mentioned earlier, the detected data can be written as a mathematical transform of the line integral of an object property over the radiation path. Assume  $f(x, y)$  is the two dimensional distribution function of the object property and an array of line integrals is measured or detected, each integral being at distance  $R$  from the origin where the perpendicular to the line is at an angle  $\theta$  (see Figure 5.3). So the measured signal can be written as a line integral transform:

$$g_{\theta}(R) = \iint f(x,y)\delta(x \cos \theta + y \sin \theta - R) dx dy \quad (5.1)$$

$$= \int_0^{2\pi} \int_0^{\infty} f(x,y)\delta(r \cos(\theta - \phi) - R) r dr d\phi \quad (5.2)$$

where  $g_{\theta}(R)$  is the projection information in the  $\theta$  direction. The integral takes place along line,  $x \cos \theta + y \sin \theta = R$ , or, in polar coordinates  $r, \phi$ ,  $r \cos(\theta - \phi) = R$ . If we know  $f(x, y)$ , we can use the integral to get  $g_{\theta}(R)$ . In the real world the situation is reversed. Our goal is to reconstruct the object function  $f(x, y)$  from the measured or projection function  $g_{\theta}(R)$ . This is a quite common and quite realistic problem [44] in such fields as X-ray tomography to detect tumors and cysts, nuclear magnetic resonance imaging, positron emission tomography and ultrasound in medicine, holographic interferometer on optics, radar remote sensing in astronomy, electron microscopy in molecular biology, stress analysis in material science and engineering, seismic profile reconstruction in geophysics,

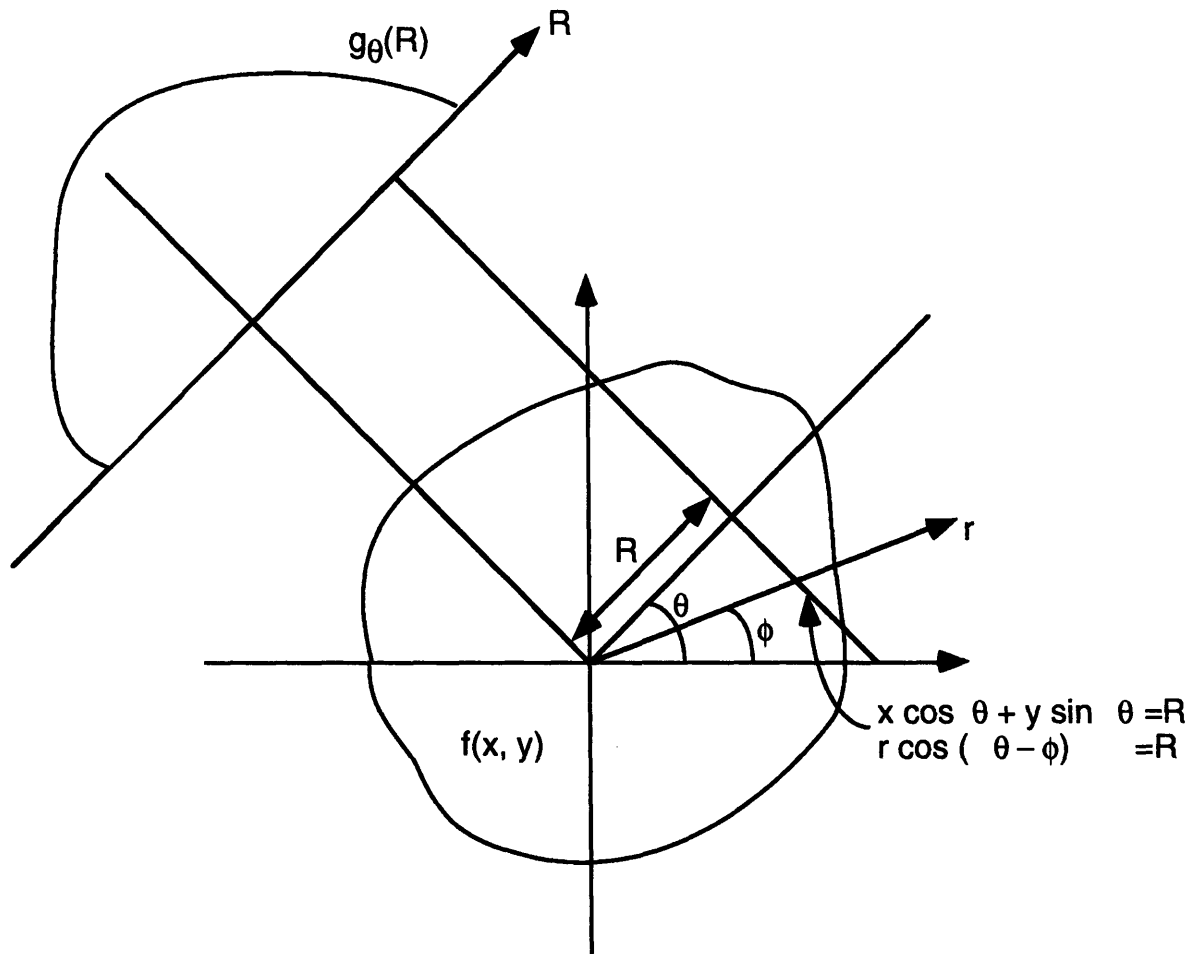


Figure 5.3: Projection of a two dimensional object function.

air pollutant studies in environmental science, and integral transforms in mathematics. In our neutron transmission image, the neutron beam intensity detected is given by:

$$I(R, \theta) = I_0 \exp \left[ - \int_{-x_0}^{x_0} \int_{-y_0}^{y_0} \mu(x, y) \delta(x \cos \theta + y \sin \theta - R) dx dy \right] \quad (5.3)$$

where  $\mu(x, y)$  is the linear attenuation coefficient of the object which we detected and  $I_0$  is the incident neutron beam intensity. If we define:

$$g(R, \theta) \equiv -\log(I(R, \theta)/I_0) \quad (5.4)$$

Equation (5.4) is then turned into the Radon transform of equation (5.1)

The mathematical analytical inversion was first obtained by Radon in 1917:

$$f(x, y) = -\frac{1}{2\pi^2} \int_0^\pi d\theta \int_{-\infty}^{\infty} dR \frac{1}{R - r\cos(\varphi - \theta)} \frac{\partial g(R, \theta)}{\partial R} \quad (5.5)$$

The problem was, however, far from being solved from the practical point of view because to carry out equation (5.5) one needs first to know the continuous form of  $g(R, \theta)$  and this is impossible in any practical application. In practice, it is impossible to measure the line integrals through all the lines across the plane. Also, the lines have a finite width, so what we really can detect is a finite subset of strip-integral. Second, the differentiation involved can be very sensitive to noise present in the actual data. Therefore, the analytical inversion formula has found little use in practical situations. In our experiments, we use a CCD-camera to collect the projection data. We have to use numerical methods to get the reconstructed three dimensional object distribution function. Figure 5.4 shows the projection data for parallel beam tomography consisting of parallel strip integrals through the object at various angles.

## 5.2.2 Numerical solution for reconstruction

Many efforts and a great deal of research have gone into reconstruction methods. No single method, in general, can cover all of the applications, since there are vastly different sampling schemes and characteristics of source function. Nevertheless one thing is identical in all of the applications, the continuous condition of the projection function.

This demands that for any kind of detection application we should reduce the noise as much as possible.

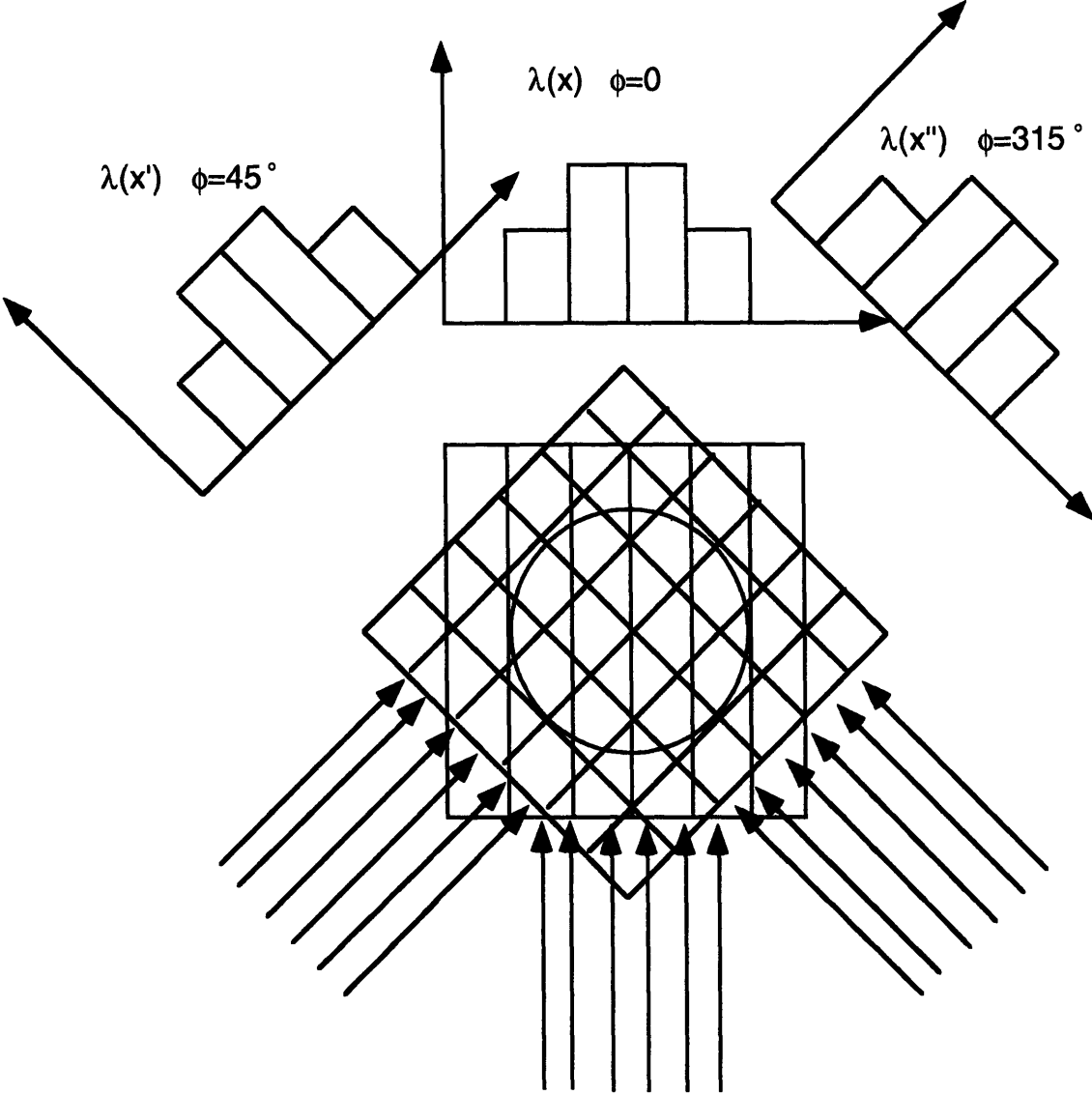


Figure 5.4: Projection measurements for an 2-D object at three different angular positions with 6 strip integrals.

The methods most widely used in tomography are: transform (analytical) method, finite element method and series expansion method. In our neutron tomographic image system due to the properties of the source we will use the transform method.

### 5.2.2.1 Filtered back projection

The concept of back projection is very simple [45]. Assume we have a spherical object. By making projections at angle  $0^\circ$ ,  $10^\circ$ ,  $20^\circ$ , .... until  $180^\circ$ , we get projection data files at each angle. It is reasonable, as an initial attempt at reconstruction, we assign the measured value along the entire line. In the simple back projection method the measurements obtained at each projection are projected back along the same line. Thus the measured values are "smeared" across the unknown density function as if it were a line of wet ink, containing the measured projection values, drawn across the reconstructed density function. Mathematically, the back projection of a single measured projection along the unknown density is given by:

$$b_{\theta}(x, y) = \int g_{\theta}(R)\delta(x \cos \theta + y \sin \theta - R)dR \quad (5.6)$$

where  $b_{\theta}(x, y)$  is the back projected density due to the projection  $g_{\theta}(R)$  at angle  $\theta$ . Adding up these densities at all angles, we have:

$$\begin{aligned} f_b(x, y) &= \int_0^{\pi} b_{\theta}(x, y)d\theta \\ &= \int_0^{\pi} d\theta \int_{-\infty}^{\infty} g_{\theta}(R)\delta(x \cos \theta + y \sin \theta - R)dR \end{aligned} \quad (5.7)$$

where  $f_b(x, y)$  is the crude reconstruction resulting from pure back projection.

For a spherical object, each projection is identical. Back projection produces a blurred reconstruction [46]. This means back projection is a poor method for reconstruction. How can we get rid of these blurs? We have to find a new way to get the desired reconstruction results. One of the methods we can use is the filtered back projection (FBP) reconstruction method. Intuitively, Figure 5.5 shows the difference between back projection (this reconstruction is often called a laminogram) and a filtered back projection.

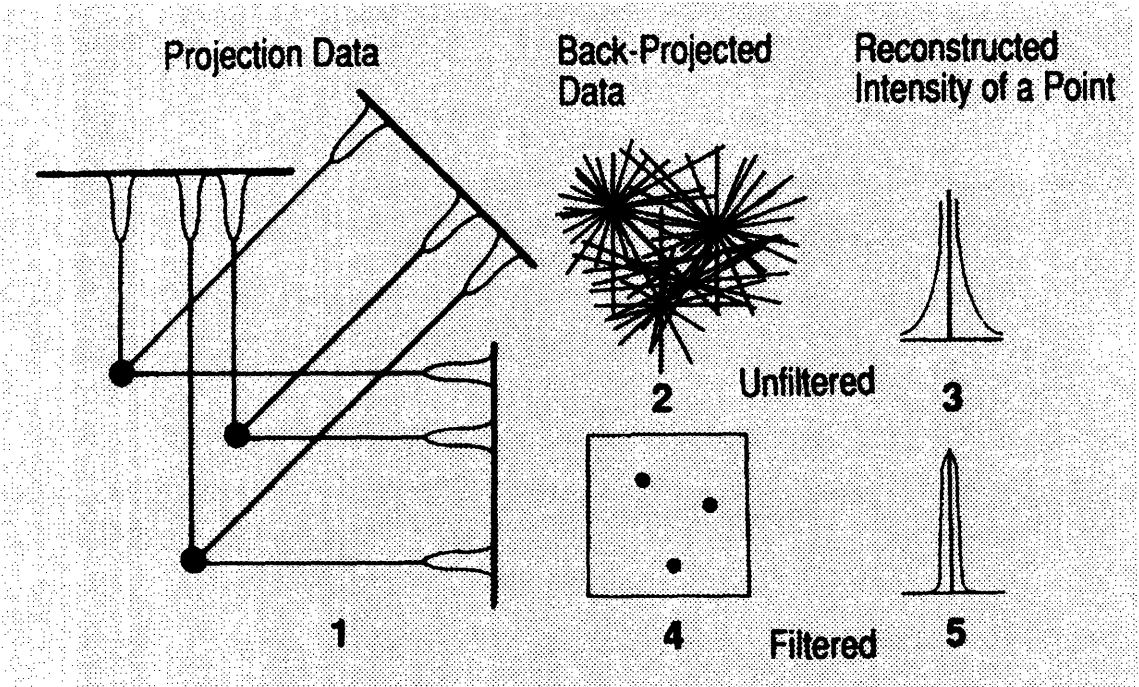


Figure 5.5: A comparison of BP and FBP.

Mathematically, for the filtered back projection method we start by restating the back projection relationship for the laminogram  $f_b(x,y)$  as:

$$f_b(x, y) == \int_0^\pi d\theta \int_{-\infty}^{\infty} g_\theta(R) \delta(x \cos \theta + y \sin \theta - R) dR \quad (5.8)$$

and restructuring it into a Fourier transform mode by using the central section theorem to substitute the inverse transform of  $F(k, \theta)$  for  $g_\theta(R)$  as given by:

$$f_b(x, y) == \int_0^\pi d\theta \int_{-\infty}^{\infty} \left[ \int_{-\infty}^{\infty} F(k, \theta) e^{i2\pi k R} dk \right] \delta(x \cos \theta + y \sin \theta - R) dR \quad (5.9)$$

Performing the integration over  $R$ , we obtain:

$$f_b(x, y) == \int_0^\pi d\theta \int_{-\infty}^{\infty} F(k, \theta) \exp[i2\pi k(x \cos \theta + y \sin \theta)] dk \quad (5.10)$$

Where  $F(k, \theta)$  is the two dimensional Fourier transform of  $g_\theta(R)$ .

If we consider the general two dimensional inverse Fourier transform of  $f(x, y)$ , we have:

$$f(x, y) == \int_0^\pi d\theta \int_{-\infty}^{\infty} F(k, \theta) \exp[i2\pi k(x \cos \theta + y \sin \theta)] |k| dk \quad (5.11)$$

Comparing (5.11) with (5.10), we see the difference only by  $|k|$  weighting. Substituting  $F_1\{g_\theta(R)\}$  for  $F(k, \theta)$  in (5.10), and dividing and multiplying by  $|k|$ , we obtain:

$$f_b(x, y) == \int_0^\pi d\theta \int_{-\infty}^{\infty} \frac{F_1\{g_\theta(R)\}}{|k|} \exp[i2\pi k(x \cos \theta + y \sin \theta)] |k| dk \quad (5.12)$$

This equation provides an alternative interpretation to back projection. In essence, the transform of each projection  $g_\theta(R)$  has been weighted by  $1/|k|$  along each radial line. This accounts for the blurred reconstruction of  $f_b(x, y)$ . This can therefore be removed by

weighting each transformed projection with  $|k|$  prior to back projection to create an undistorted reconstruction as given by:

$$f(x, y) == \int_0^\pi d\theta \int_{-\infty}^{\infty} \frac{F_1\{g_\theta(R)\} \cdot |k|}{|k|} \exp[i2\pi k(x \cos \theta + y \sin \theta)] |k| dk \quad (5.13)$$

This reconstruction approach is called as the filtered back projection (FBP) system.

We summarize the steps for the filtered back projection as follows:

- 1). Set an angle  $\theta_k$ . Here  $k = 1$  to  $N_\theta$
- 2). Collect the projection data file at that angle.
- 3). Take the Fourier transform of the projection at angle  $\theta_k$ .
- 4). Multiply the above with the Fourier transform of the filter.
- 5). Take the inverse Fourier transform of the above product.
- 6). Back project the above result.
- 7). Do the same procedure for the next angle.
- 8). Finish all of the angles.

Figure 5.6 is an example of our numerical reconstruction calculation result. We use 128 angular projections with 128 projection data points at each angle.

There are several choices for the filter, but all are basically ramp filters with high frequency cutoffs. The exact choice depends on the details of a particular application.

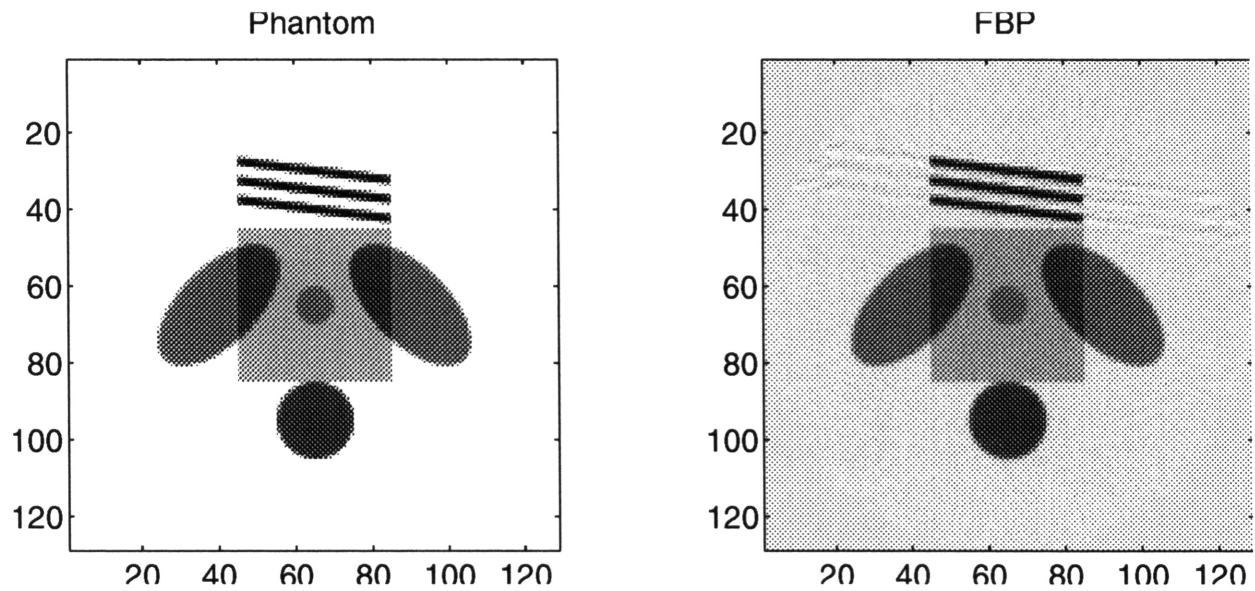


Figure 5.6 Example of filtered back projection numerical reconstruction calculation result.

### 5.2.2.2 Wavelet method

We can also use a new technique developed at MIT by Bhatia and Willsky, multiscale simulation reconstruction [47], to do our reconstruction. With this technique, based on wavelets, a reconstruction is produced at multiple scales simultaneously. If all of the multiple scales are combined, then the results are the same as conventional techniques. Each scale contains only features of that scale; for example, the coarse scale contains coarse spatial information while the fine scale contains fine features such as edges and boundaries.

The advantage of this technique lies in the ability to trade off reconstruction time and resolution during initial fast scans to discover possible problems in the object under investigation by fine scale reconstruction which could be used to extract edges and features. In conventional tomography, a complete high resolution reconstruction is made, followed by post processing of the image to extract features. Thus, with multiscale

reconstruction, an initial quick reconstruction can be made to determine areas of corrosion, followed by a subsequent interactive zooming in on the region of interest at high resolution if corrosion is detected.

We summarize the steps for the wavelet method as follows:

- 1). Set an angle  $\theta_k$ . Here  $k = 1$  to  $N_\theta$
- 2). Collect the projection data file at that angle.
- 3). Take the wavelet transform of the projection at angle  $\theta_k$ .
- 4). Multiply the above with the wavelet transform of the filter.
- 5). Take the inverse wavelet transform of the above product.
- 6). Back project the above result.
- 7). Do the same procedure for the next angle.
- 8). Finish all of the angles.

Figure 5.7 is an example of our numerical reconstruction calculation result. We use 128 angular projections with 128 projection data points at each angle.

## **5.3 Three important reconstruction issues in our experiments**

### **5.3.1 Reconstruction result changes with $N_\theta$**

For the reconstruction calculation we vary the number of samples per angular projection and the number of angular projections. In our experiments we can control the turn table

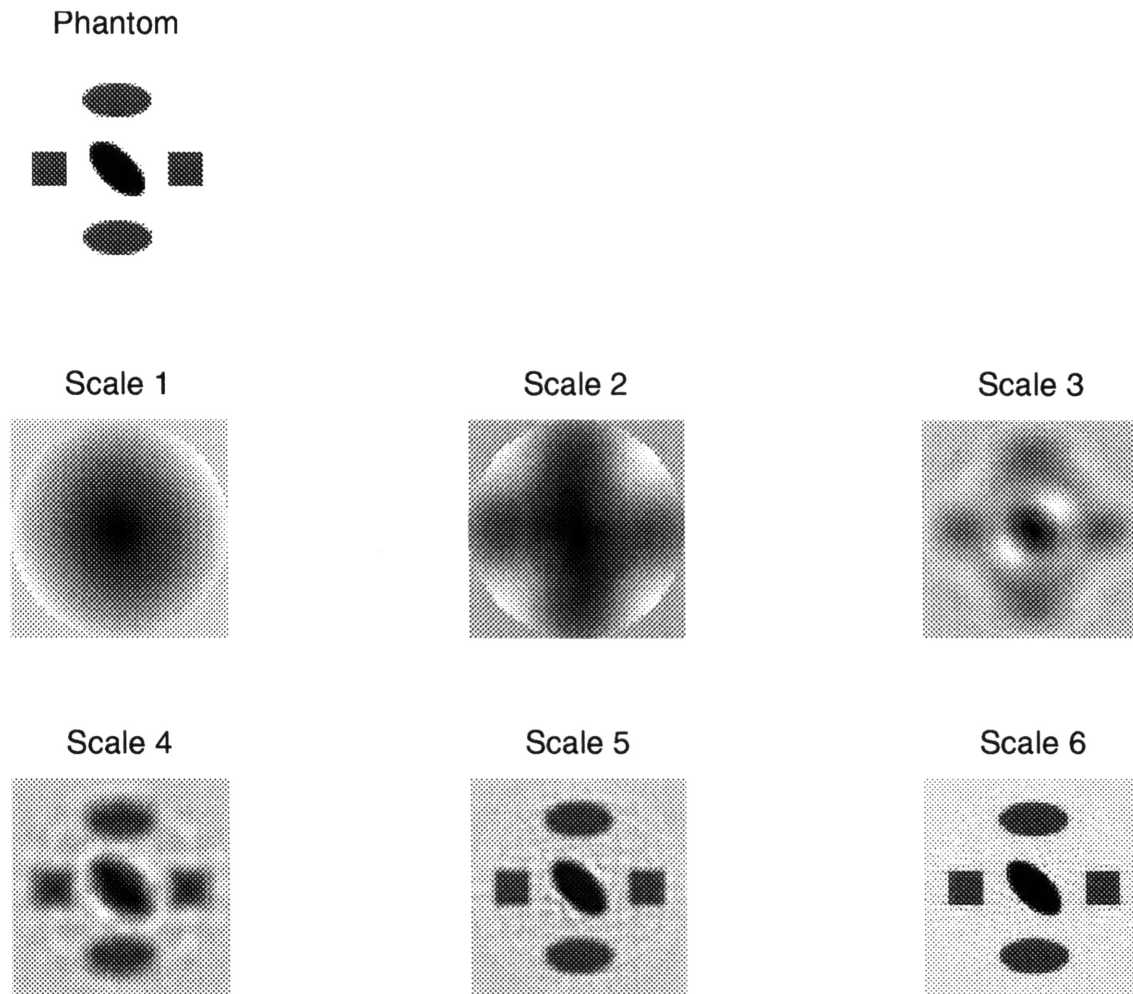
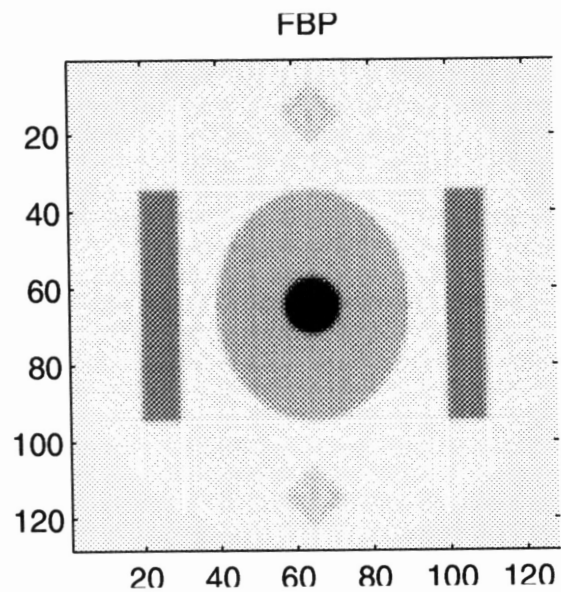
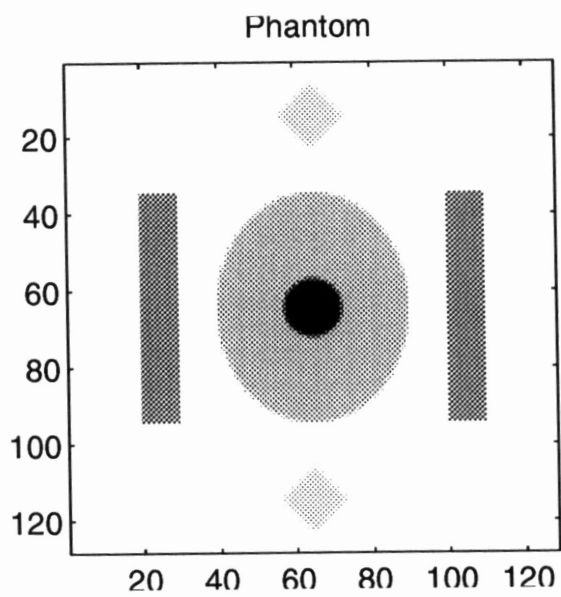
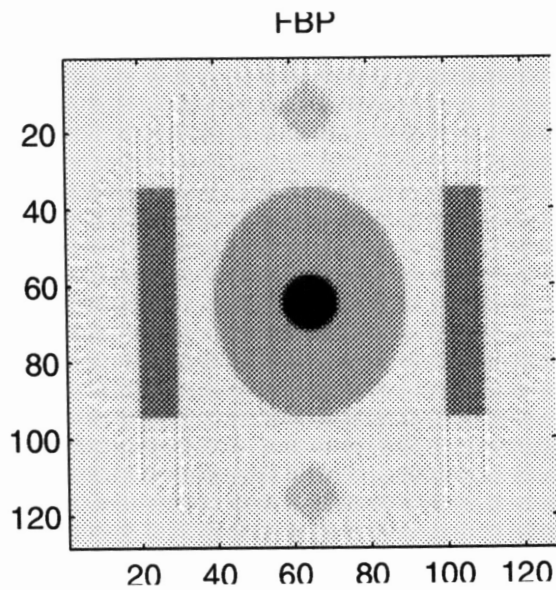
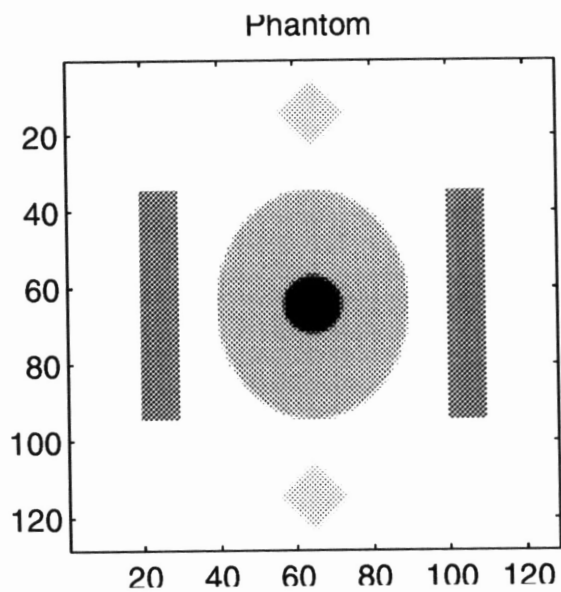


Figure 5.7: Examples of reconstruction using wavelet technique. Using the same data set, the image may be reconstructed on various scales depending on the desired resolution and reconstruction time.

so we can determine how much of an angle we want to turn the object through each time. It is important to find an optimized way to determine how much angle we should turn at each time, since if we use a smaller angle, we need a longer time to collect all of the data and we need more space to save them. If we use a larger angle we will lose the detailed information of the object. Figure 5.8 shows some simulation results.



(a)  $N_\theta = 128$



(b)  $N_\theta = 64$

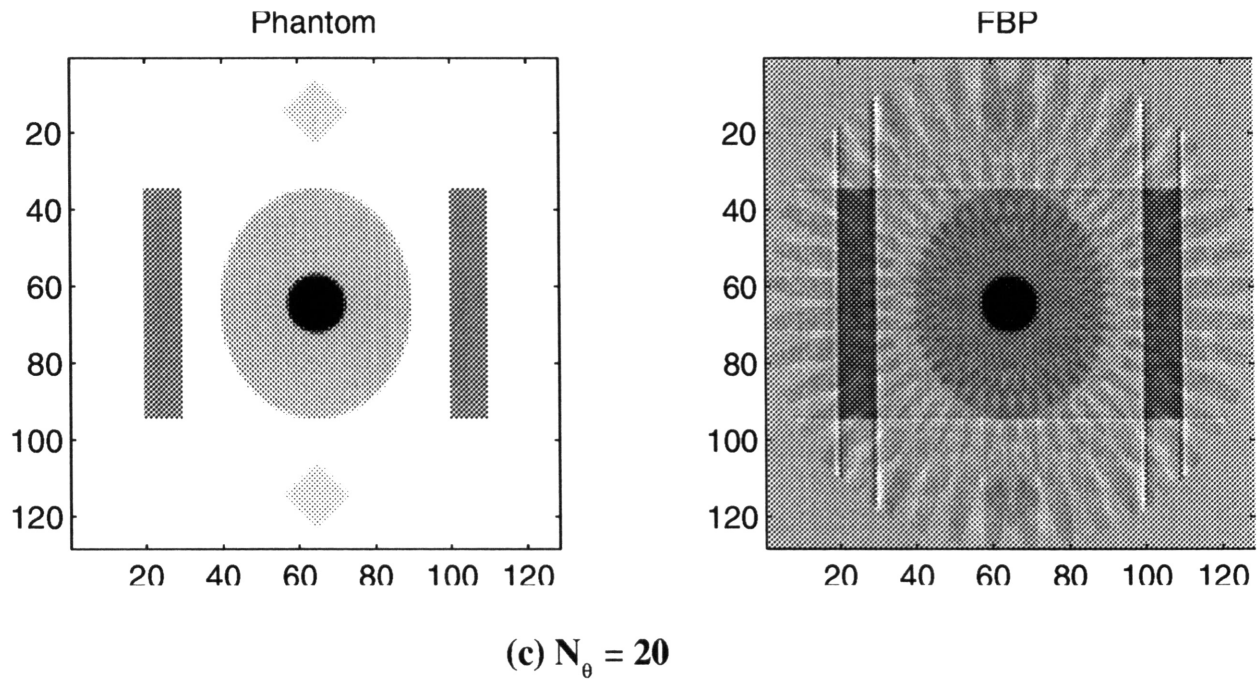


Figure 5.8: Reconstruction results at different  $N_\theta$  and  $N_s = 128$ . (a)  $N_\theta = 128$ ,  
 (b)  $N_\theta = 64$ , (c)  $N_\theta = 20$ .

Where  $N_\theta$  is angular projections to be measured,  $N_s$  is the strips in each angular projection.

Figure 5.9 shows the intensity map of the 128X128 phantom shown in Figure 5.8. The numbers shown are the intensities of respective regions. The projection data are gathered using a parallel beam geometry with  $N_s = 128$ .

It is clear that if  $N_\theta = 20$ , the reconstructed object is not very well matched to the real object. We have particularly lost the information of the top and bottom small squares. When  $N_\theta = 64$ , we get a reasonable result. The bigger  $N_\theta$  is, the better result we can get, but as a trade-off we need longer data acquisition time and reconstruction time.

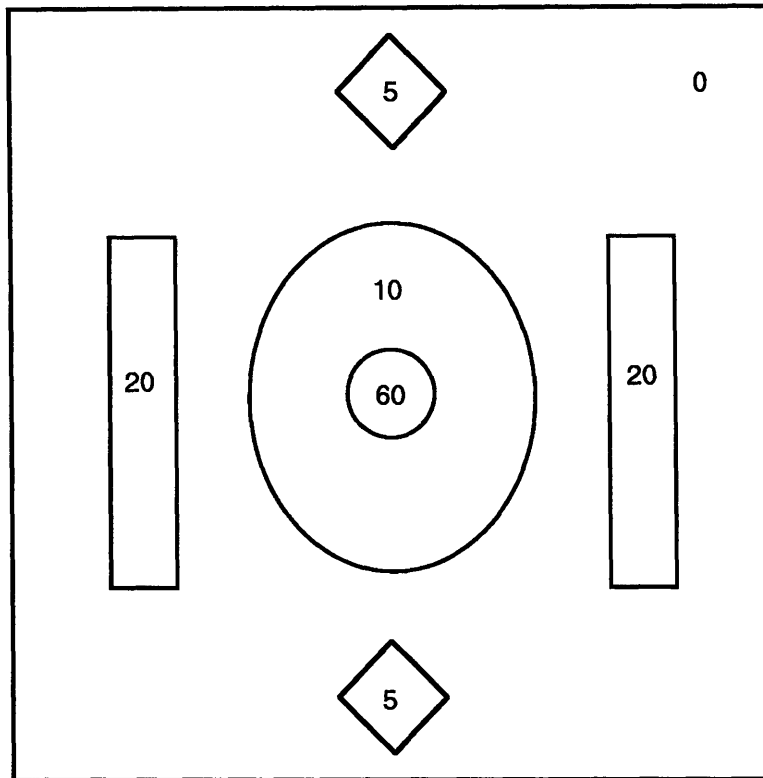


Figure 5.9: The intensity map of the 128X128 phantom shown in Figure 5.8. The numbers shown are intensities of respective regions. The projection data are gathered using a parallel beam geometry with  $N_S = 128$ .

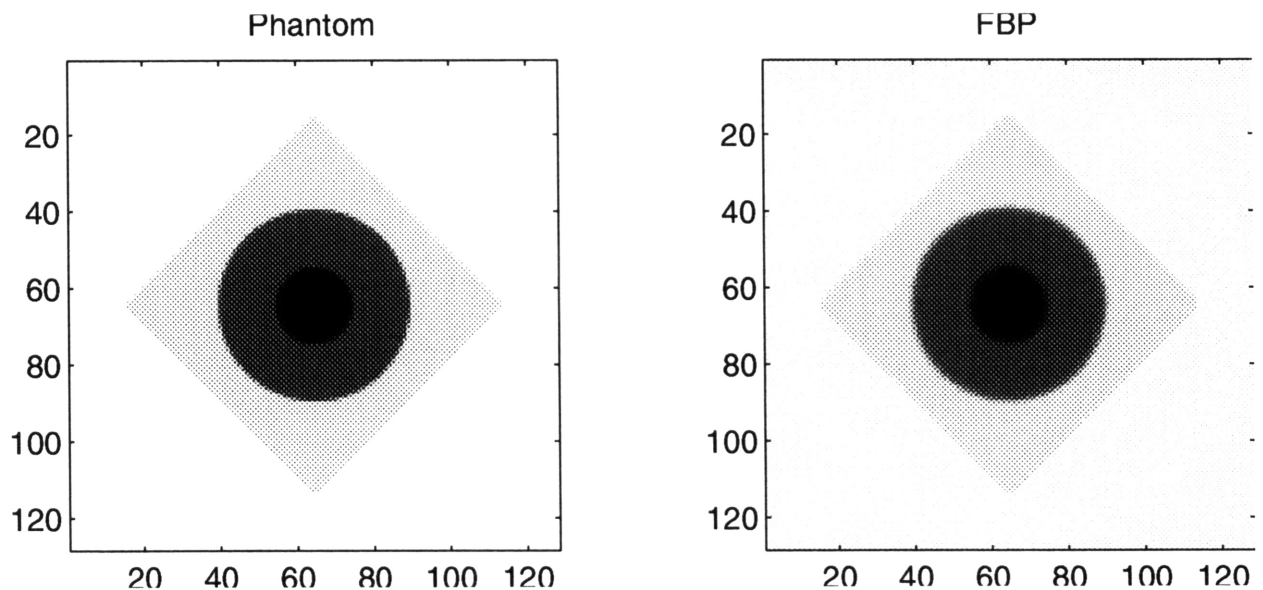
### 5.3.2 Cut-off frequency

The term "filtered" is only formal because we have converted the two dimensional Fourier transform into a one dimensional Fourier transform and an angular integration (back projection). As a result, the one dimensional Fourier component is multiplied by a "filtering" function  $|k|$ . In fact, no real space filtering is ever performed because this requires us to know the real space distribution function for the object  $f(x, y)$ , which is exactly the function we want to determine. In the discrete Fourier transform, there is always a maximum  $k_m$  which is determined by the sampling frequency of the detection system. This maximum frequency is different from the maximum frequency which band

limits the frequency of the function  $f(x, y)$  we want to sample. According to the Nyquist condition one needs the sampling frequency to be at least twice the maximum band limited frequency of the signal to be sampled. Therefore, for a given sampling frequency, we must assume our function to be sampled is band limited by a maximum frequency which is half of the sampling frequency. Otherwise the "aliasing" effect will corrupt the reconstruction. Figure 5.10 shows the results cutoff at different km. Figure 5.11 shows the intensity map of 128 X 128 phantom shown in Figure 5.10.

### 5.3.3 Noise

Noise is a very important issue in tomographic imaging systems. If the noise level is too high, we can not get a high quality image, or even detect signals. Figure 5.12 shows some of our reconstruction calculation results when we considering the effects of noise. We calculate several cases with different signal to noise ratio, SNR.



(a)  $f_c = 0.85$

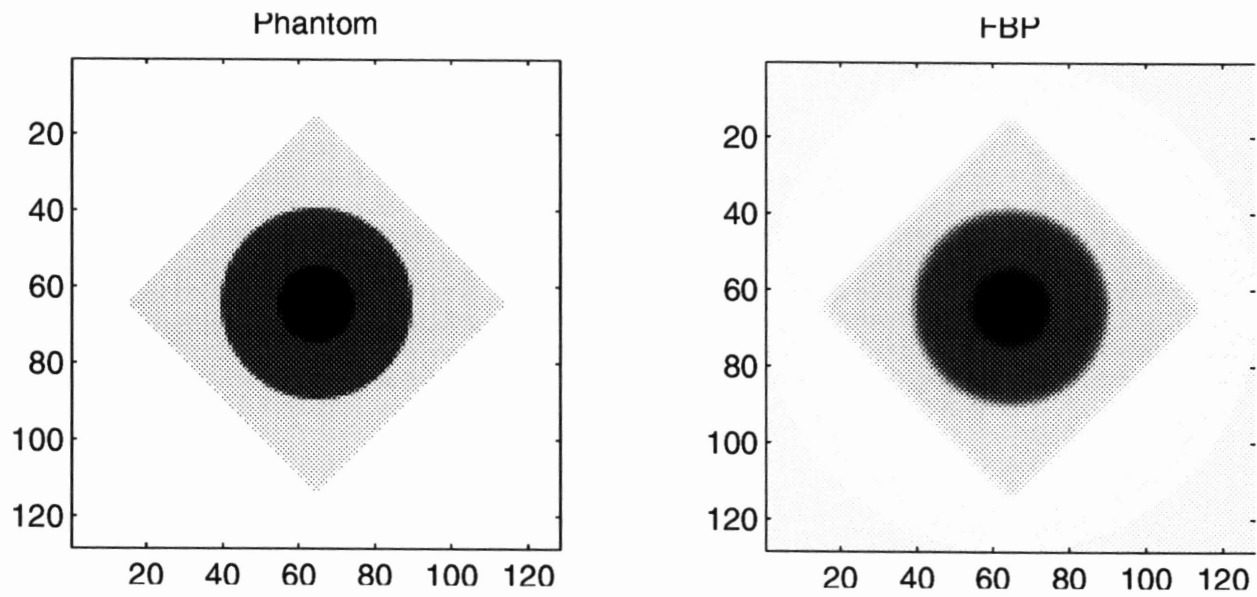
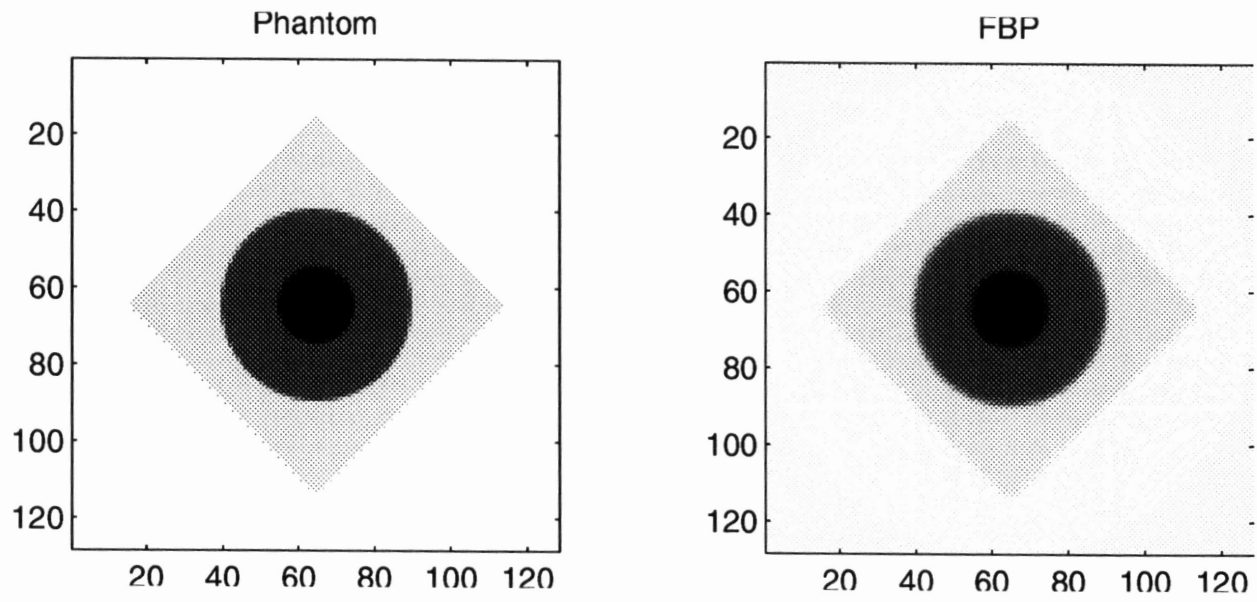


Figure 5.10: Reconstruction results at different cut off frequency. (a)  $f_c = 0.85$ ,

(b)  $f_c = 0.75$ , (c)  $f_c = 0.5$ .

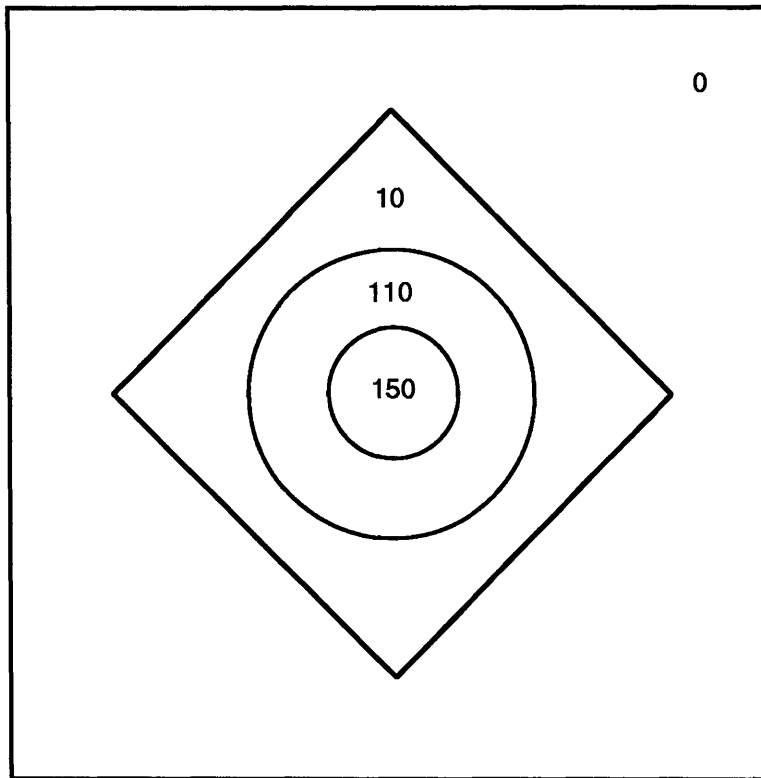
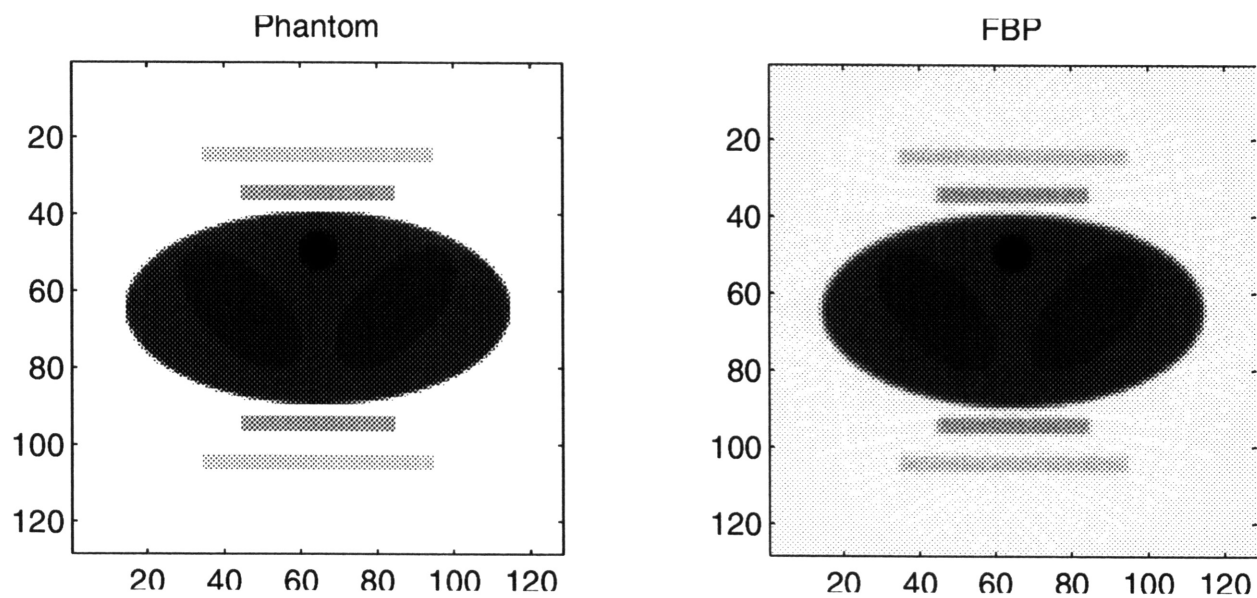


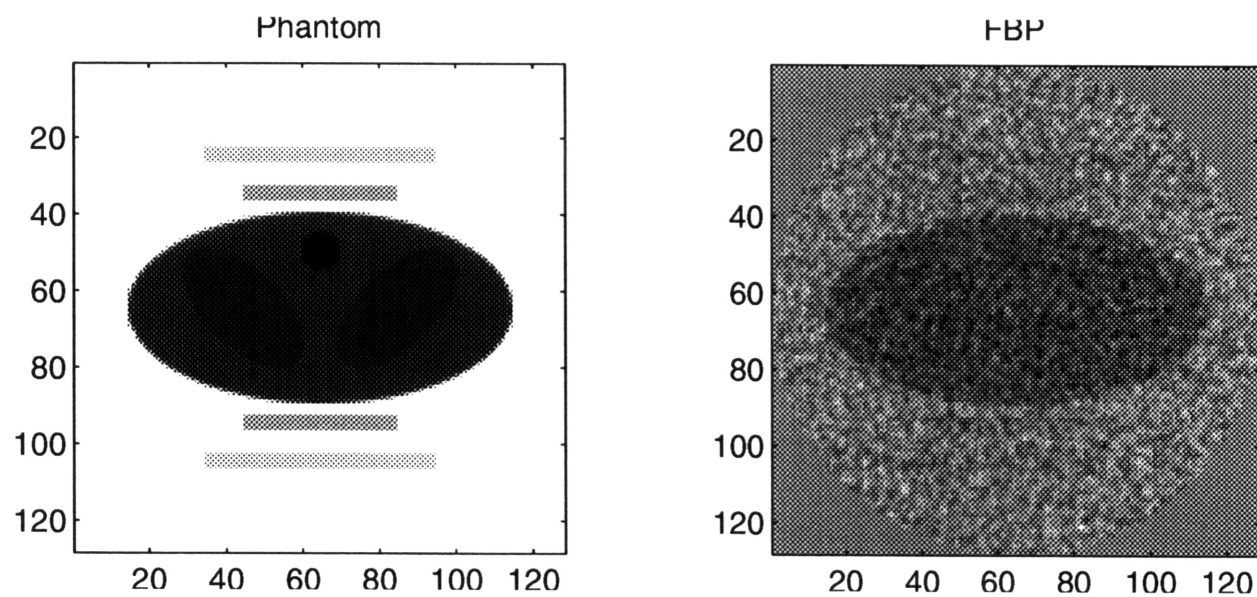
Figure 5.11 The intensity map of the 128X128 phantom shown in Figure 5.10. The numbers shown are intensities of respective regions. The projection data are gathered using a parallel beam geometry with  $N_s = 128$  and  $N_\theta = 128$ .

We can see that when the SNR ratio equals 100, we can get fairly good reconstruction results for the phantom which shown in Figure 5.12. For SNR equals 30, the features in the object can barely be seen. For the SNR equals 10, the reconstructed results are very poor. Figure 5.13 shows the intensity map of 128 X128 phantom shown in Figure 5.12.

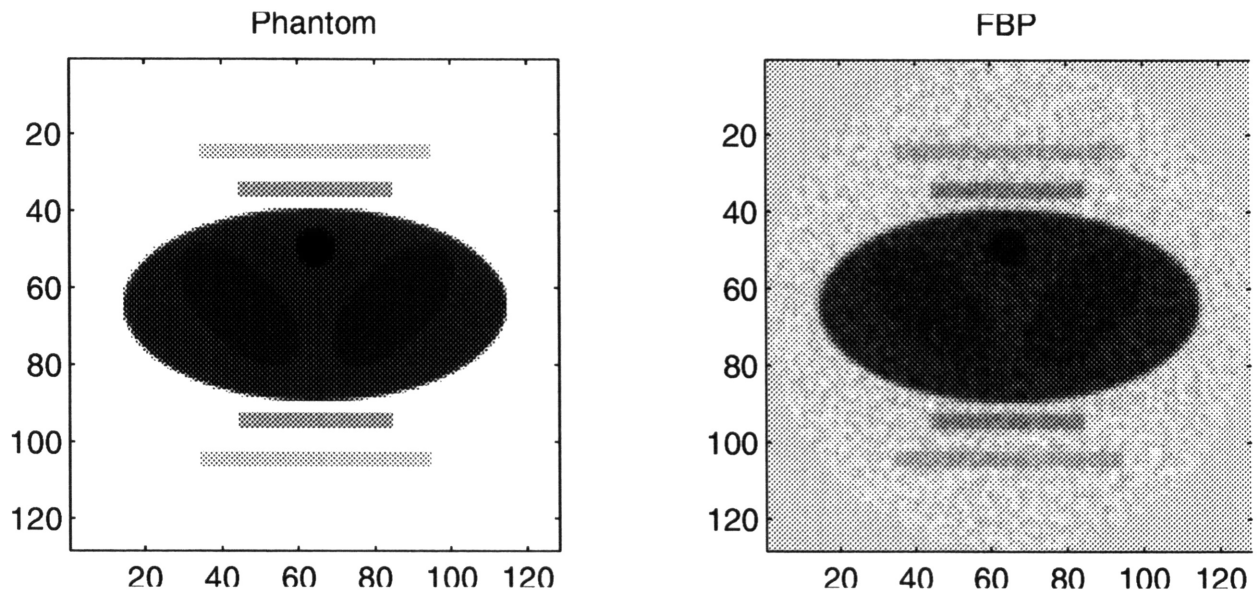
In order to get a high quality image we have to reduce the noise level as much as possible, that is why we want to operate the CCD-camera at the lowest temperature we



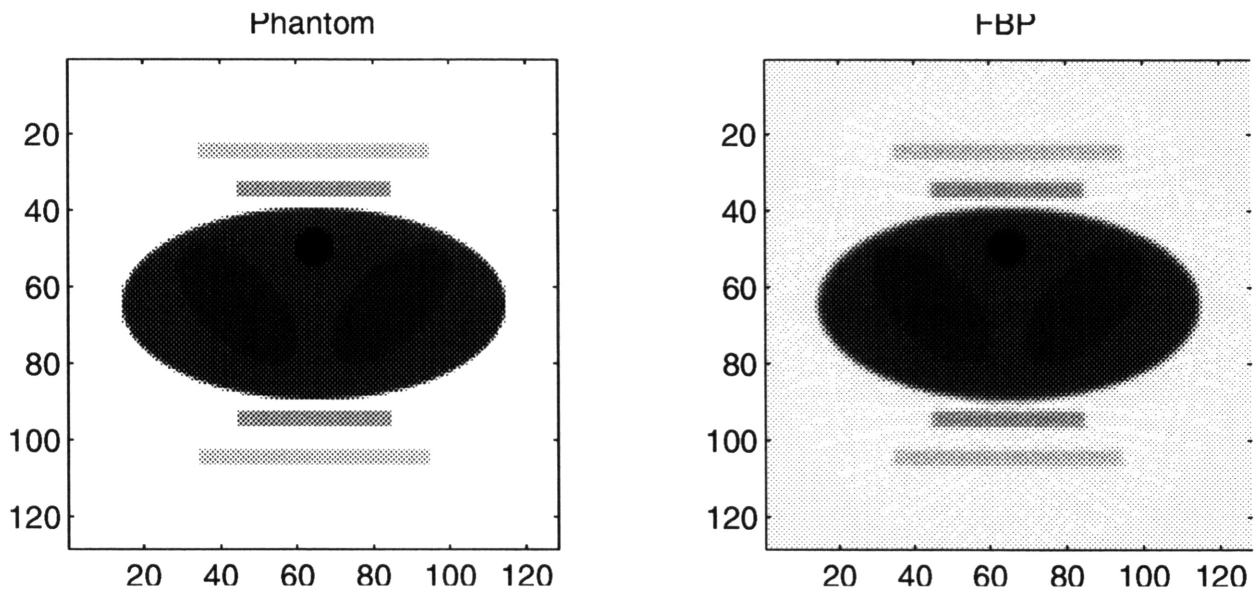
(a) SNR = infinite



(b) SNR = 10



(c) SNR = 30



(d) SNR = 100

Figure 5.12: Reconstruction results for different signal to noise ratio with  $N_S=128$  and  $N_\theta=128$ . (a) SNR=infinite, (b) SNR=10, (c) SNR=30, (d) SNR=100

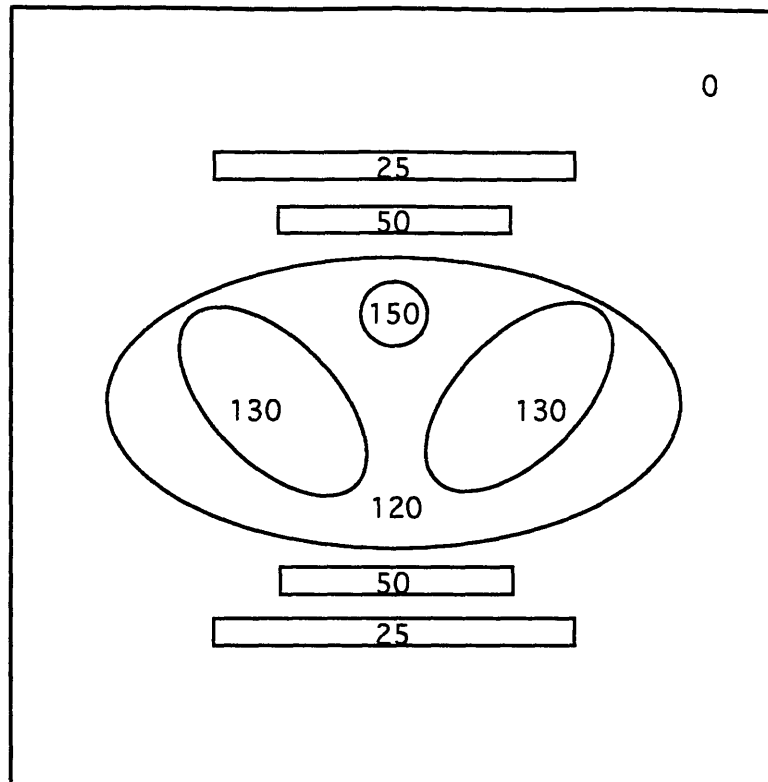


Figure 5.13: The intensity map of the 128X128 phantom shown in Figure 5.12. The numbers shown are intensities of respective regions. The projection data are gathered using a parallel beam geometry with  $N_S = 128$ .

can achieve. But some "noise" produced by background and our system can not be avoided. Traditional image techniques use film to record the image. Generally speaking, an image has both signal and noise information on it, but due to the technique they used, they can not do any thing with it. For our image system since we use CCD-camera as the detector instead of traditional film, after we take the image we can do some image manipulation, such as add two images together, or subtract two images. This kind of detector system has more powerful abilities than any detector system which was built before.

We can take advantage of this powerful ability in our experiments. First we take a background noise image. Then we use our neutron beam to take another image. We subtract the two images, and the result has the system noise removed.

## 5.4 Three dimensional reconstruction method

For two dimensional reconstruction, i.e., slices across objects, line projections are required, while for full three dimensional reconstruction, area projections are required. In our experimental system we use a CCD-camera as two dimensional detector, and we need to reconstruct a three dimensional object function from two dimensional detected data sets. We use IPLab software for Macintosh to control our camera, and collect our images. We then transfer these data files to a Silicon Graphics 4D/240GTX workstation, where we reconstruct the three dimensional object as a series of slices. Figure 5.14 shows the relationship between slices and the three dimensional reconstruction result.

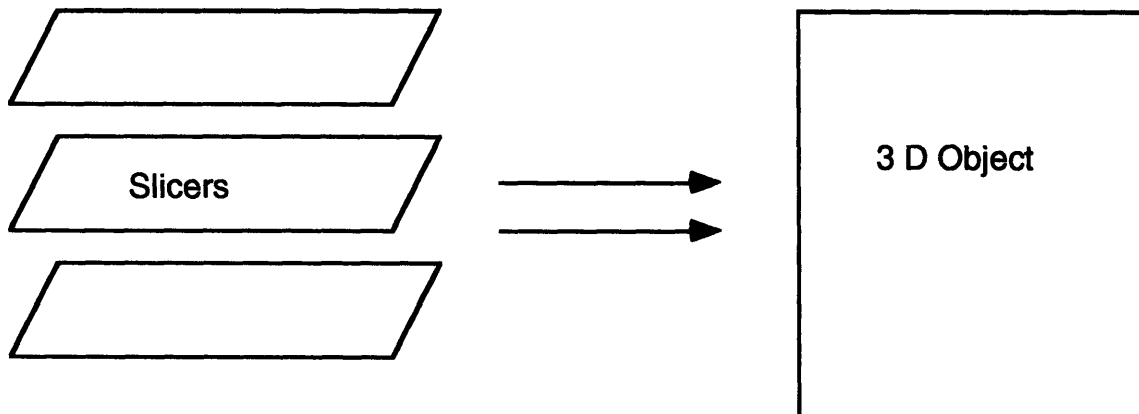


Figure 5.14: The relationship between slice and three dimensional reconstruction result.

Assuming we turn the object  $2^\circ$  each time, until it is turned over  $180^\circ$ , we have 90 detected two dimensional data files. We put all of these data files into a program which

we called it as "slicer". The main purpose of this program is to give us a series of output files; for each file a single line of projected data for each imaging slice plane was given. We can use this output file as input for the two dimensional reconstruction, after the reconstruction we get one slice of the object function. By continue doing this procedure one by one, we will get a data sets of the slices. Put all of these slices together we can get

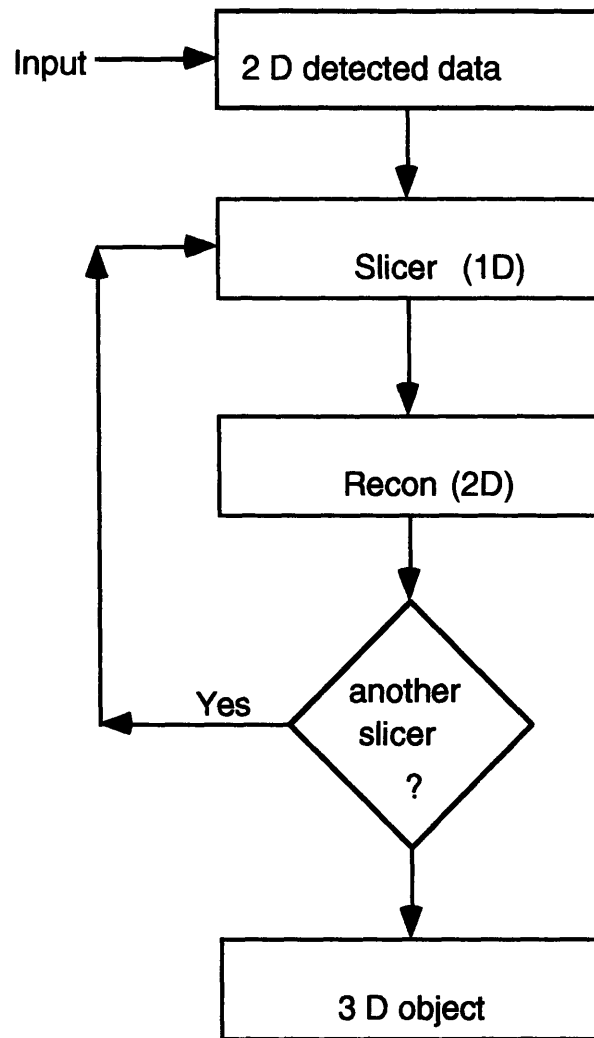


Figure 5.15: Flow chart for the three dimensional reconstruction procedures

a three dimensional reconstructed object function. Figure 5.15 shows the flow chart for the three dimensional reconstruction procedures.

After the reconstruction, we get a set of slice images. Pile them up and we will get a three dimensional object, which we can view at different angles. This is a unique advantage of tomographic image systems. Mathematically we get the image from the reconstruction method. After the reconstruction we have all of the three dimensional data, so we can display it in whatever way we want. This is especially good for nondestructive test and evaluation since from the three dimensional data we can quantitatively calculate chemical composition. For example, for the corrosion test what we are concerned with we want to detect the percentage of the hydrogen in the materials. Since we have the three dimensional data we can calculate it quite easily .

Now there are many software packages available to display the 3-D images. One of them is Section-View [48]. It displays the 3-D image very quickly. Also you can rotate the object. But it can not do any image processing. IDL (Interactive Data Language) is another software package. It has a lot of image processing features but it runs slowly.

# Chapter 6

## Detector performance and experimental results

In this chapter, the imaging quality for the whole system was tested with respect to dark noise, readout noise, gain of the CCD camera, dynamic range and the spatial resolution. The experimental results were presented too. First, the noise performance was measured. Second, dynamic range for the CCD camera was tested. Third, the resolution of the system was obtained. Then the neutron radiographic images for corrosion detection were presented.

### 6.1 Noise performance

The ultimate performance of an imaging system is limited by its noise. The noise in a CCD image system comes from a variety of sources. There is, for example, fixed pattern noise, which is a function of the manufacturing technology used to make the CCD or other components in the system; there is quantum statistical noise which depends on the number of electrons that are collected in each charge well; there is readout noise, which is also statistical, and depends on the design and bandwidth of the analog amplifier in the CCD and in the camera; and there is dark noise, which is a function of the operating

temperature of the system. So, we must 1) remove pattern noise, 2) determine dark current, 3) determine readout noise.

Figure 6.1 shows the variance as a function of the mean signal at -30°C. The slope of the regression of the variance is a technically interesting quantity. This slope is an estimate of the transfer gain of the CCD camera expressed in output-digital-number per quantum of signal. The principle of this technique is straightforward. Assuming an image is taken for a fixed time, then the signal in electrons for a given pixel is just given by:

$$N_{ij} = n_{ij} + n_{read} \quad (6.1)$$

$n_{ij}$  is true signal and  $n_{read}$  is a fixed signal due to offsets and readout. The associated variance is given by:

$$\sigma^2 = \sigma_{ij}^2 + \sigma_{read}^2 \quad (6.2)$$

and, since the statistical variance  $\sigma_{ij}^2$  is just  $n_{ij}$  we get:

$$\sigma^2 = n_{ij} + \sigma_{read}^2 \quad (6.3)$$

The CCD camera analog to digital converter (ADC) converts signals from electrons to ADC counts with a gain  $G$ , the dimension of the  $G$  is in counts per electron. The ADC reading is given by:

$$A = Gn \quad (6.4)$$

where A is the digital counts and n is the number of electrons and thus, in units of ADC counts:

$$\begin{aligned}
 \sigma_a^2 &= G^2 \sigma_{ij}^2 + G^2 \sigma_{read}^2 \\
 &= G^2 n_{ij} + G^2 \sigma_{read}^2 \\
 &= G A + G^2 \sigma_{read}^2
 \end{aligned} \tag{6.5}$$

If we then plot the variance of the difference of two images versus the average value of signal, the slope directly gives the gain of the system in electrons per ADC count and the intercept is the read noise. Figure 6.1 shows the noise performance of the camera when operated at -30°C and in high resolution mode. From this slope, we obtain a gain of 0.15 count/electron or approximately 7 electrons/count. The intercept yields a noise of approximately 12 electrons which is approximately equal to 1 detected neutron. As we mentioned in Chapter 3, the light output for one incident neutron is  $1.7 \times 10^5$  photons and corresponds roughly to 14 electrons.

The steps used to calculate the gain and readout noise are summarized as follows:

- 1). Plot mean of the ADC as a function of exposure time. Get the offset (i.e. the intercept).
- 2). Calculate the new mean.

$$\text{New Mean} = \text{Mean}/2 - \text{offset}/2$$

- 3). Calculate the variance.

$$\text{Variance} = \text{RMS}^2/2$$

- 4). Plot variance as a function of new mean. The slope is the gain. The intercept is equal to the square of the gain times readout noise.

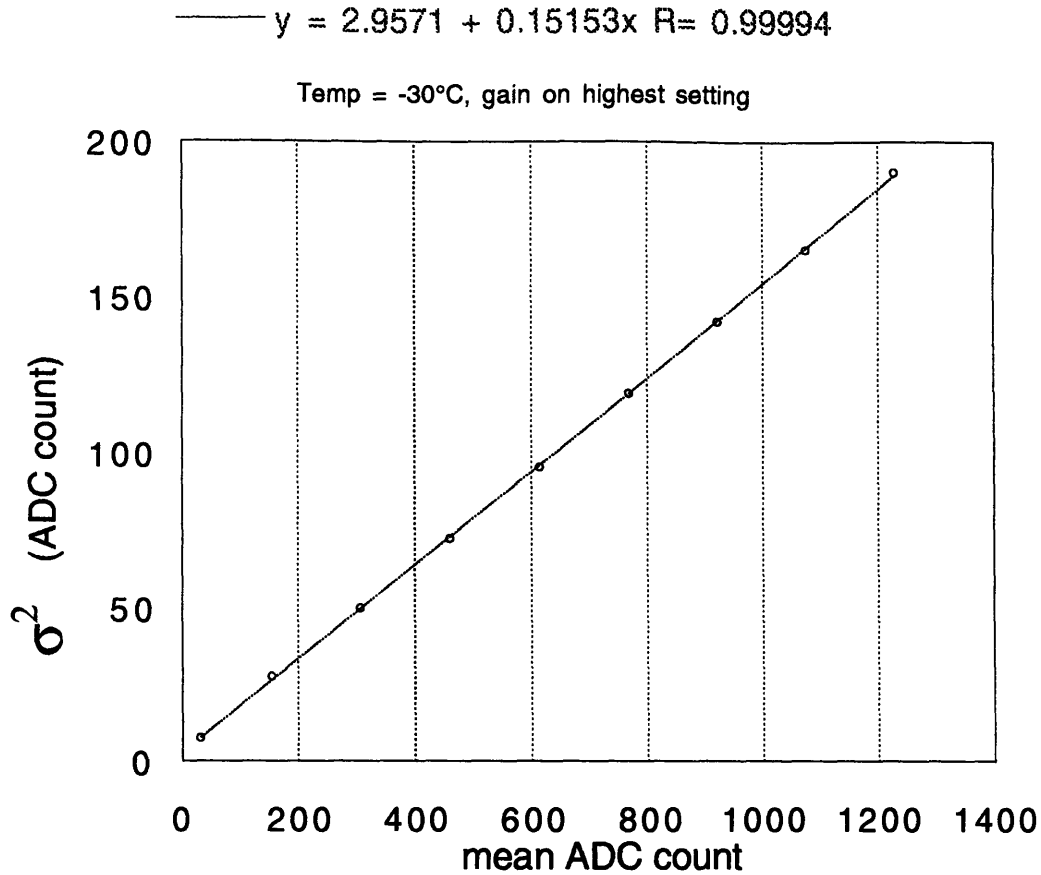


Figure 6.1: Determination of the readout noise and gain of the CCD camera system using measurement of the variance in the dark current.

In order to determine the signal to noise ratio (SNR) and the dynamic range, it is important to remove the effect of fixed pattern noise. This noise does reduce the usefulness of an image, but in a way that is not well characterized by a numerical parameter. Fixed pattern noise can be removed from the data by taking two images under the same exposure conditions and forming the numerical difference image. What remains in the difference image is the root mean square (rms) of the statistical noise from the two original images.

In our experiments, images were collected in pairs. The first pair was acquired with 1 minute exposure time and successive pairs with 2, 3, 4, and 5 minutes. After taking each image, the mean, rms and the standard deviation were measured for all the pixels in a single image. The formulas used to compute the density measurements are as follows. Let  $N$  = number of pixels in the region, and  $I_{xy}$  = pixel values within the region. Then

$$\text{Mean} = \sum I_{xy} / N \quad (6.6)$$

$$\text{RMS} = [\sum I_{xy}^2 / N]^{1/2} \quad (6.7)$$

$$\text{Standard Deviation} = [\sum I_{xy}^2 / N - \text{Mean}^2]^{1/2} \quad (6.8)$$

The pair images were subtracted so the fixed pattern noise was removed, then the rms deviations were found for the numerical difference images. These data were recorded by using a 15-bit ADC at 420 kHz readout speed. Table 6.1 gives the raw data of mean, rms and standard deviation for different exposure time at -34°C.

When we plot the mean as a function of the exposure time, we will get the offset for the system (i.e. the intercept), see Figure 6.2.

Since when the exposure time equals zero, the mean reading should be zero too, we can calculate the new mean in this way:

$$\text{New Mean} = \text{Old Mean}/2 - \text{offset}/2 \quad (6.9)$$

We can also calculate the variance; the variance is equal to the half of the rms square. Table 6.2 shows the raw data for new mean, RMS and the variance for different exposure time at -34°C.

Table 6.1: The raw data of mean, RMS and standard deviation  
for different exposure time at -34°C.

Exposure Time	Images	Mean ( ADC count)	RMS ( ADC count)	Stand. Dev. ( ADC count)
1 min	A	1256.66		
	B	1255.58		
	(A-B)		9.38	9.24
2 min	A	2361.83		
	B	2361.61		
	(A-B)		13.48	13.48
3 min	A	3466.80		
	B	3466.98		
	(A-B)		16.11	16.11
4 min	A	4571.76		
	B	4571.63		
	(A-B)		18.74	18.74
5 min	A	5676.80		
	B	5677.09		
	(A-B)		21.14	21.14

Table 6.2: The raw data for new mean, RMS and variance for  
different exposure time at -34°C.

Exposure Time	New Mean ( ADC count)	RMS ( ADC count)	Variance ( ADC count) <sup>2</sup>
1 min	552.51	9.3800	43.992
2 min	1105.0	13.480	90.855
3 min	1657.5	16.110	129.77
4 min	2210.0	18.740	175.59
5 min	2762.6	21.140	223.45

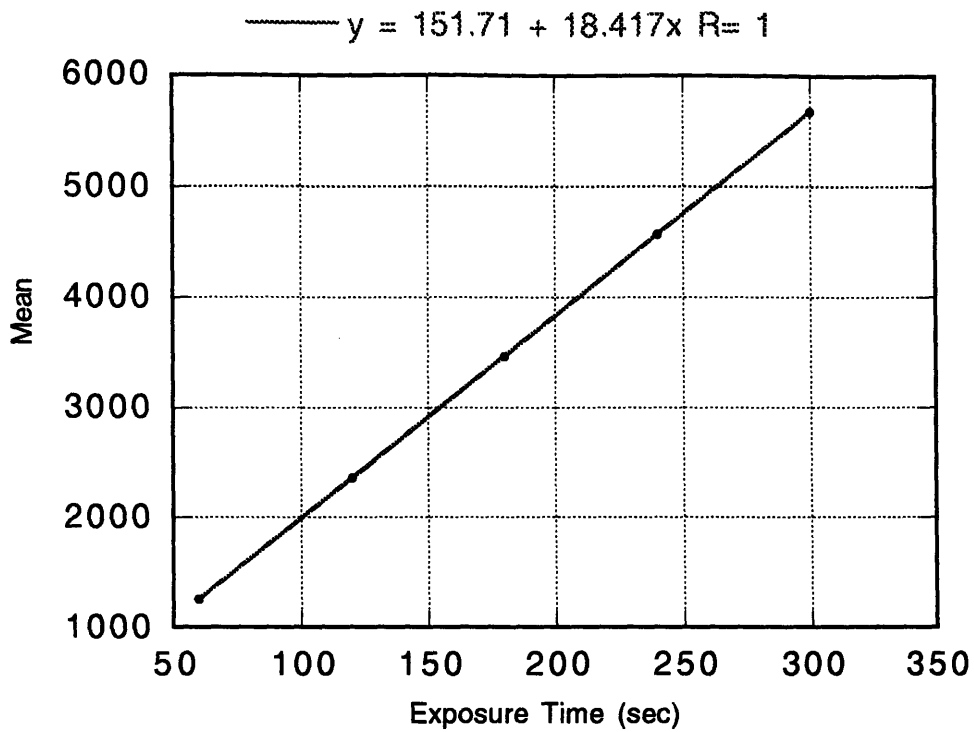


Figure 6.2: The mean as a function of exposure time at -34°C.

The CCD camera used in our experiment was cooled by chilled water. Figure 6.3 shows our measurement results of the variance varies with different exposure time; the temperature ranges from -34°C, -40°C, -44°C, -48°C to -50°C. It is clear that with the decrease of the temperature the noise level is reduced significantly. It also shows the excellent linearity of the variance noise as a function of exposure time (illumination).

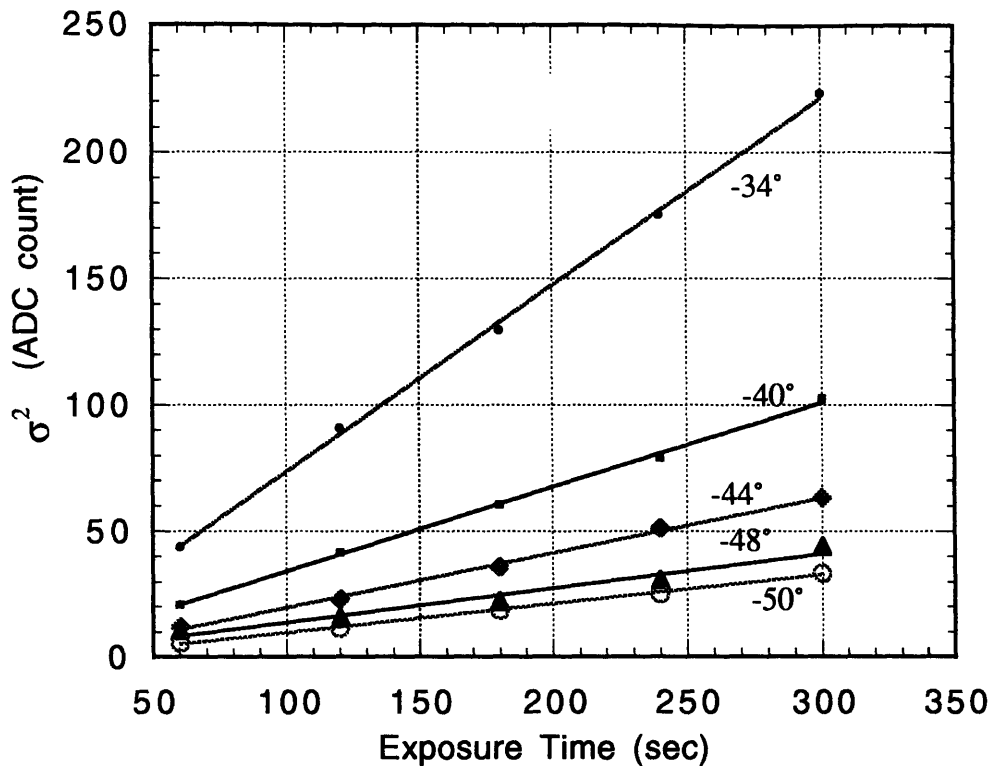


Figure 6.3: The variance in the image as a function of the exposure time. Results are shown for the temperatures of  $-34^{\circ}\text{C}$ ,  $-40^{\circ}\text{C}$ ,  $-44^{\circ}\text{C}$ ,  $-48^{\circ}\text{C}$ , to  $-50^{\circ}\text{C}$ .

Generally speaking, the signal to noise ratio (SNR) of the CCD system is a function of exposure time. At lower exposure time region, the readout noise dominates, while in long exposure time region, the statistical noise dominates. In the region dominated by readout noise, the SNR is linear with exposure time; while in the statistical noise dominated region, the SNR is proportional to the square root of the exposure time. We want to operate the CCD camera at a high SNR region, so some times we may take several short exposures then put them together or some times we just take a long single exposure. The strategies for image optimization are different in the two regions.

## 6.2 Dynamic range

Dynamic range,  $D$ , is defined as the ratio of the maximum usable signal level to the readout noise level. The readout noise level is the noise level in an image for which there is no exposure, i.e., a bias image. In general, the maximum usable signal is limited by the CCD charge well size or the amplifier saturation, whichever is smaller.

In our imaging system, the maximum usable signal is equal to:

$$U_{sat} = 2^{15} \times G \quad (6.10)$$

where  $G$  is the gain of the CCD camera, is equal to 7 electron/count. We already know that the readout noise level is 12 electrons so we have:

$$D = U_{sat}/\sigma_{read} = 2 \times 10^4 \quad (6.11)$$

## 6.3 Spatial Resolution

In order to represent an object by its image, an image system must be used. The image system is a bridge from the object to its image. Mathematically, we assume that such a system can be represented by an operator  $S\{\}$ , which acts on an input function (i.e.: object) to produce an output functions (i.e. image). If  $f(x, y)$  represents the input and  $g(x, y)$  represents the output, then we have:

$$g(x,y) = S\{f(x,y)\} \quad (6.12)$$

This relationship between input and output is shown schematically in Figure 6.4.

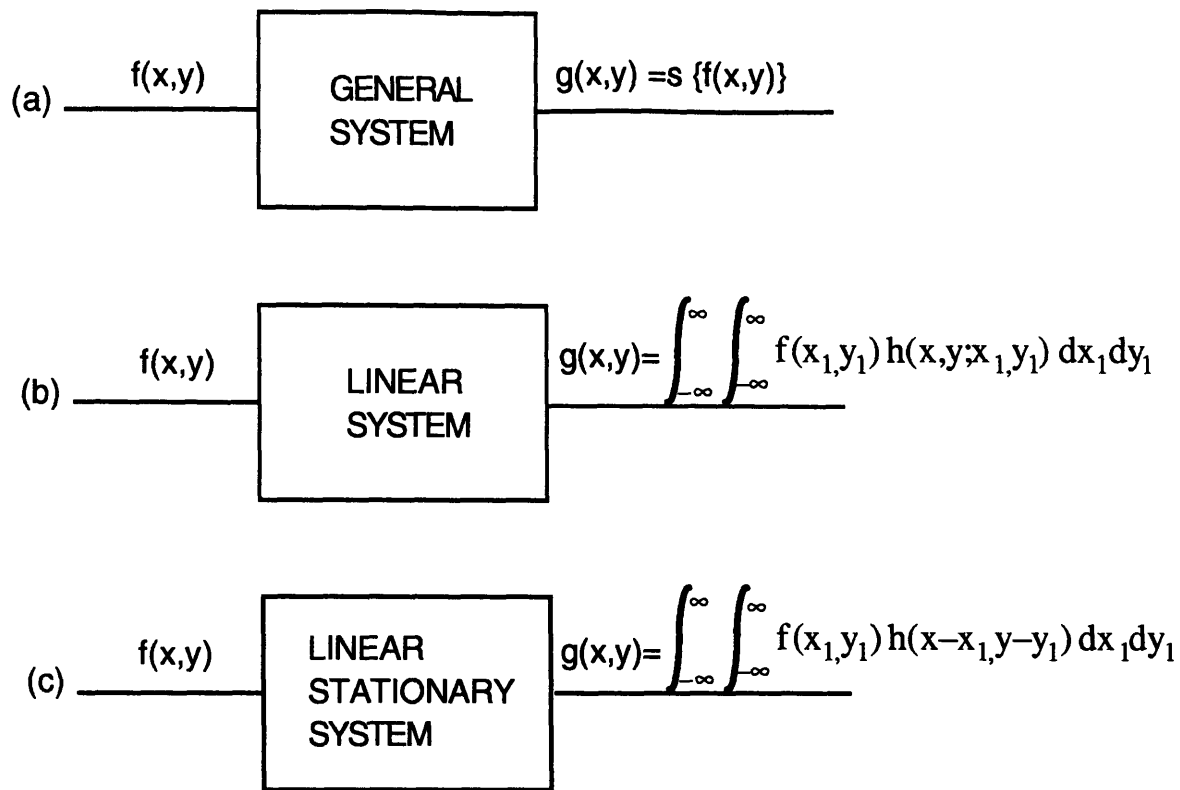


Figure 6.4: Schematic representation of (a) a general system; (b) a linear system; (c) a linear and stationary system.

If we restrict the nature of the system, we can develop the relationship further.

For a system that is both linear and stationary, the input-output relationship becomes:

$$g(x,y) = \int_{-\infty}^{\infty} \int_{-\infty}^{\infty} f(x_1, y_1) h(x-x_1, y-y_1) dx_1 dy_1 \quad (6.13)$$

$$g(x,y) = \int_{-\infty}^{\infty} \int_{-\infty}^{\infty} f(x-x_1, y-y_1) h(x_1, y_1) dx_1 dy_1 \quad (6.14)$$

where

$$h(x,y; x_1, y_1) = S\{\delta(x-x_1)\delta(y-y_1)\} \quad (6.15)$$

$h(x,y; x_1, y_1)$  is called the point spread function (PSF).

We can see that the output image is equal to the input convoluted with the point spread function, as represented in Figure 6.4.(c). Due to the physical meaning of convolution this is often referred to as a "smearing", or "blurring" of one function by another. So the spatial resolution of an image system is determined from the point spread function.

In the analysis of spatial image detail we shall see that Fourier Transform theory and spatial frequency analysis of images can be greatly beneficial. By doing a Fourier transform, we can get more detailed information about the image system.

Generally, if we have a function  $f(x, y)$ , it's Fourier transformation is defined as :

$$F(k_x, k_y) = \int_{-\infty}^{\infty} \int_{-\infty}^{\infty} f(x,y) e^{-i(k_x x + k_y y)} dx dy \quad (6.16)$$

Then in the spatial frequency space equation (6.14) can be written as:

$$G(k_x, k_y) = F(k_x, k_y) H(k_x, k_y) \quad (6.17)$$

The Fourier transform of the point spread function (PSF) corresponds to the optical transform function (OTF) and the modulus of the OTF is called modulation transfer function (MTF).

The main advantages of the spatial frequency  $(k_x, k_y)$  description over the distance  $(x, y)$  description is that the complicated process of convolution is replaced by a straightforward multiplication.

In practice, there is a more useful concept called the line spread function. Assuming we have a line input, the response of the system to a line input is defined as the line spread function of the imaging system.

Mathematically, the line spread function is obtained from the point spread function by integrating over one variable.

$$l(x) = \int_{-\infty}^{\infty} \int_{-\infty}^{\infty} \delta(x-x_1)h(x_1,y_1)dx_1dy_1 \quad (6.18)$$

where we use a single delta function  $\delta(x_1)$  to represent the line input.

$$l(x) = \int_{-\infty}^{\infty} h(x,y_1)dy_1 \quad (6.19)$$

For a linear photographic system the modulation transfer function is equal to the modulus of the Fourier transform of the line spread function.

As we mentioned earlier the spatial resolution of an imaging system is determined by the PSF. Therefore, it should also be determined by the LSF. Evidently the spatial resolution can also be determined from the modulation transfer function (MTF) of the imaging system. The MTF is the Fourier transform of the line spread function, normalized to unity in the low frequency limit. In our tests, both the MTF and the PSF were measured to represent the spatial resolution of our detector.

Mathematically, suppose the input is an opaque edge lying along the y-axis such that

$$f(x) = 0 \quad (x < 0); \quad f(x) = 1 \quad (x > 0)$$

Applying the convolution relationship, the edge spread function (i.e. the image of the edge)  $e(x)$ , is given by

$$e(x) = \int_{-\infty}^{\infty} \int_{-\infty}^{\infty} f(x-x_1)h(x_1,y_1)dx_1dy_1 \quad (6.20)$$

$$e(x) = \int_x^{\infty} l(x_1)dx_1 \quad (6.21)$$

The edge spread function is an integration of the line spread function. From equation (6.21) it follows that the line spread function is given by the differential of the edge spread function:

$$l(x) = \frac{d}{dx}(e(x)) \quad (6.22)$$

In our measurement, eight images were captured with the same settings for the field of view and exposure. These images are summed together to provide the raw data image for the MTF analysis. The region of the image across the edge used to generate the line spread function is much wider than the perceptible unsharpness in the image of the edge, also this region should not include any flawed regions on the CCD.

The camera is set up with the NE-426 neutron to light converter screen material  $^6\text{LiF-ZnS:Cu}$  filling the field of view, so the image is located in the center of the field of view. The orientations of the edges of the bar chart were aligned along a column of the CCD to within one pixel width.

The steps to get the MTF from the raw data image are given as following:

- 1). Compute the column averages of the pixel values.

- 2). Compute the first differences of the column average. (It has been shown to be possible to use a relatively simple sum-and difference calculation [49] to get the line spread function.)
- 3). Compute the one-dimensional Fourier transform of the first differences.
- 4). Scale the Fourier transform to have unity real part at zero frequency.
- 5). Combine the real and imaginary parts of the transform at each frequency to evaluate the magnitude of the transform.

Figure 6.5 shows the whole scheme of the derivation of the MTF from the edge response curve.

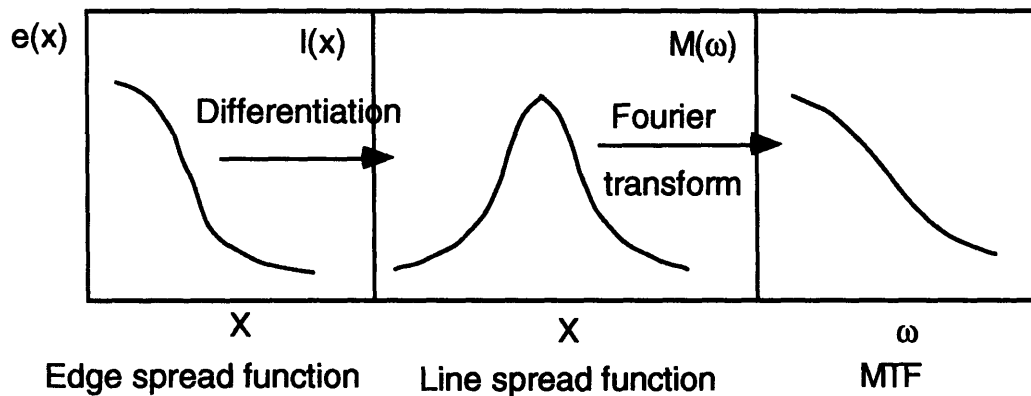


Figure 6.5: Derivation of the MTF from the edge response curve.

Generally speaking, in order to get a high quality images we need high thermal neutron flux with a uniform flux distribution over a large area, but the neutrons come from the accelerator is not in the thermal range. We have to design a moderator to let the neutrons be thermalized. High density polyethylene was used both as reflector and

moderator. The thermal neutrons produced by the moderator is not parallel, in order to get high quality pictures, collimator was designed to let the beam becomes more parallel.

A very simple kind of collimator is designed (see figure 6.6 (a)). It was mad of Cadmium cylinder with 8 inches diameter and 12 inches long. Another kind of collimator was designed and built too (see figure 6.6 (b)). It was made of  $B_4C$  painted aluminum.

The transmission behavior for the  $B_4C$  loaded paint was studied. The paint had a concentration of 6 g  $B_4C$  powder (1000 mesh) per 6 cubic center meter of paint-  $B_4C$  mixture. The attenuation of thermal flux was measured experimentally for the aluminum sheet with 0.9 mm  $B_4C$  paint; the thermal neutron flux loss is around 70%.

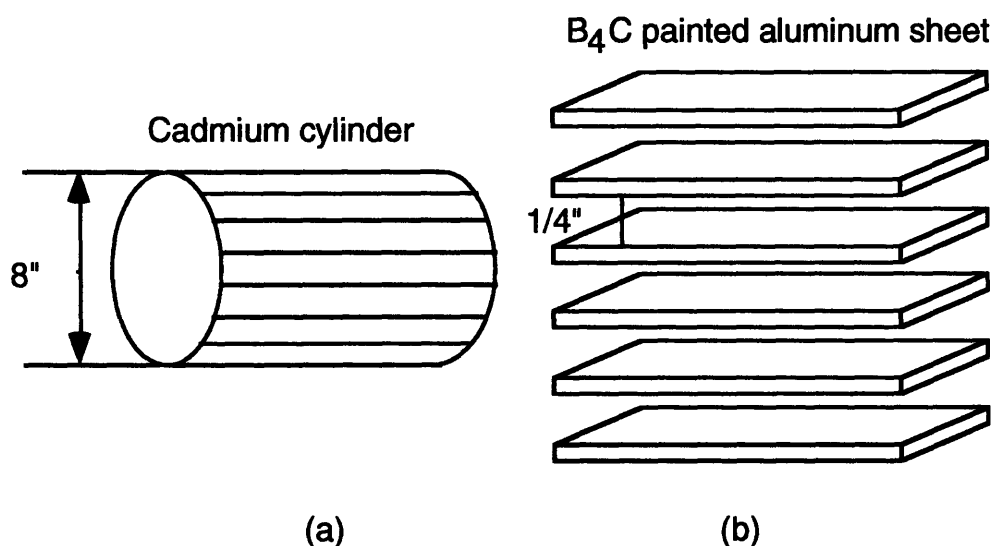


Figure 6.6: Two kinds of collimators. (a) Cadmium cylinder. (b) B<sub>4</sub>C painted aluminum.

Figure 6.7 shows the modulation transfer function of the detector as a function of spatial frequency [lp/mm]. Without collimator, the MTF at 2 lp/mm is 50%, with collimator, the MTF at 2.3 lp/mm is 50%. The collimator increases the whole system's resolution, but on the other hand it loses the beam flux too. Generally speaking, MTF

gives us more accurate information for images containing low spatial frequencies (e.g. small angle scattering in some cases).

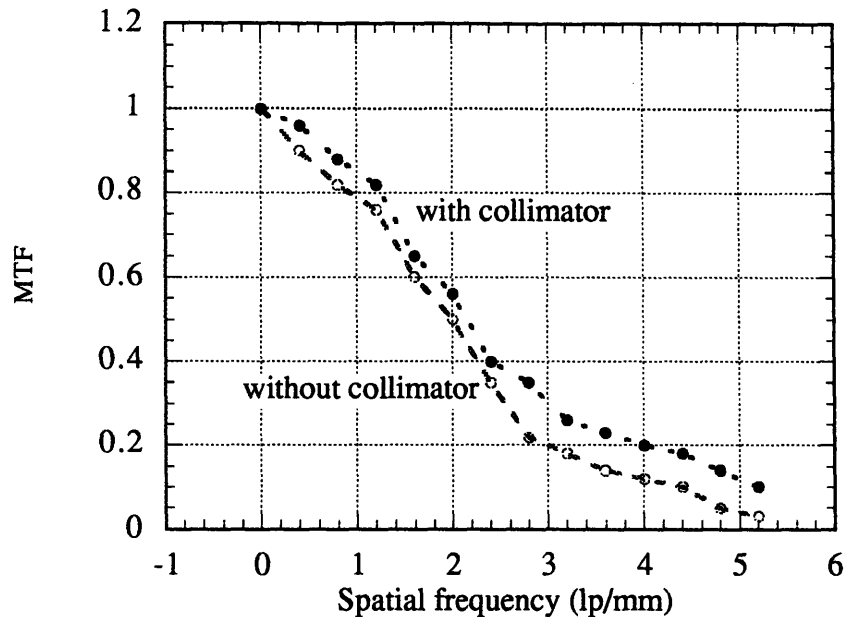


Figure 6.7: Modulation transfer function of the detector with  $B_4C$  painted aluminum collimator and without collimator.

## 6.4 Evaluation and demonstration of detection of corrosion

As an initial demonstration of the neutron radiographic image system, two small pieces of Cadmium were used as objects, Figure 6.8 shows the neutron radiographic image with 3 minute exposure time. The accelerator was operated at 4 mA ion beam current per pulse so the thermal neutron flux is in the order of  $10^5$  n/sec.

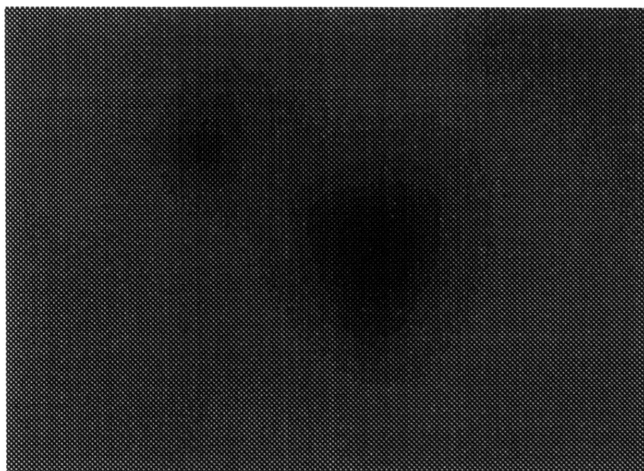


Figure 6.8: Neutron radiographic image for two pieces of Cadmium with 3 minute exposure time.

A group of polyethylene samples were prepared (see Figure 6.9) as benchmark for this neutron image system. Figure 6.10 shows the neutron radiographic images for the polyethylene with 3 minute exposure. The difference due to different thickness can be see clearly.

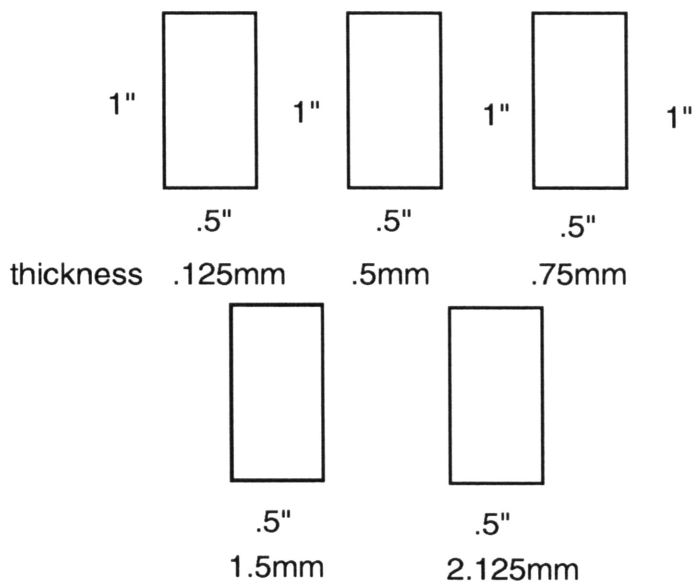


Figure 6.9: Polyethylene samples with the same size but different thickness.

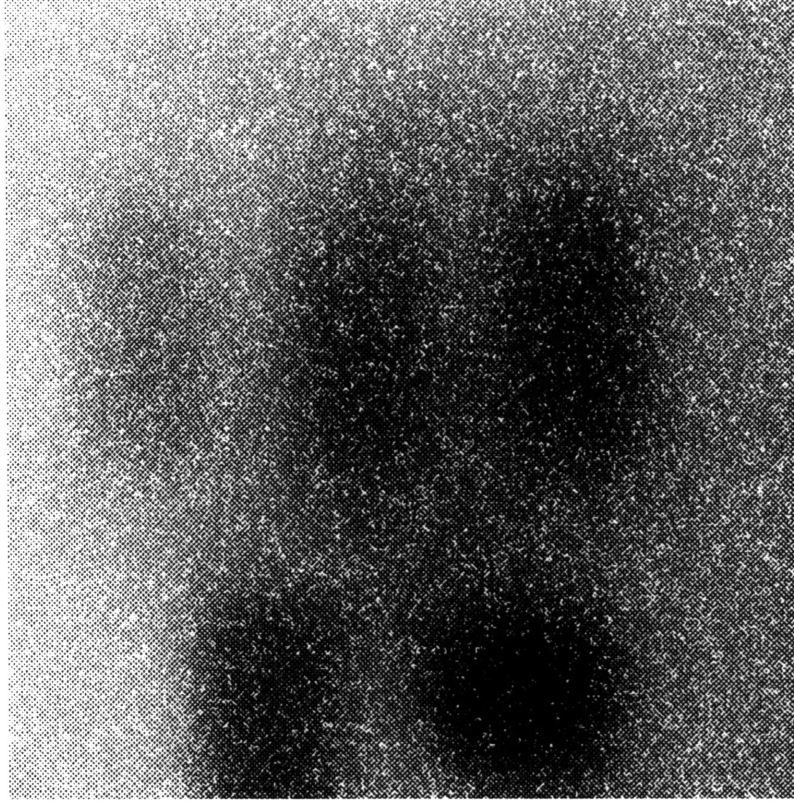


Figure 6.10: Neutron radiographic image for polyethylene with thickness of .125 mm, .5 mm, .75 mm, 1.5 mm and 2.125 mm.

The sensitivity of the system to corrosion detection can be estimated by assuming replacement of aluminum with an aluminum hydrate. For transmission image, the linear absorption coefficient for pure aluminum is  $0.0861 \text{ cm}^{-1}$  and  $2.4 \text{ cm}^{-1}$  for the hydrate. The signal expected, that is, the change in neutron counts, is given by:

$$\Delta N = N d\mu \Delta x \quad (6.23)$$

and the noise is the statistical variation in  $N$  (we already proved the other noise can be neglected) and is equal to  $N^{1/2}$ .

So, for a given signal to noise ratio (SNR) we have:

$$\text{SNR} = N d\mu \Delta x / N^{1/2} \quad (6.24)$$

which gives the required number of counts for a given SNR as:

$$N = (\text{SNR})^2 / (d\mu \Delta x)^2 \quad (6.25)$$

The exact SNR required to establish the presence of some feature depends on the observer and the feature being observed. For a skin thickness of 0.040" of aluminum, the minimum total number of detected neutrons to see a 0.001" corrosion layer is  $1.7 \times 10^4$  for an SNR of 1 or  $4.2 \times 10^5$  for an SNR of 5, assuming no error in flat field correction. With our current system, this would require 5 sec. and 125 sec. for a measurement.

A small section of aluminum lap joint from a salvaged KC-135 was imaged using the accelerator neutron source. A planar image of the joint was taken with a 120 second exposure and a similar image was obtained of the neutron beam without the lap joint. Finally, the ratio of the two images was computed and a new image made (see Figure 6.11 and Figure 6.12).

The image was taken with the CCD camera pixels grouped in a 4 x 4 array. Using the system minification of 7 and the size of the CCD pixels ( $22.5 \mu\text{m} \times 22.5 \mu\text{m}$ ) the effective size of each pixel in real space is  $0.63 \text{ mm} \times 0.63 \text{ mm}$  or 252 pixels/cm<sup>2</sup>. Clear regions of decreased signal are seen in the ratio picture. Small regions of interest were defined both within the decreased signal area and in the full signal area and the average pixel values were determined. The value in the full signal area was  $23000 \pm 450$  and  $22000 \pm 450$  in the decreased signal area. From this we obtain a value for  $\Delta N/N$  of  $(1000 \pm 630) / 23000 = 0.043 \pm 0.027$ . To reduce the error in this, we rotated the image and then averaged the columns of pixels. The rotated image is show in Figure 6.13. Based on

these we can compute the effective amount of absorber,  $\Delta\mu\Delta x=0.043$ . Assuming  $\text{Al(OH)}_3$  ( $\mu=2.4$ ) or  $\text{AlO(OH)}$  ( $\mu=1.5$ ) is present, with an averaging  $\mu=2.0$ , we get  $\Delta x = 0.02$  cm. The area of highest attenuation also had an additional layer of 0.1 cm aluminum which has an attenuation of  $\Delta\mu\Delta x = 0.1 \times 0.0861=0.00861$ , considerably less than the thin layer of corrosion. From this, it can be concluded that we are not observing additional thickness of aluminum. To correcting for this, we obtain a value of  $\Delta N/N = 0.023$  which gives a thickness of corrosion of 0.012 cm, assuming an average value for  $\mu$  of 2.0. Depending on the value of  $\mu$ , the value of  $\Delta x$  could range between 0.009 and 0.015 cm. After examining the disassembled section we observed corrosion in the area as well as a thin layer of sealant along the narrower region. Thus, we concluded that the system is capable of detection of thin layers of corrosion even with a lower than expected neutron flux.

To estimate the detected neutron flux, we used the calibration of the CCD. The ADC gain was 7 electrons/count. Thus, 23000 counts represents  $1.61 \times 10^5$  electrons. Based on an estimate of 100 electron per neutron, this signal represents  $1.61 \times 10^3$  n/pixel (actually 4 x 4 group). Using these values, we estimated the flux as  $1.61 \times 10^3$  n/pixel x  $250 \text{ pixel/cm}^2/120\text{sec}= 3.4 \times 10^3$  n/sec/cm<sup>2</sup> detected neutrons or  $2.3 \times 10^4$  n/sec/cm<sup>2</sup> incident on the screen, a number consistent with our earlier estimates.

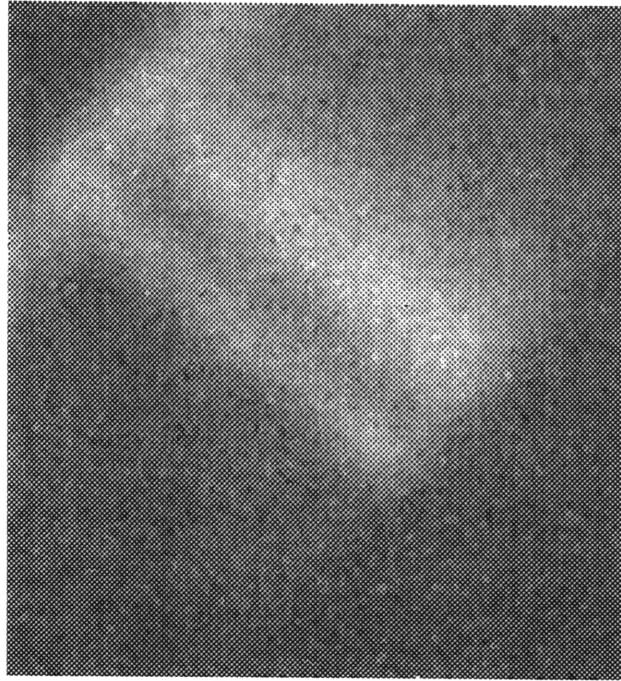


Figure 6.11: Neutron radiographic image of a piece of aluminum lap joint from a KC-135.

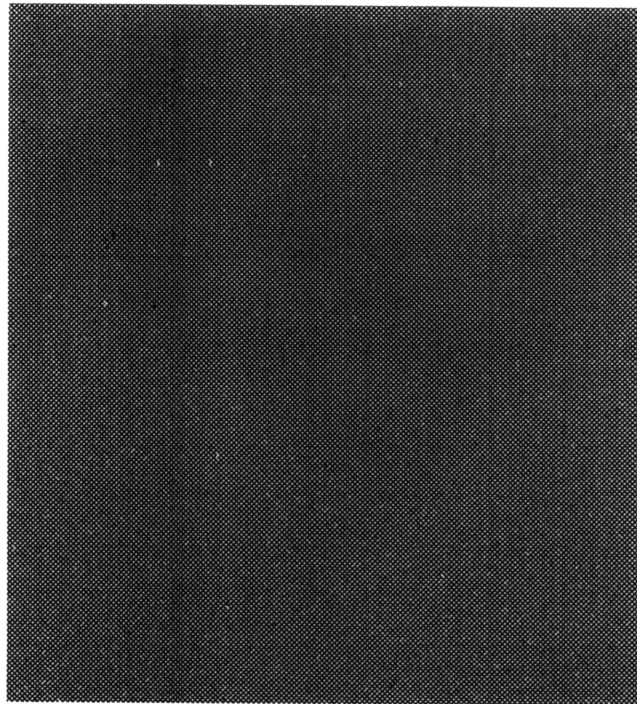


Figure 6.12: Same as Figure 6.11, except with photo negative, the bright area in Figure 6.11 becomes the dark region in this picture.

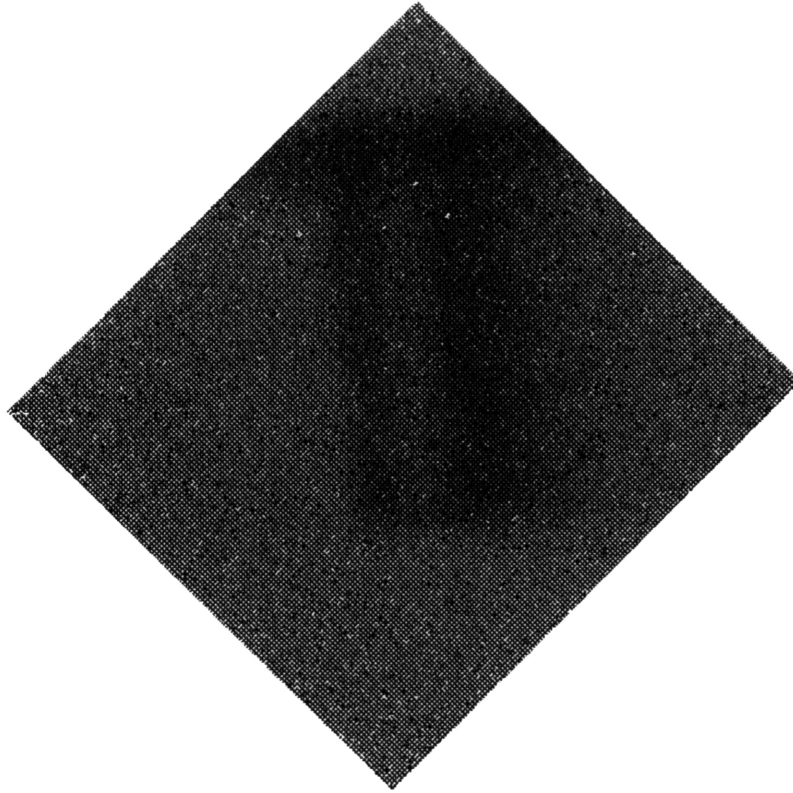


Figure 6.13: This is the picture of the same lap joint without filtering or equalization, but with rotation of 45 degree. A region of interest was chosen to cover the two dark strips and the average pixel value for each column of the rectangle was calculated.

## **6.5 Verification of tomographic hardware and reconstruction software performance**

In order to show the performance of the entire tomographic imaging system, a few tomographic images were made by using a 40 kV x-ray tube. All of the components of the imaging system were the same as those for the neutron tomographic imaging, except that one used X-ray, the other used neutron beam. Thus, this experiment measured all parts of the system and confirmed the correct operation procedures which we have developed during building the system. A test sample was constructed using a metal part

(wrench socket) and a small chicken bone mounted off center on a rubber mud. 18 views were taken every 10° and dimension for each radiographic image is 310 x 228 pixels.

Figure 6.14 shows the reconstructed tomographic result, which is equivalent to the 140th cross sections by pixel counts. The hollow part for the wrench socket can be seen clearly.

Figures 6.15 and 6.16 are projection views taken at 0° and 160° angles respectively. This test shows the whole digital tomographic imaging system is working well.

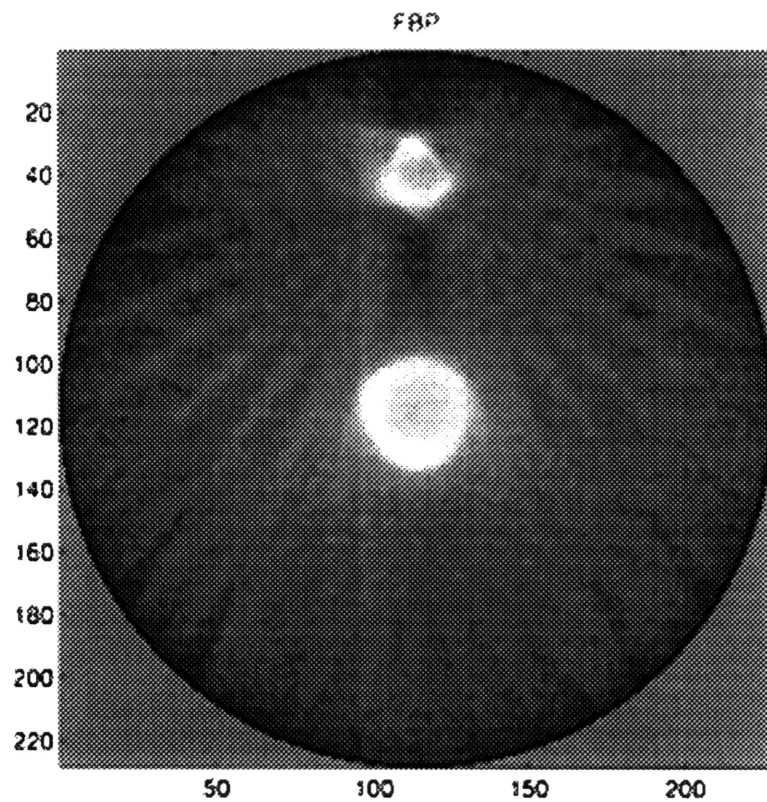


Figure 6.14: Tomographic reconstruction results for the metalwrench socket and the chicken bone. The hight is equivalent to the 140th cross sections by pixel counts.

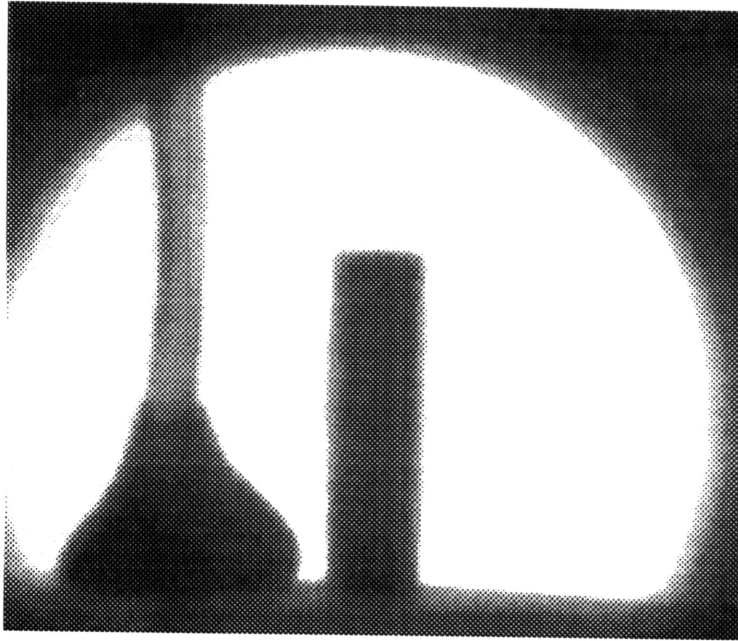


Figure 6.15: The radiographic image for the metal wrench socket and the chicken bone at 0°

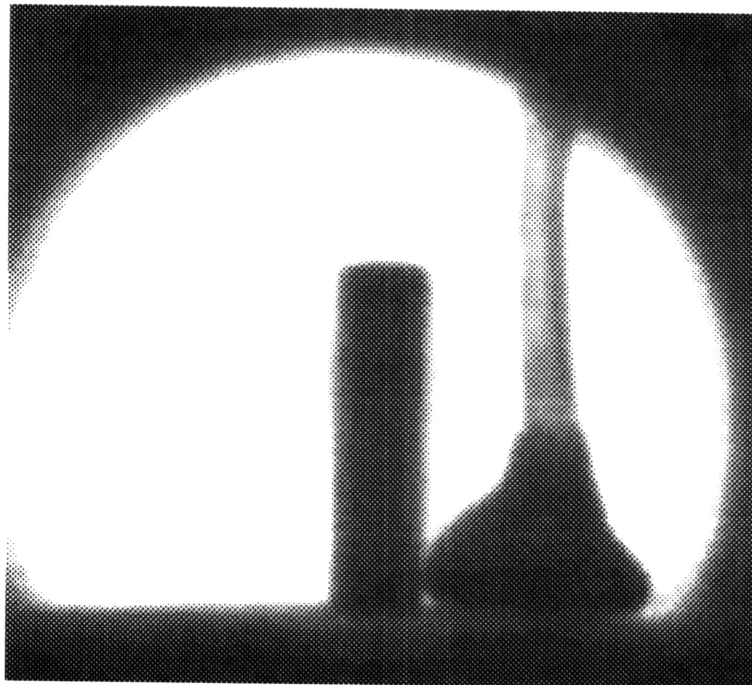


Figure 6.16: The radiographic image for the metal wrench socket and the chicken bone at 160°

# Chapter 7

## Discussion and conclusions

### 7.1 Discussion

#### 7.1.1 Neutron sources

The major components for the neutron radiography and tomography imaging system are the neutron source, detectors, and image data processing. Among them, the neutron source is an important component. The resolution of the imaging system is a function of the beam quality (i.e. the beam collimation and thermal neutron flux). The exposure time was solely determined by the intensity of the thermal neutron flux. The neutron sources as being available can be classified in three general types: (a) nuclear reactor, (b) radioactive, and (c) accelerator. The possible use of these neutron sources for radiography and tomography must be considered from several points of view. Included among the items one must consider are neutron energy and intensity, gamma energy and intensity, portability, cost, size, shielding problems, collimation and general utility. Table 8.1 gives the comparison of the best performance of three type neutron sources with our AccSys Technology model DL-1 RFQ.

Compared to accelerator based and radioisotope sources, nuclear reactor neutron sources have one big advantage: a relatively large neutron flux, typically well collimated

Table 7.1: Comparison of the best performance of three type neutron sources with our AccSys Technology model DL-1 RFQ.

Source type	Power (MW)	Thermal neutron flux (n/cm <sup>2</sup> -sec)	(L/D)	Cost	Portability
Reactor	50 -200	10 <sup>12</sup>	100-150	very expensive	no
Accelerator	100	10 <sup>10</sup>	10-20	expensive	yes
Radioisotope	no	10 <sup>4</sup> -10 <sup>5</sup>	10-20	expensive	yes
AccSys	0.4	10 <sup>7</sup>	10-20	median	yes

by long beam ports extending from the moderator material near the reactor core to the laboratory. However, with the development of the new charge particle acceleration techniques, accelerators are beginning to rival reactors in both total and thermal neutron flux.

A significant limitation for using reactor source is that we can not built a portable imaging system with it. With applications for neutron radiography and tomography expanding, it is necessary to design and built a small, portable, and easy to operate neutron imaging system

One alternative is radioisotope source. These sources are portable and can be incorporated into moveable structure that can be maneuvered about the object of interest; and for this type of sources require little technical skill to operate. However, as illustrated in Table 7.1 , the neutron yield achievable from these sources is exceedingly low compared to reactor and accelerator sources, resulting in radiographs of much poor quality and resolution for a given exposure time. Additionally, since the flux is a function of half-life, the more intense sources often have short half-life. Californium-252 is by far

the radioisotope of choice due to its small size, low  $\gamma$ -output, low average neutron energy, relatively long half-life, and yield per unit cost.

The third option, optimal compromise and promise choice in the future, is a particle-accelerator based neutron source. Although these source cannot presently equal the thermal neutron flux of reactors for highly collimated beam, their thermal flux is much higher than radioisotope sources; they have the advantage of producing a neutron beam only when needed; also there is no waste disposal problem involved in this kind of neutron sources. Accelerators are becoming small and compact enough to be incorporated in maneuverable imaging systems; and as the size and cost of accelerators decrease, the prospect for industry, universities, and military bases having on-site neutron sources becomes more realistic.

### **7.1.2 A comparison of NTI with other corrosion detection methods**

There are some other nondestructive corrosion testing image techniques are available now, among them Eddy current and thermal wave image techniques are more popular. A general introduction of those two methods are given here and the comparison of those technique with our neutron nondestructive testing method are also described.

#### **Eddy current method**

The eddy current method of nondestructive testing, as currently practiced, was pioneered by Friedrich Forster in the 1940's [50], and there has since been rapid progress in its development. Eddy current method tests can be used on all materials which are electrically conducting. They include the sizing of surface and sub-surface cracks, measurements of the thicknesses of metallic plates and non-metallic coatings on metal substrates, assessment of corrosion and measurements of electrical conductivities and magnetic permeabilities. These latter properties may be related to structural features such

as hardness, chemical composition, grain size and the stretch of this materials. An important advantage of eddy current testing over some other methods, such as ultrasonic and potential drop techniques, is that there is no need for physical contact with the surface of the object being tested. Thus careful surface preparation is unnecessary.

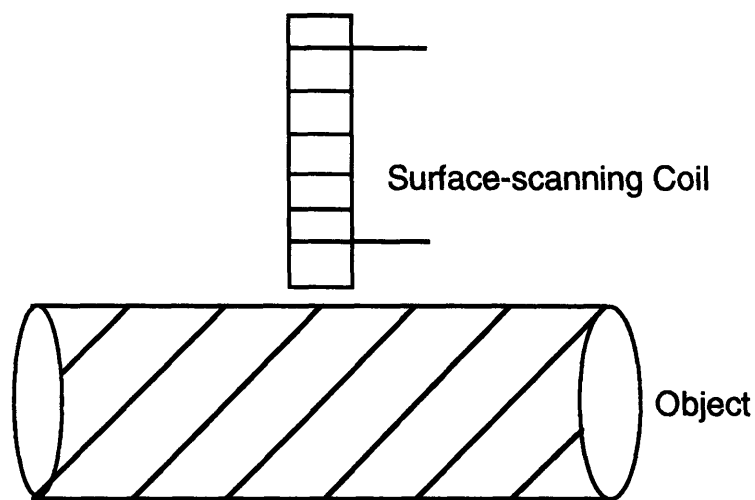


Figure 7.1: Basic coil component for surface scanning eddy current testing.

Eddy current testing system consists of exciting an alternating current at a given frequency through a coil, we call it a probe-coil , located as near as possible to the electrically conducting object being tested, and thus to induce eddy currents in the latter.

With the eddy current method, the current passing through the coil generates electromagnetic waves through an electrical conductor in its vicinity. The associated magnetic field induces the flow of electric currents, i.e. eddy current.

As a result, changes take place in the components of the impedance of the coil which can be related to the design of the coil, the size, shape and position of the test object and the values of its magnetic permeability  $\mu$  and electrical conductivity  $\sigma$ . The

impedance of the coil is also affected by localized variations in  $\mu$ ,  $q$  and the geometry of the object under test as a result of the presence of a defect.

If we compare Eddy current method with neutron tomographic image, we will find:

I). Resolution 3000  $\mu\text{m}$ (ECM) 200-500  $\mu\text{m}$ (NTI).

II). The depth of the detection 4-8 mm(ECM), 20 cm(NTI) or more for airplane wing.

III). The detection time for 400  $\text{cm}^2$ , using Eddy current method it will take half hour, while for NTI it only take less then 3 minutes. So NTI is more efficient than ECM.

It is clear that neutron tomographic image has more advantages than eddy current method.

### **Thermal Wave Image**

Thermal wave image is another method used for nondestructive test [51]. In this method, a flash lamps pulse was used to heat the object surface uniformly. After the pulse, a thermal diffusion wave was formed, the wave velocity depends on the property of the object. If the object is perfect without any defect or corrosion, the thermal wave will propagate uniformly, but if there is flaw or corrosion or defect, the behavior of the thermal wave will change. A infrared camera was used to monitor the object surface temperature following the heat pulse. Computer and fast image processor extracts the thermal wave echo image. From the images which we get at different time we can know the size and the depth of the defects or corrosion.

If we compare Thermal wave image with neutron tomographic image, we will find:

I). Resolution 5000  $\mu\text{m}$ (TWI) 200-500  $\mu\text{m}$ (NTI).

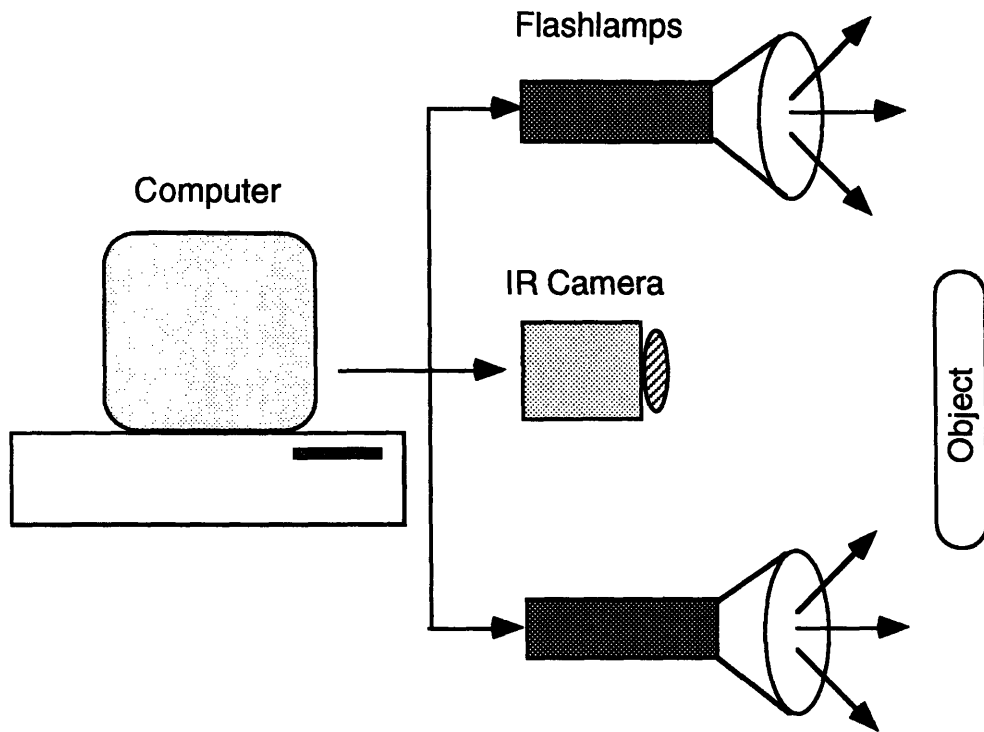


Figure 7.2: Thermal wave image system.

II). The depth of the detection 1 mm(TWI), 20 cm(NTI) for airplane wing.

III). TWI requires flat surfaces. In practical, most of the parts of an airplane are not flat.

For small and thin objects, thermal wave imagine has some advantage, but for aircraft corrosion detection, due to the surface of the aircraft is not a flat, this method loses his power too.

The low resolution for eddy current method and the flat surface requirement for thermal wave imaging limits their usefulness for corrosion detection for aircraft. The neutron radiographic tomographic nondestructive testing method so far seems is the most powerful way for corrosion detection in aircraft industry.

## 7.2 Conclusions

In this thesis work, a compact portable neutron radiographic and tomographic image system has been designed, built and installed. An AccSys Technology model DL-1 radiofrequency quadrupole (RFQ) accelerator neutron source (producing neutrons by the reaction  ${}^9\text{Be}(d,n){}^{10}\text{B}$ ) was used in this imaging system. The accelerator weights 400 lbs with 1.22 meters long, 1.84 meter high and 0.88 meter wide. The thermal neutron flux produced by this accelerator is  $10^4$  n/cm<sup>2</sup>.sec. It is this portable neutron source that makes our imaging system portable.

Neutrons have proved to be a powerful tool for nondestructive testing and evaluation both for science and engineering. In order to obtain high quality images, reactor neutron sources have been used in the past. Radiographic and tomographic imaging systems using reactor neutron sources have already made great contributions to scientific research work in this field. In reality, we need a nondestructive test system that is moveable, instead of one that remains in the laboratory. It is clear that if we want to detect the presence of corrosion on any part of an aircraft, the testing equipment must be portable. A portable neutron imaging system lets a nondestructive test step out from the laboratory and move into the real world, thus it has significant meaning to science and engineering. The benefits apply to the aircraft industry, and also to human beings as a whole since aircraft safety is an important issue to everyone.

In this thesis work, an electronic digital imaging system for corrosion detection was developed. Traditionally, people store their images on films, which are very expensive and difficult to do any imaging processing. Our digital imaging system has great advantages over the traditional film image system. In our system, a computer controls the camera and saves the images digitally. In this way, not only is film eliminated, but also imaging processing on the stored digital images becomes reality.

In this thesis work, the benchmarks to quantify the image quality for this digital image system were measured. In order to determine the resolution of the imaging system the modulation transfer function (MTF) was measured. The dark noise for the CCD camera was measured and the read out noise for the charged couple device (CCD) camera was also calculated from experimental data. The gain and dynamic range of the CCD system were measured.

Two sets of three dimensional reconstruction software for our neutron imaging system were developed and tested. A new reconstruction technique, multiscale simulation reconstruction, was also put into our reconstruction software; therefore, we can get multiple scales simultaneously. The advantage of this technique lies in the ability to trade off reconstruction time and resolution during initial fast scanning to discover possible problems in the object under investigation by a fine scale reconstruction which could be used to extract edges and features. In conventional tomography, a complete high resolution reconstruction is made, followed by post processing of the image to extract features. With multiscale reconstruction, an initial quick reconstruction could be made to determine areas of corrosion, followed by a subsequent interactive zooming in the region of interest at high resolution if corrosion is detected.

In this thesis work, moderators and collimators were designed and installed. Collimation is an important procedure for an imaging system which uses accelerator neutron sources, since the neutrons which come out from the accelerator are not parallel; thus in order to obtain reasonable resolution for the image we have to use collimator. The collimator can eliminate the scattered neutron components from the digital image.

A preliminary effort was made to apply this imaging system to non-destructive tests for corrosion detection of aircraft aluminum lap joint parts from an aging KC-135 aircraft. The testing result shows that even the system with a lower than expected neutron flux, we still could detect a thin layer of corrosion. The sensitivity of this digital imaging

system was estimated theoretically and tested experimentally. The tomographic reconstruction software for this digital imaging system was verified by using x-ray.

### **7.3 Suggestion for future work**

A high quality thermal neutron source is a key step for visualizing the corrosion parts in the aircraft fuselage and wing. More work needs to be done on the accelerator based neutron source in order to obtain both high flux and good collimation.

The combination of the moderator and collimator is an important part for accelerator based neutron imaging system. Since the neutrons from the accelerator are not in the thermal energy range, the moderator must match the neutron energy spectrum for use in imaging. The moderated neutron beam is not parallel, so a collimator must be used, otherwise the scattered neutrons will reduce the contrast resolution for the imaging system. More work should be done on optimizing those two parts.

# **Appendix A**

## **Basic CCD theory**

The CCD chip handles electrical charges in a way closely analogous to a hydraulic system. The charge packets can be regarded as quantities of fluid stored and shifted in a series of buckets.

### **A.1 A CCD image sensor operates in four successive steps**

#### **During the exposure period:**

1). It converts the incident illumination into a proportional quantity of electrical charges (photocharges). This is achieved by an array of photoelements disposed either along a line (linear array) or in a two dimensional matrix (area array). The input of a CCD image sensor consists of an array of photosensitive elements, or pixels, which carry out the light-to-charge conversion. These can be photodiode or photoMOS elements (see Figure A.1) disposed either along a single line or in a two-dimensional matrix.

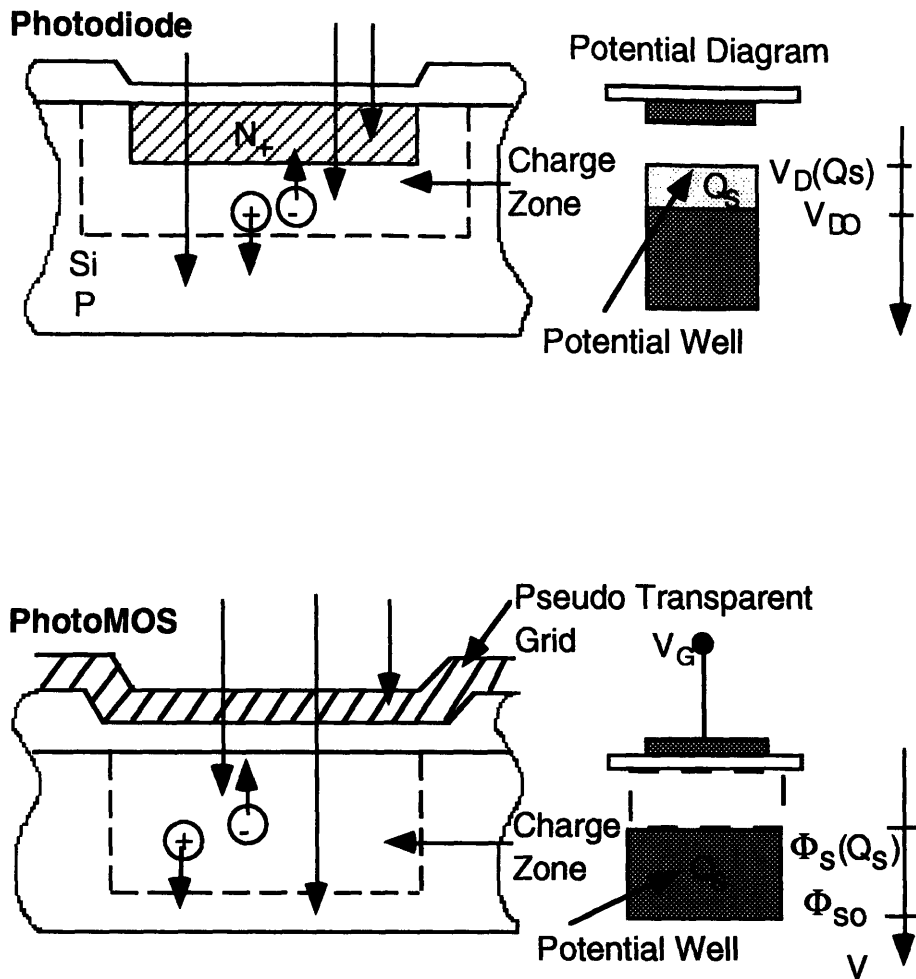


Figure A.1: Photodetection using silicon.

When a photon enters in the silicon, an electron-hole pair is generated. The electron is collected in a depleted zone created by means of a diode or MOS structure, while the hole is re-combined in the silicon substrate. People generally use quantum efficiency,  $\epsilon$ , which characterizes the sensitivity for each photosensitive element to convert light into charge. It is defined as the ratio of a number of collected photocharges to the number of incident photons on a pixel area.

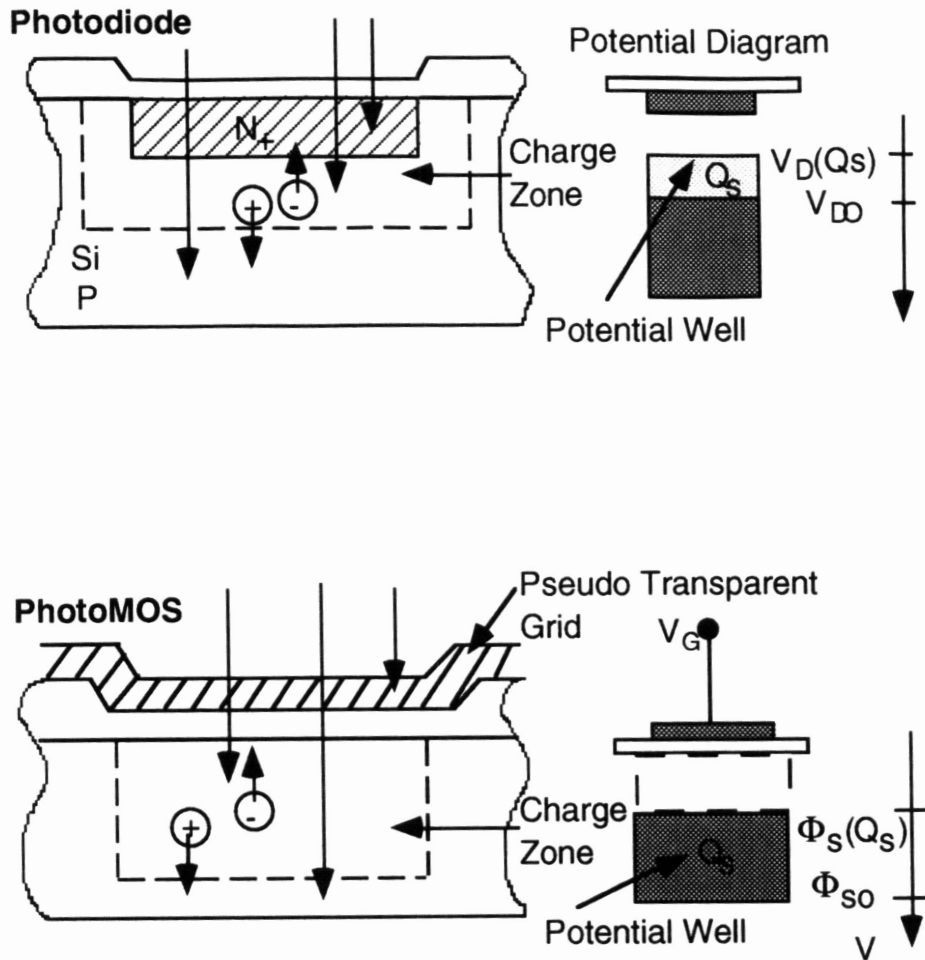


Figure A.1: Photodetection using silicon.

When a photon enters in the silicon, an electron-hole pair is generated. The electron is collected in a depleted zone created by means of a diode or MOS structure, while the hole is re-combined in the silicon substrate. People generally use quantum efficiency,  $\epsilon$ , which characterizes the sensitivity for each photosensitive element to convert light into charge. It is defined as the ratio of a number of collected photocharges to the number of incident photons on a pixel area.

This cycle is then iterated, starting at line A, with the charges shifted along one half stage at each new change in the  $\Phi_1$   $\Phi_2$  clock configuration.

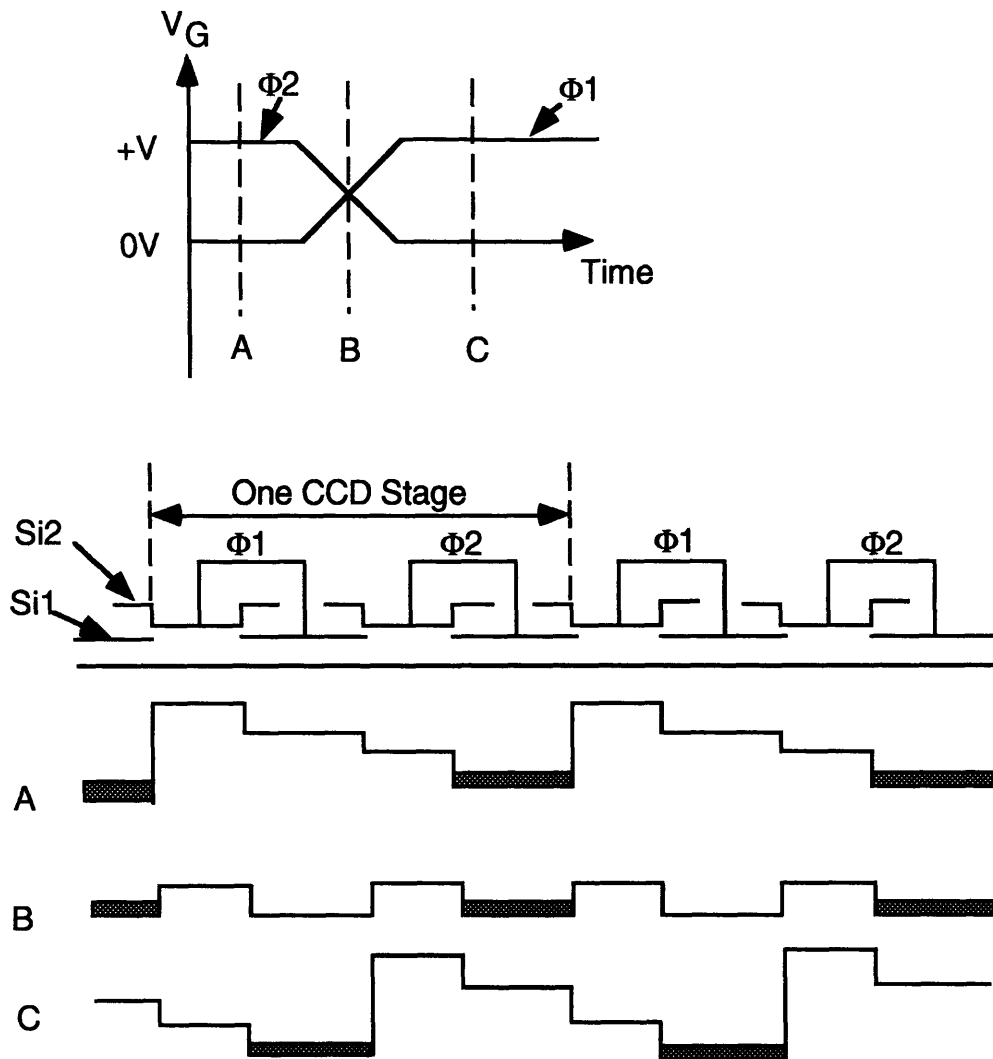


Figure A.2: Two phase transfer operation.

4). At the readout stage, each arriving photocharge packet is converted into a proportional voltage signal. Additional sampling and amplification give the low impedance output video signal. Finally let us consider the readout stage. As the charges arrive at the

readout stage, they are converted to a proportional voltage level. This conversion is carried out by a readout diode, adjacent to an output gate,  $V_{gs}$  (DC biased). After readout, charges are drained away in a reset diode via an MOS transistor.

A CCD image sensor can thus be considered as a "black box" which transforms an optical image, i.e. a spatial distribution of radiation, into a time-distributed voltage signal.

Figure A.3 shows the four steps for CCD image sensor operation procedures.

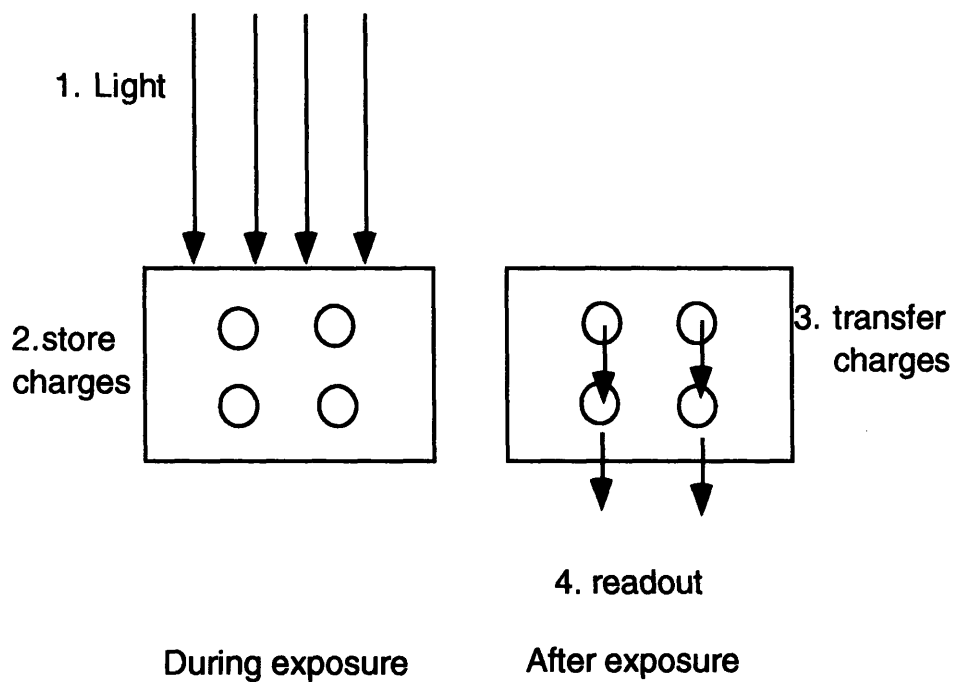


Figure A.3: The four steps for CCD image sensor operation.

## A.2 Electrooptical performance

The main parameters that characterize CCD image are given in the following.

## A.2.1 Spectral response

The spectral response of a CCD is the relation between responsivity and the wavelength of the illuminating wavelength. Responsivity is the ratio of useful signal voltage ( $V_{os}$ ) to exposure. Figure 3.11 shows the spectral response for two CCD's and uses a human eye as a reference. Figure 3.11 illustrates the dependence of the spectral response on the type of photoelectric element. We also can see that both structures have a good response in the near-infrared spectrum of up to 1100 nm. This is why in our experiment, the ZnS scintillator has been modified to our specifications of using a Cu activator rather than the standard Ag activator. This is because it shifts the spectrum of the emitted light further toward the red region where the quantum efficiency of the CCD is higher.

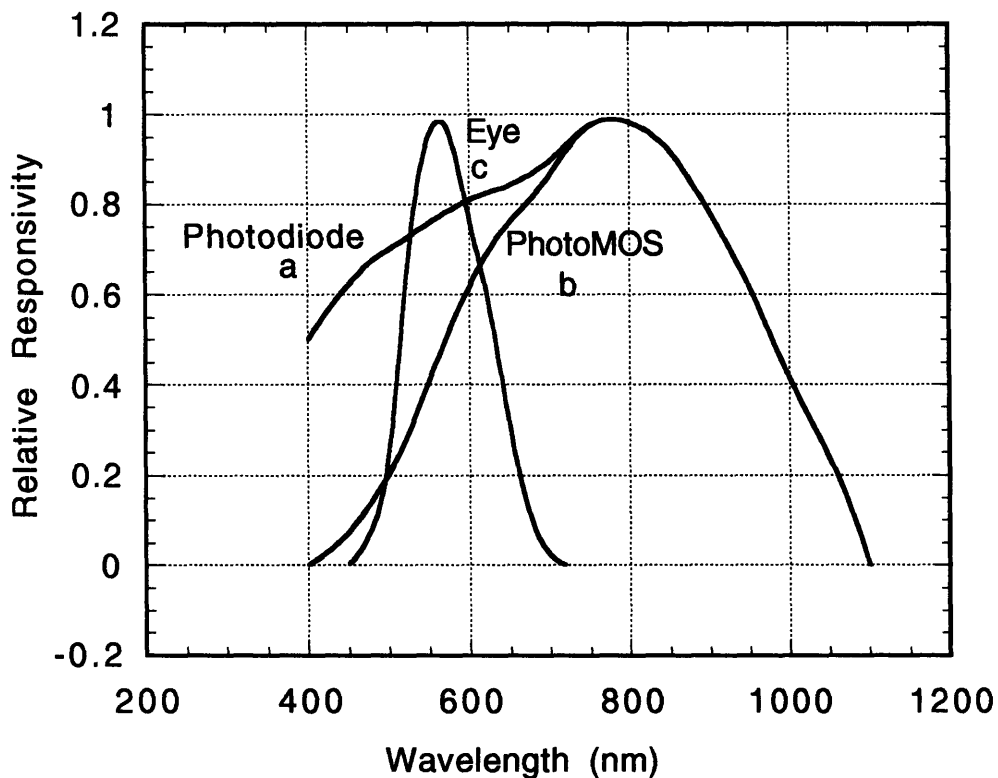


Figure A.4: Typical spectral responses for a) a photodiode, b) a photoMOS, c) the human eye for reference.

## A.2.2 Noise

There are two significant sources of noise, one is dark noise and another is readout noise. The dark noise mainly depends on the temperature of the operating system. Readout noise mainly depends on the readout system, such as the dynamic range for reading and the pixel numbers which are used to grab the image.

### Dark Noise

Dark current voltage,  $V_{DS}$ , is generated in the silicon element by the thermal motion of the electrons. If the thermal energy is sufficient, electrons can move into the conduction band where they are trapped and contribute to the detected charge, even though without signal we can still detect this dark current. Thermal dark charge is a function of temperature and time. The dark current depends on the property of the materials with which the semiconductors were made. The number of intrinsic charge carriers in the semiconductor,  $N$ , is given as following:

$$N = C \int_{t_1}^{t_2} \exp\left[-\frac{E_g}{2kT}\right] dt \quad (\text{A.1})$$

Where the integrated over the time of exposure and readout,  $E_g$  is the semiconductor gap energy needed for electrons to enter the conduction band,  $T$  is the temperature in Kelvin,  $k$  is Boltzmann's constant, and  $c$  is constant over small temperature ranges.

The dark current drops by a factor of two for each decrease in temperature of approximately 6 °C.

Thus, it is beneficial to minimize the readout time, and essential to operate the CCD at the lowest possible temperature. In our experiment , we use a chilled water cooling system. The lowest temperature we can achieve is -52°C.

## **Readout Noise**

Readout noise, or temporal noise is defined as the fluctuation in time of a given pixel; it is generally referred to by the root mean square value of the detector array when no light is incident on the detector.

Readout noise is influenced by several factors, such as charge transfer efficiency, reset noise, (which is introduced when recharging the diode to its reference potential), amplifier bandwidth and dark current.



```

!source shiinitial.csh

%$$$ Get the options for reconstruction.
[optionr, optionn] = getoption_k_v2;
if (optionr == 3),
    disp(' ');
    disp('>>>> FILTER OPTIONS');
    disp('+++++');
    disp('Filter types:');
    disp(' 1. RAMP 2. HAN 3. HAM 4. PARZN 5. BUTER');
    fi = input('The filter type           : ');
    cu = input('The cut off frequency       : ');
    rd = input('The order of the filter      : ');
end

%$$$ Calculate the scaling factor for display.
sf = 128/ndimu;

%$$$ Input the phantom.
%counts = pinputg_k('group_2', ndimu);

%$$$ Start collecting the projection data.
%eval(['!source run_proj.csh ', num2str(ndimu), ', ', num2str(kdimu), ', ...',
%     num2str(nang), ', ', num2str(sf)]);

%$$$ Load the phantom image file, and convert it to a 2-D array.
%load phant.mlb;
%pimage = d12d2(phant, ndimu);

%$$$ Load projection data and make it noisy.
load proj.dat;
if (optionn == -100),
    nproj = proj;
else
    signal_power = (proj'*proj)/(nang*kdimu);
    SNR = optionn;
end

```





```

%$$$ Load the wavelet transform matrix.
eval(['load dWf3',num2str(kdimu),'];');

%$$$ Form dWT = dW*T to save some multiplications later on.
dWT = dW*T;

%$$$ Transform the projections.
for angi = 1:nang,
    Tproj( kdimu*(angi-1)+1 : kdimu*(angi-1)+kdimu,1 ) = dWT*...
        nproj( kdimu*(angi-1)+1 : kdimu*(angi-1)+kdimu,1 );
end

%$$$ Prepare the transformed projections for back-projection.
Tproj_bp = zeros(size(Tproj));
for angi = 1:nang,
    Tproj_bp( kdimu*(angi-1)+1 : kdimu*(angi-1)+kdimu,1 ) = ...
        dW'*...
        Tproj( kdimu*(angi-1)+1 : kdimu*(angi-1)+kdimu,1 );
end

%$$$ Get the begin and end of each scale.
[begi, endi, nsca] = getbes(kdimu);

%$$$ Do reconstruction at different scales.
if (optionr ~= 7),
    xvar = -140;
    if (ndimu == 128 | ndimu == 256 )
        yvar = 408;
    else
        yvar = 268;
    end
    Tprojsc = zeros(size(Tproj));
    for angi = 1:nang,
        Tprojsc( kdimu*(angi-1)+kdimu : ...
            kdimu*(angi-1)+kdimu, 1 )=...
            Tproj( kdimu*(angi-1)+kdimu : ...

```

```

        kdimu*(angi-1)+kdimu, 1);
end
for scale = nsca:-1:1,
    xvar = xvar + 140;
    if ( (scale ~= nsca) & ( rem((nsca-scale),3) == 0 ) ),
        xvar = 0;
        yvar = yvar - 140;
    end
    if (optionr == 9),
        Tprojsc = zeros(size(Tproj));
    end
    for angi = 1:nang,
        Tprojsc( kdimu*(angi-1)+begi(scale) :...
                kdimu*(angi-1)+endi(scale), 1 )=...
                Tproj( kdimu*(angi-1)+begi(scale) :...
                       kdimu*(angi-1)+endi(scale), 1);
    end
    Tprojsc_bp = zeros(size(Tproj));
    for angi = 1:nang,
        Tprojsc_bp( kdimu*(angi-1)+1 :...
                   kdimu*(angi-1)+kdimu,1 ) = dW'*...
        Tprojsc( kdimu*(angi-1)+1 : kdimu*(angi-1)+kdimu,1 );
    end
    save msrec.prj Tprojsc_bp /ascii;
    eval(['!source run_back.csh ', num2str(ndimu),' ',...
          num2str(kdimu),' ',num2str(nang),' ',num2str(sf)]);
    eval(['!mv msrec.mlb msrec',num2str(scale),' .mlb']);
end
end

%$$$ Do final reconstruction.
save msrec.prj Tproj_bp /ascii;
eval(['!source run_back.csh ', num2str(ndimu),' ',...
      num2str(kdimu),' ',num2str(nang),' ',num2str(sf)]);

load msrec.mlb;

```













# References

- [1] Bauccio M.L., "Case Studies of Material Deterioration and Failure", *Materials Selection for Military Equipment* (A Handbook of Critical Properties and Applications), National Association of Corrosion Engineers (1987) 1.
- [2] Latanision R.M., Gastine O.H, Compeau C.R., "Stress Corrosion Cracking and Hydrogen Embrittlement: Differences and Similarities", *Proceedings of the Symposium on Environment Sensitive Fracture of Engineering Materials*, Fall AIME Meeting, 24-26 October 1977.
- [3] Parkins R.N., "Current Understanding of Stress-Corrosion Cracking", *Journal of Metals*, Vol. 44, No. 12, (1992) 12
- [4] *Aircraft Accident Report--Aloha Airlines, Flight 243, Boeing 737-200, N73711, Near Maui, Hawaii, April 28, 1988*; NTSB/AAR-89/03, National Transportation Safety Board, Washington, D.C., 20594 (1989).
- [5] Barton J.P., Bader J.W., Stokes J.A., "Experience with Aircraft Inspection in the MNRS Using Film and Electronic Imaging, Neutron Radiography", *Proceedings of the Fourth World Conference*, Gordon and Breach Publishing Company (1992) 133.
- [6] Froom D.A., Barton J.P., and Bader J.W., "Neutron Radiography at Sacramento ALC, Neutron Radiography", *Proceedings of the Fourth World Conference*, Gordon and Breach Publishing Company (1992) 153.
- [7] Baconn G.E., *Neutron Physics*, Wykeham Publications, London (1969).
- [8] Henry A.F., *Nuclear-Reactor Analysis*, MIT Press, Cambridge, Mass [1975].
- [9] Berger H., *Neutron Radiography*, Elsevier Press, Amsterdam (1965).
- [10] Koeppe R., Brugger G., Schdapper G., Larsen G. and Jost R., "A Demonstration of Filtered Neutron Beam Computed Tomography", *J. of Comp. Assist. Tomography*, Vol. 5 (1981) 79.

- [11] Von der Hardt P., and Rottger H., *Neutron Radiography Handbook*, D. Reidell Publishing Company (1981).
- [12] Scharf W., *Particle Accelerators And Their Uses: Part 2, Application of Accelerators*, Harwood Academic Publishers (1986).
- [13] Thewlis J., *Brit. J. Appl. Phys.*, **Vol. 7** (1956) 345.
- [14] Thewlis J., *Progress in Nondestructive Testing, Vol. 1*, edited by E. G. Stanford and J. H. Fearon, Heywood, London (1958) 111.
- [15] Leeftang H. P., Markgraf J.F.W., "Detection of Corrosion on Aircraft Components by Neutron Radiography, Neutron Radiography", *Proceedings of the Fourth World Conference*, Gordon and Breach Publishing Company (1992) 161.
- [16] Fischer C.O., "The History of the First Neutron Radiographs in Berlin 1935-1944", *Proceedings of the Fourth World Conference*, Gordon and Breach Publishing Company (1992) 3.
- [17] Peter O., *Z. Naturforschung*, **Vol. 1** (1946) 557.
- [18] Chadwick J., *Nature*, **Vol. 129** (1932) 312.
- [19] Fermi E. and Szilard I., *U. S. Patent 2,708,656*
- [20] Brugger R.M., *Phys. Today*, **Vol. 21** (1968) 23.
- [21] Hennelly E.J., *Nucleonics*, **Vol. 19** (1961) 124.
- [22] Warman E.A., Presented at the 22nd National Convention of the Society for Nondestructive Testing, New York, 1962.
- [23] Anon., *Nucleonics*, **Vol. 14** (1956) 105.
- [24] Webb S., *The Physics of Medical Imaging*, Instituted of Physics Publishing, Bristol and Philadelphia (1988).
- [25] Matsomoto G., and Krata S., "The Neutron Tomography", *Neutron Radiography*, edited by Barton J.P. and Von der Hardt P., Proceedings of the Second World Conference, D.Reidell Publishing Company (1986).
- [26] Matsumoto G., Sendo T., Honda S. Ohkubo K. and Ikeda Y., "Improvement of Reconstructed Image Quality In Neutron CT", *Neutron Radiography*, edited by Barton J.P. and Von der Hardt P., Proceedings of the Second World Conference, D.Reidell Publishing Company (1986).

- [27] Kusminarto and Nicholas M. S., "Imaging With Neutrons in Transmission Tomography", *Neutron Radiography*, edited by Barton J.P. and Von der Hardt P., Proceedings of the Second World Conference, D.Reidell Publishing Company (1986).
- [28] McClellan G.C. and Tow D.M., "Damaged Reactor Fuel Assemblies", *Neutron Radiography*, edited by Barton J.P. and Von der Hardt P., Proceedings of the Second World Conference, D.Reidell Publishing Company (1986).
- [29] Lanza R. C., McFarland E.W., and Poulos G.W., "Computerized Neutron Tomography for Core Analysis, Soc. of Core Analysts", Conference paper 9128 (1991) 12.
- [30] McFarland E.W., Leigh J., Dai H., Lanza R.C., "Heterogeneous Distribution of Hydrogen in Titanium Compressor Blades: Detection and Characterization by Neutron Computed Tomography", SPIE Proceeding Vol 2092, SPIE Optical Engineering Press, Bellingham (in press).
- [31] Spowart A.R., "Optimising Neutron Scintillators for Neutron Radiography", *Brit. J. N. D. T.*, Vol. 11 (1969) 1.
- [32] Berger H, Brenizer J. and Rogerson J., "Comparisons of Thermal Neutron Imagers", to be published.
- [33] Kobayashi H., "Recent Development of CCD Camera for NR Imaging-Tomography", *Neutron Radiography*, Proceedings of the Fourth World Conference, Gordon and Breach Publishing Company (1992) 553.
- [34] Na H., Mcfarland E., Lanza R. C., "A Segmented Array Approach to Large Scale Neutron Radiography and Tomography Using Cold Charge Coupled Devices", *Neutron Radiography*, Proceedings of the Fourth World Conference, Gordon and Breach Publishing Company (1992) 591.
- [35] Casali F., et al., "A System for Neutron Radiography With a Cooled CCD Camera", *Neutron Radiography*, Proceedings of the Fourth World Conference, Gordon and Breach Publishing Company (1992) 481.
- [36] Scharf W, *Particle Accelerators and Their Uses: Part 1, Accelerator Design*, Harwood Academic Publishers (1986).

- [37] Wiedemann H., *Particle Accelerator Physics: Basic Principles and Linear Beam Dynamics*, Springer-Verlag, Berlin Heidelberg (1993).
- [38] Scharf W., *Particle Accelerators and Their Uses: Part 2, Applications of Accelerators*, Harwood Academic Publishers (1986).
- [39] Month M. and Dienes M., *Physics of Particle Accelerators*, AIP Conf. Proc. #184, Am. Inst. Phys., New York (1989)1829.
- [40] Kapchiniskii IM, Teplyakov VA, *Linear Ion Accelerator With Spatially Homogeneous Strong Focusing*, Prib. Tekh. Eksp., **Vol. 19** (1970) 2
- [41] W. Paul et al, *Z. Physik.*, **Vol.140** (1959).
- [42] Radon J., Uber die Bestimmung von Funktionen durch ihre Integralwerte langs gewisser Mannigfaltigkeiten, Berichte Sachsische Akademie der Wissenschaften, Leipzig, Math.-Phys. K1, **Vol 69** (1917) 262.
- [43] Hounsfield G. N., "A method and apparatus for examination of a body by radiation such a x-ray or gamma radiation", Patent Specification 1283915, The Patent Office (1972).
- [44] Deans S., *The Radon Transform and Some of Its Applications*, Wiley, New York, (1983).
- [45] Gordon R., "Image Processing for 2-D and 3-D Reconstruction from projection: Theory and Practice in Medicine and Physical Sciences", Conf. Proc. of Optical Society of America, Washington, DC (1975).
- [46] Macovski A., *Medical Imaging Systems*, Prentice-Hall, Englewood Cliffs, N.J. (1983).
- [47] Bhatia M., *Wavelet Transform-Based Multi-Resolution Techniques For Tomographic Reconstruction And Detection*, MIT Ph.D. Thesis. 1994.
- [48] Samosky J. T., "Section View: a System For Interactively Specifying and Visualizing Section Through Three-Dimensional Medical Image Data", MIT M. S. Thesis (1993).
- [49] Scott, F., Scott, R. M. and Shack, R. V., "The use of Edge Gradients in Determining Modulation-Transfer Function", *Photogr. Sci. Eng.*, **Vol 7** (1963). 345.

- [50] J. Blitz., *Electrical and Magnetic Methods of Nondestructive Testing*, A. Hilger Bristol, Philadelphia (1991).
- [51] R. L. Thomas, "Thermal Wave Imaging", Second Air Force Aging Aircraft Conference, Rose State College, May 17-19, 1994.